2011

# Development, validation and verification of the Momentum Source Model for discrete rotor blades

Kanchan Guntupalli
*Iowa State University*

## Recommended Citation

Guntupalli, Kanchan, "Development, validation and verification of the Momentum Source Model for discrete rotor blades" (2011). *Graduate Theses and Dissertations*. 10446.
https://lib.dr.iastate.edu/etd/10446

# Development, validation and verification of the Momentum Source Model for discrete rotor blades

by

Kanchan Guntupalli

A thesis submitted to the graduate faculty
in partial fulfillment of the requirements for the degree of
MASTER OF SCIENCE

Major: Aerospace Engineering

Program of Study Committee:
R. Ganesh Rajagopalan, Major Professor
Zhi J. Wang
Thomas J. Rudolphi

Iowa State University
Ames, Iowa
2011

## TABLE OF CONTENTS

# LIST OF TABLES

# LIST OF FIGURES

# NOMENCLATURE

| | |
|---|---|
| $N_b$ | number of rotor blades |
| $C_d$ | drag coefficient |
| $C_l$ | lift coefficient |
| $c$ | airfoil chord |
| $d^u, d^v, d^w$ | volume coefficients for u, v and w momentum equations |
| $f_i, g_i, h_i$ | functions representing contribution from grid point $i$ to the face flux |
| $\vec{F}$ | rotor force vector |
| $g$ | acceleration due to gravity |
| $\vec{J}$ | total momentum flux of the general variable $\Phi$ |
| $\dot{m}$ | mass flux leaving the domain around a boundary point |
| $M$ | local Mach number |
| $p$ | pressure |
| $p'$ | pressure correction |
| $Pe_\Delta$ | element Peclet number |
| $r, s, t$ | points on the face of a control volume |
| $R$ | rotor radius |
| $Re$ | Reynolds number |
| $\vec{S}$ | rotor momentum source term |
| $u, v, w$ | velocity components in the global coordinate system |
| $u', v', w'$ | velocity corrections |
| $\hat{u}, \hat{v}, \hat{w}$ | pseudo velocity components |
| $\tilde{u}, \tilde{v}, \tilde{w}$ | artificial velocity components |
| $U, V, W$ | velocity components in the local coordinate system |
| $U_{avg}$ | average velocity for a tetrahedron |

| | |
|---|---|
| $V_\infty$ | freestream velocity |
| $\vec{V}$ | velocity vector |
| $\vec{V}_\beta$ | rotor flapping velocity |
| $x, y, z$ | coordinates in the global coordinate system |
| $X, Y, Z$ | coordinates in the local coordinate system |
| $X_{min}, X_{max}$ | minimum and maximum $X$ component for a tetrahedron in local coordinates |

Greek Symbols

| | |
|---|---|
| $\alpha$ | angle of attack |
| $\beta$ | rotor flapping angle |
| $\delta$ | rotor blade deflection |
| $\mu$ | fluid viscosity |
| $\vec{\Omega}$ | rotor angular velocity vector |
| $\Phi$ | general, scalar transport variable |
| $\rho$ | fluid density |
| $\psi$ | rotor azimuth angle |
| $\theta_c$ | rotor blade collective pitch angle |
| $\theta_{tw}$ | sectional twist angle |
| $\xi, \eta, \zeta$ | rotor based Cartesian coordinate system |

# ACKNOWLEDGMENTS

I would like to express my deepest gratitude to my major professor, Dr. R. Ganesh Rajagopalan, for his guidance and support throughout this research and the writing of this thesis. I would also like to thank my committee members: Dr. Z. J. Wang and Dr. T. J. Rudolphi. I appreciate the financial support provided by the VLRCOE program for this research. Many thanks are also due to the Department of Aerospace Engineering at Iowa State University and its staff for computing resources and administrative help.

I take this opportunity to thank my colleagues and friends, Sayan Ghosh, Mark Lohry and Angela Lestari for their valuable suggestions and countless brainstorming sessions. I would also like to thank my fiancé, Sameer Garg, and my friends, Raman Sharma and Rucha Agnihotri, for standing by me throughout the course of my graduate studies. I would like to express my deepest appreciation for the love and confidence provided to me by my family. Last but not the least, I would like to dedicate this thesis to my mother.

# CHAPTER 1. INTRODUCTION

Over the past couple of decades, Computational Fluid Dynamics (CFD) has become a very popular tool for solving complex engineering problems. Unlike experiments, which are often expensive and time consuming, computational tools yield quicker and robust engineering solutions. The quest for solving more complex problems without considerable increase in computational effort has led to the need for developing faster and more accurate numerical methods. Most engineering problems are time dependent and deal with complex three-dimensional physical geometries. It is, therefore, evident that CFD techniques that can handle complicated geometries and furnish time accurate solutions are required for such problems.

A very crucial component for an accurate CFD analysis is the grid used for solving the problem. While grids can be classified in many different ways, one of the most basic distinctions is on the basis of grid connectivity. Grids with regular connectivity implicitly defined in the form of 2-D or 3-D arrays are called structured grids. On the other hand, unstructured grids are characterized by irregular grid connectivity, permitting various types of irregularly shaped grid elements. While structured orthogonal grids offer best accuracy, especially for viscous flow problems, they can be very difficult and time consuming to generate for complex geometries. In recent times, the need for meshing complex and multiply connected physical domains has popularized the use of unstructured grids. Unstructured grids are easier to generate, especially for complex geometries. Another advantage of unstructured grids is the ability to locally refine the grid without affecting the whole domain. This is especially important in resolving regions with high gradients. The run time and memory requirements for a structured grid based solver are undoubtedly less compared to an unstructured grid with the same number of grid points. But the ability to control grid refinement, better grid adaptation for irregular domains resulting in higher spatial accuracy with lesser number of grid points and overall reduction in grid generation time for unstructured grids, outweigh their disadvantages and make unstructured grid based solvers an alternative and viable option for solving complex engineering problems.

The Navier-Stokes equations are the most complete set of equations that correctly represent the physics of three-dimensional fluid motion. They are sometimes simplified by making certain assumptions like considering the fluid to be Newtonian. Numerical techniques used for solving the Navier-Stokes equations can broadly be classified as being pressure based or density based. Density based algorithms are known to be unstable for low Mach number, incompressible flows. Methods to make density based algorithms suitable for low Mach number flows include preconditioning and adding pseudo-compressibility [1, 2, 3, 4, 5]. Even so, density-based methods remain not very efficient for incompressible flows. Pressure based solvers, with the assumption of constant density, are more suitable for such cases. Pressure based solvers have their own disadvantages. In the incompressible flow equations, there is no explicit equation for pressure. Pressure is solved for in an indirect way through the continuity equation. This leads to a set of four non-linear and coupled equations, with the three velocities and pressure as the unknowns. One approach is to solve for all the unknowns simultaneously. This is known as the direct approach [6, 7, 8]. Such methods require large amount of computer storage and also involve repeated calculations of the coefficients, thereby rendering them non-economical [9].

Another way of handling this is to solve for the velocities and pressure sequentially. This is known as the segregated approach. The velocities are determined from a given pressure field. The crux of this approach is to develop a methodology to improve the guessed pressure so that the resulting velocity field satisfies continuity. The three velocities and pressure are called primitive variables and such methods are often termed as primitive variable formulations. An alternative to primitive variable formulation is to eliminate pressure altogether as is done in the vorticity-streamfunction or vorticity-velocity formulations. But pressure is often an important result required of a CFD simulation and in order to obtain it, an additional Poisson equation needs to be solved.

There are quite a few numerical methods developed using the primitive variable segregated approach. Some of these are the fractional step method [10], penalty method [11, 12, 13, 14], artificial compressibility [4, 15, 16, 17] and pressure correction methods [19]. Harlow and Welch

[18] first introduced a segregated approach using a staggered grid for the primitive variables. This technique was extended by Spalding and Patankar [19] into the SIMPLE (Semi-Implicit Method for Pressure Linked Equations). This method falls under the category of the pressure correction methods, where a pressure correction term is developed which is used to correct the velocity field. This process is repeated until a divergence free velocity field is obtained. Over the years, extensions and variations of SIMPLE have been developed viz. SIMPLER, SIMPLEC, SIMPLEX, etc. Some other pressure correction based methods include PRIME, PISO and CLEAR, reviewed by Moukalled and Darwish [20].

There are basically two ways of describing the location of primitive variables. The first is the collocated approach wherein both velocities and pressure are stored at the same location. As against this, in a staggered grid approach, pressure and velocities are not stored at the same location. From a finite volume standpoint, this means that the control volumes for velocities and pressure are not the same. Collocated variable arrangement is obviously more simple and easy for book keeping, but in the velocity-pressure formulations, this leads to spurious pressure or pressure checkerboard. This means that the method does not make distinction between a uniform and an alternating pressure field. A remedy for such spurious pressure oscillations was developed by Rhie and Chow, who added an artificial diffusion term in the mass conservation equation. This is the basis of the pressure-weighted interpolation method (PWIM) [21, 22]. Another alternative is to use staggered grid arrangement instead, which are known to have good conservation properties without the requirement of any artificial diffusion being added. Staggered grids are easy to implement in a structured framework. However, in an unstructured framework, staggered grid arrangement is not very straightforward as the grid lines are not necessarily parallel to any one of the coordinate axes. As unstructured grids become more popular due to the previously discussed advantages they offer, there is a desire for developing better numerical methods that use unstructured grids. Many researchers attempted the extension of staggered mesh to unstructured grids [23, 24, 25, 26, 27, 28, 28, 29, 30] . However, this approach is often not capable of completely eliminating the problem of spurious pressure oscillations.

An alternative is to use what is known as artificial grid staggering, where pressure is computed at fewer grid points then the velocities. One such approach was developed by Baliga [31], using a Control Volume based Finite Element Method (CVFEM) for spatial discretization. In this method, the calculation domain is discretized into certain geometrical shapes and variables are calculated using element-based interpolation functions, using an element-by-element compilation of the coefficients of the discretized equations. Once the coefficients are assembled, a control volume based conservation principle is employed for deriving the discretized equations. Such methods are capable of handling irregular and multiply connected domains, thereby making them suitable for solving multi-body flow problems like a rotor-fuselage configuration. Due to the control volume based formulation, the methods possess conservative property and render themselves to easy physical interpretation. They are capable of handling flows over the entire Peclet number range and address issues of false diffusion. Because of the artificial grid staggering employed, the CVFEM developed by Baliga [31] is known as the 'unequal-order' CVFEM. While this method satisfactorily solved the problem of checkerboard pressure, it affected the accuracy of the solution as the pressure is computed on a much coarser grid than the velocity. It is not suitable for handling high pressure gradient regions. As an improvement to this, Prakash [32] developed an 'equal-order' CVFEM that computed both the pressure and the velocity over the same grid and later, developed an improved shape function for explicit representation of source terms [33]. In the equal-order approach, the problem of the checkerboard pressure was addressed by developing an artificial velocity field that is dependent on the pressure differences between adjacent grid points. Continuity constraint is imposed on this artificial velocity, instead of the nodal velocity field. Muir and Baliga [34] used the equal-order method for the solution of three-dimensional, steady, convection-diffusion problems using tetrahedral elements.

Recently, Lestari [35] used a CVFEM like method with median-dual control volumes [53] for solving the two-dimensional, unsteady Navier-Stokes equations. Triangular grid elements were used and various implicit and explicit time integration schemes were examined. The current research implements a similar technique for the solution of the time-dependent Navier-Stokes equations. The equal-order interpolation functions used in CVFEM are coupled with a median-dual based finite volume methodology to solve for the primitive variables in a three-dimensional domain. The underlying equations are developed and implemented for a physical domain discretized using tetrahedral elements. The resulting set of discretized equations are solved using the SIMPLER solution technique for pressure-based methods [19]. Apart from applying the 3-D, median-dual based, unsteady flow solver to standard benchmark problems, it is shown to be successful for solving complex rotorcraft flows. A novel unsteady rotor modeling technique, based on the momentum source approach, has been developed in the current work and the integration of the unstructured solver with the unsteady rotor model is presented. The background and details of the rotor model are presented in the next section.

## 1.1 Discrete Blade Unsteady Rotor Model

Rotorcraft flows have proven to be one of the most challenging problems in the field of applied aerodynamics. Unlike a fixed winged aircraft, rotating blades experience a radially increasing linear velocity and thus, an increase in the bound circulation at the tip. This results in a strong tip vortex and complex wake geometry. Moreover, a rotor operates under many complex conditions such as the non-linear viscous flow associated with high-speeds, the effect of the aero-elastic behavior of the rotor and the mutual interference effects from the tail rotor and the fuselage.

The solution of practical problems like helicopter Brownout and aero-acoustics demands a clear understanding of the various aspects of the rotorcraft flowfield and loads. While investigation of rotorcraft aerodynamics using CFD has been in place for many decades now, there is always a need for more accurate, inexpensive and robust computational methods that would enable aerodynamicists to design better rotors and enhance the overall performance of helicopters. In this research, a new unsteady rotor model based on the momentum source approach [54] is developed and integrated with an unstructured solver, also developed as part of the current work, with the potential for solving complex rotorcraft flows.

### 1.1.1 Momentum Source Method: Background

The momentum source approach was first applied to vertical axis wind turbines [36]. The essential feature of the method is that the effect of the rotor is considered only in terms of the momentum that it imparts to the flow. The rotor is, thus, replaced by distributed sources of momentum in the flow. The direction and magnitude of the imparted momentum depend on the rotor geometry and local flow characteristics. The method requires no apriori assumptions about the wake structure and the need for a body-fitted rotor grid on the rotating blades is also eliminated. Use of momentum sources to represent the rotor admittedly compromises the reality of the simulation very close to the blades by not resolving the (chord wise and span wise) boundary layer flow on the rotor. However, the ability to solve practical rotorcraft problems without the need for complex numerical computations has made the momentum source based rotor model very useful. Over the past two decades, Rajagopalan and co-authors [37, 38, 39, 40, 41, 42, 43, 44, 45] have demonstrated the applicability of the model for a wide variety of problems ranging from isolated rotor performance to interference effects due to a full helicopter configuration. The technique of modeling the rotating blades as a distribution of momentum sources in the flowfield has been adopted by various researchers and implemented with different types of flow solvers. For example, the momentum source model was implemented in a finite volume framework to predict rotorcraft aero-acoustical characteristics [56]. The Virtual Blade Model of FLUENT [55] also utilizes the approach of modeling rotating blades as momentum sources placed inside a rotor disk fluid zone, coupled with a general purpose Navier-Stokes solver.

### 1.1.2 Unsteady Rotor Model: Present Research

In all the above references, the momentum source based rotor model is assumed to be steady, wherein the spinning rotor is represented by time-averaged momentum sources in the governing flow equations. What this means is that in such a model, the rotor is represented by momentum sources present throughout the disk plane. The fact that a rotor is actually made up of discrete blades, which change position with time, is not taken into account. While the steady rotor model adequately predicts the loading on the rotor and furnishes a fair approximation of the average rotor performance, it is capable of capturing only time-averaged rotor effects on the flowfield information. It, therefore, does not capture such features of a rotorcraft flow as discrete tip vortices or the unsteady behavior of rotating blades. It is the aim of this research to rectify this limitation of the steady rotor model, thereby making the solution procedure more accurate in predicting the overall performance of rotors and most importantly, capable of capturing a time-accurate flowfield that represents the motion of discrete blades.

In order to obtain a time-accurate flowfield, the movement of the rotating blades needs to be correctly modeled and depending on the instantaneous position of blades, the unsteady momentum source terms need to be computed. These unsteady source terms would then vary with the azimuth and would be added only to the region of the rotor disk plane where the blades are actually present. Recently, Kim et. al. [46] developed an unsteady rotor model based on momentum source method, for studying the unsteady effects of rotor-airframe interactions. The calculation of the momentum source terms was carried out by predicting the induced velocity field using dynamic inflow models. In the current investigation, the unsteady momentum source terms, which are actually the forces exerted by the rotor blades on a fluid element of unit volume, are calculated using classical blade element theory and the induced velocity field is computed as part of the overall solution without the need for any additional inflow models.

The rest of the thesis will describe the aforementioned unstructured flow solver and the unsteady rotor model in detail. In Chapter-2, the theory and equations pertaining to the 3-D, unstructured, median-dual based flow solver are presented. This is followed by the rotor related theory and equations that are given in Chapter-3. Chapter-3 also describes the process of the integration of the unsteady rotor model with the unstructured flow solver. Results and discussions are presented in Chapter-4. In this chapter, first the validation results for the unstructured flow solver are presented, followed by the validation results for the unsteady rotor and results for an isolated rotor solved using the unsteady rotor model integrated with the unstructured flow solver are presented. Finally, Chapter-5 summarizes the current research and enumerates recommendations for future work.

# CHAPTER 2. 3-D UNSTRUCTURED FLOW SOLVER : THEORETICAL FORMULATION

This chapter details the derivation of the 3-D median dual based finite volume method used to solve the governing equations. The current work assumes unsteady, laminar, viscous, incompressible flow.

## 2.1 Governing Equations

The governing equations of the flow are the three-dimensional Navier-Stokes equations. The assumption of incompressible Newtonian fluid results in four unknowns, viz. the velocities in the three dimensions and pressure. The mass and momentum conservation equations are sufficient to model such a flow.

### 2.1.1 Conservation of Mass

For a general fluid, the mass conservation equation, known as the continuity equation, can be represented as follows:

$$\frac{\partial \rho}{\partial t} + \nabla.(\rho \vec{V}) = 0 \tag{2.1}$$

For an incompressible fluid, $\rho$ is constant and the above equation is reduced to:

$$\rho \nabla.(\vec{V}) = 0 \tag{2.2}$$

This can be further expanded in 3-D Cartesian coordinate system as follows:

$$\frac{\partial(\rho u)}{\partial x} + \frac{\partial(\rho v)}{\partial y} + \frac{\partial(\rho w)}{\partial z} = 0 \tag{2.3}$$

where, $u$, $v$ and $w$ are the velocity components in $x$, $y$ and $z$ directions, respectively.

### 2.1.2 Conservation of Momentum

The momentum conservation equation is derived by applying Newton's second law to an infinitesimal fluid control volume. In the divergence form, it looks like:

$$\frac{\partial(\rho\vec{V})}{\partial t} + \nabla.(\rho\vec{V}\vec{V}) = \rho\vec{f} + \nabla.\pi_{ij} \tag{2.4}$$

where, the divergence of the stress tensor $\pi_{ij}$ is given by:

$$\nabla.\pi_{ij} = -(\tilde{I}.\nabla)p - \nabla(\nabla.\tilde{I}) + \nabla.\tilde{\tau} \tag{2.5}$$

In the above equation, the term $\nabla(\nabla.\tilde{I})$ goes to zero for non-orthogonal systems and can, therefore, be ignored. The first term on the right hand side, $(\tilde{I}.\nabla)p$ is the pressure source and reduces to $\nabla p$. The momentum equation now becomes:

$$\frac{\partial(\rho\vec{V})}{\partial t} + \nabla.(\rho\vec{V}\vec{V}) = -\nabla p + \nabla.\tilde{\tau} \tag{2.6}$$

For a Newtonian fluid, the shear stress on a particular fluid element is directly proportional to the rate of deformation. Therefore, for a Newtonian and isotropic fluid, the constitutive relationship for $\tilde{\tau}$ is given by:

$$\tilde{\tau} = \mu\left[\nabla\vec{V} + (\nabla\vec{V})^T - \frac{2}{3}(\nabla.\vec{V})\tilde{I}\right] \tag{2.7}$$

For incompressible fluid, both $(\nabla.\vec{V})$ and $\nabla.(\nabla\vec{V})^T$ vanish. The resulting momentum equation is:

$$\frac{\partial(\rho\vec{V})}{\partial t} + \nabla.(\rho\vec{V}\vec{V}) = -\nabla p + \nabla.(\mu\nabla\vec{V}) \tag{2.8}$$

Assuming constant viscosity and expanding the above equation in 3-D Cartesian coordinate system, the momentum equations in the three coordinate directions are:

$$\frac{\partial(\rho u)}{\partial t} + \frac{\partial(\rho uu)}{\partial x} + \frac{\partial(\rho uv)}{\partial y} + \frac{\partial(\rho uw)}{\partial z} = -\frac{\partial p}{\partial x} + \mu(\frac{\partial^2 u}{\partial x^2} + \frac{\partial^2 u}{\partial y^2} + \frac{\partial^2 u}{\partial z^2}) + S'_x \tag{2.9}$$

$$\frac{\partial(\rho v)}{\partial t} + \frac{\partial(\rho uv)}{\partial x} + \frac{\partial(\rho vv)}{\partial y} + \frac{\partial(\rho vw)}{\partial z} = -\frac{\partial p}{\partial y} + \mu(\frac{\partial^2 v}{\partial x^2} + \frac{\partial^2 v}{\partial y^2} + \frac{\partial^2 v}{\partial z^2}) + S'_y \tag{2.10}$$

$$\frac{\partial(\rho w)}{\partial t} + \frac{\partial(\rho uw)}{\partial x} + \frac{\partial(\rho vw)}{\partial y} + \frac{\partial(\rho ww)}{\partial z} = -\frac{\partial p}{\partial z} + \mu(\frac{\partial^2 w}{\partial x^2} + \frac{\partial^2 w}{\partial y^2} + \frac{\partial^2 w}{\partial z^2}) + S'_z \tag{2.11}$$

where, $S'_x$, $S'_y$ and $S'_z$ are the momentum sources in the three coordinate directions. Let us combine the convective and diffusive fluxes to define a new variable flux $J$ as follows:

$$J_x^u = \rho uu - \mu\frac{\partial u}{\partial x} \qquad J_x^v = \rho uv - \mu\frac{\partial v}{\partial x} \qquad J_x^w = \rho uw - \mu\frac{\partial w}{\partial x} \tag{2.12}$$

$$J_y^u = \rho vu - \mu\frac{\partial u}{\partial y} \qquad J_y^v = \rho vv - \mu\frac{\partial v}{\partial y} \qquad J_y^w = \rho vw - \mu\frac{\partial w}{\partial y} \tag{2.13}$$

$$J_z^u = \rho wu - \mu\frac{\partial u}{\partial z} \qquad J_z^v = \rho wv - \mu\frac{\partial v}{\partial z} \qquad J_z^w = \rho ww - \mu\frac{\partial w}{\partial z} \tag{2.14}$$

Using the definition of this total flux $J$, the momentum equations 2.9 - 2.11 can be rewritten in the following form:

$$\frac{\partial(\rho u)}{\partial t} + \frac{\partial J_x^u}{\partial x} + \frac{\partial J_y^u}{\partial y} + \frac{\partial J_z^u}{\partial z} = S'_x - \frac{\partial p}{\partial x} \tag{2.15}$$

$$\frac{\partial(\rho v)}{\partial t} + \frac{\partial J_x^v}{\partial x} + \frac{\partial J_y^v}{\partial y} + \frac{\partial J_z^v}{\partial z} = S'_y - \frac{\partial p}{\partial y} \tag{2.16}$$

$$\frac{\partial(\rho w)}{\partial t} + \frac{\partial J_x^w}{\partial x} + \frac{\partial J_y^w}{\partial y} + \frac{\partial J_z^w}{\partial z} = S'_z - \frac{\partial p}{\partial z} \tag{2.17}$$

## 2.2 Spatial Discretization

The current work uses a finite volume based spatial discretization scheme. In the finite volume approach, the computational domain is subdivided into control volumes and the conservation laws are satisfied over each of these control volumes. When the conservation laws are integrated over all the control volumes, global conservation is achieved. This research uses a vertex centered method with tetrahedral elements. The three dimensional domain is subdivided into a number of tetrahedrons and median dual based control volumes are constructed around each vertex by joining the centroid of the tetrahedral element to the centers of its faces. This results in non-overlapping control volumes around each vertex, where the primitive variables are stored. Each control volume has triangular shaped control surfaces and the discretization scheme conserves fluxes of the flow variables through each of these control surfaces. The vertex-centered discretization procedure used here is as developed by Baliga and Prakash [33, 34]. Fig. 2.1 shows a tetrahedral element with node points $(P, Q, R, S)$ and Figs. 2.2 and 2.3 illustrate the median-dual based control volume around node $P$. In Fig. 2.2, the three median-duals constructed on face $P-R-S$ by joining the tetrahedral centroid $C_t$, face center $C_f$ and the edge mid points are shown. Following the same procedure, median-dual control volumes are formed around all vertices. Part of such a control-volume around node $P$ is shown in Fig. 2.3.

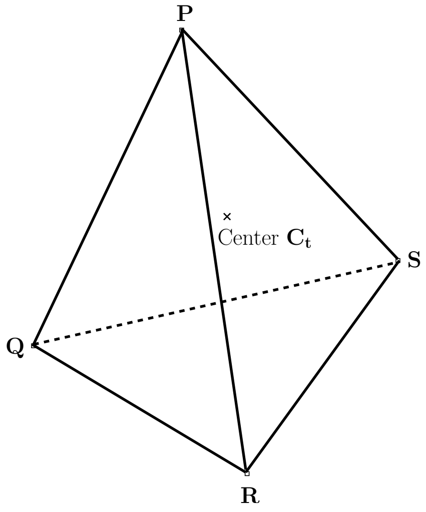

Figure 2.1 Tetrahedral element with centroid at $C_t$

## 2.3 Time Integration Scheme

In the finite volume approach, the governing equations are integrated over every control volume, leading to a set of non-linear algebraic discretized equations, which are then solved for the unknowns. In order to arrive at the final discretized equation, we need to determine the integration and discretization schemes for the different terms in the governing equations. In this section, we discuss the time integration scheme used to integrate the time terms in the Equations 2.15 - 2.17. If $\Phi$ is the variable to be integrated, an assumption is necessary about how it will vary with time from $t$ to $t+\triangle t$. A general scheme for time integration is as follows:

$$\int_t^{t+\triangle t} \Phi \; \mathrm{d}t = [f\Phi + (1-f)\Phi^o] \tag{2.18}$$

where, $\Phi^o$ is the value at time $t$ and $\Phi$ is the value at $t+\triangle t$. From now on, all variables with the superscript ‘o’ will stand for the variable’s value at time $t$. The factor $f$ is the weighting

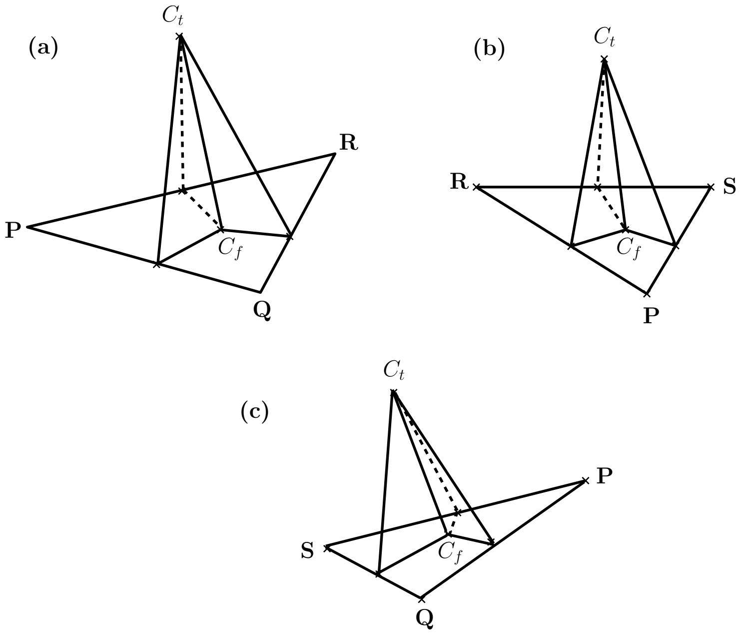

Figure 2.2 Median-dual control volume around node 'P': contribution from neighboring nodes

factor, with $f = 0.5$ leading to the well known Crank-Nicolson scheme and $f = 1$ leading to the fully implicit time integration scheme.

## 2.4 Variable Interpolation Function and Flux Calculation

We will now discuss the formulation of the interpolation functions required to approximate the flow variables and their gradients within a tetrahedral element. Before we do that, we need to make certain assumptions about the profile distribution of the variables within each tetrahedral element. In the present work, the following assumptions are made:

- The density ($\rho$) and viscosity ($\mu$) are assumed to be constant over a tetrahedral element. This ensures continuity of flux of any variable ($\Phi$) over the control surfaces.
- The source term in the $u-$momentum equation ($S'_x$), the $v-$momentum equation ($S'_y$) and the $w-$momentum equation ($S'_z$) are assumed to be constant over a tetrahedral element. In the sections to follow, we shall see that these sources also include the momentum source terms due to the presence of a rotor in the flowfield.
- The pressure $p$ is assumed to vary linearly over each tetrahedral element. This means

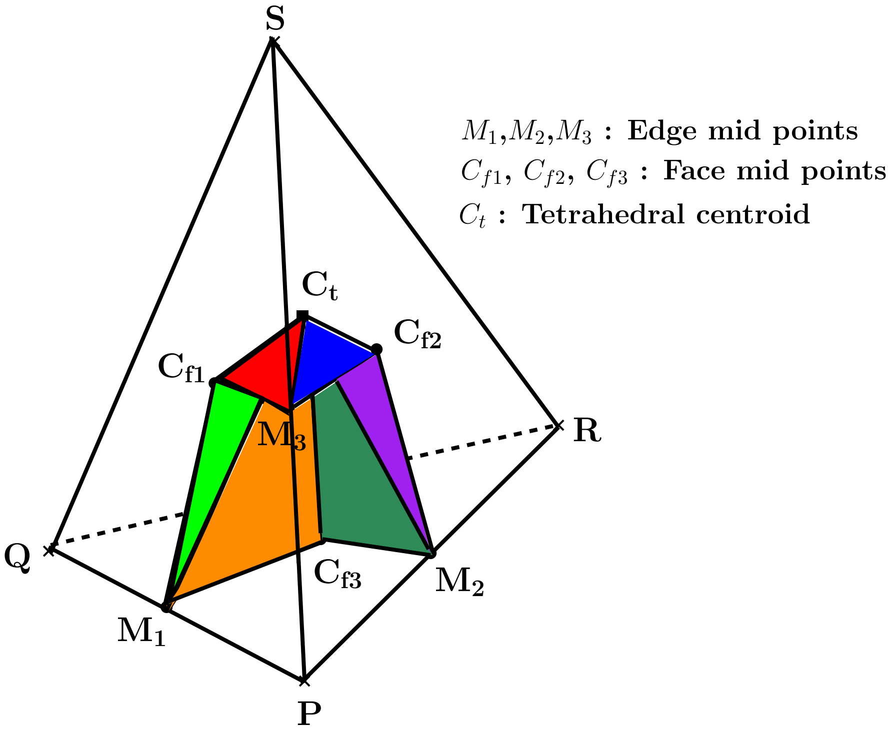

Figure 2.3 Median-dual control volume around node 'P': contribution due to one tetrahedral element

that pressure gradient terms in the three momentum conservation equations are constant over a tetrahedral element.

Interpolation functions are required to compute the fluxes through the control volume surfaces and it is important to choose an appropriate interpolation function that correctly models the physics of the flow and leads to a reasonably accurate numerical solution. For a 1-D convection diffusion problem without any source terms, the exponential function is an exact solution. But the exponential function is very expensive to compute and hence, the power law scheme is chosen here as an approximation of the exponential function. The implementation of the interpolation function is straightforward for a structured grid because the control surfaces are aligned with one of the coordinate directions. But in the case of an unstructured grid, the control surfaces are aligned arbitrarily with respect to the coordinate axes. If not handled properly, this may greatly reduce accuracy especially in high Reynold number flows. Baliga proposed the formulation of a local coordinate system for each tetrahedral element to tackle this problem in unstructured grids. One of the coordinate directions of this local system is aligned with the local average velocity vector within each element, and the other two coordinate directions complete the orthogonal system. This formulation is described in detail below.

### 2.4.1 Local Coordinate System

For each tetrahedral element, the direction of the average velocity vector $\vec{U}_{avg}$ is taken as the local $X$ direction. $(Y, Z)$ are taken so as to complete a mutually perpendicular coordinate system. Fig. 2.4 illustrates a tetrahedral element with node points numbered as $(1, 2, 3, 4)$ and a schematic of the local coordinate system $(X, Y, Z)$. The orientation of the local $(X, Y, Z)$ system with the global $(x, y, z)$ system is given by the following transformation:

- translate $(x, y, z)$ to the tetrahedral centroid $(x_c, y_c, z_c)$
- rotate by angle $\theta'$ about the $y_c$ axis to get $(x_1, y_1, z_1)$
- rotate by an angle $90 - \phi'$ about $z_1$ axis to get the final $(X, Y, Z)$

The transformation angles depend on the local average velocity, given by:

$$cos\phi' = \frac{v_{avg}}{U_{avg}} \qquad cos\theta' = \frac{u_{avg}}{U_{avg} sin\phi'} \tag{2.19}$$

$U_{avg}$ is the magnitude of the resultant average velocity vector through the tetrahedral centroid and $u_{avg}, v_{avg}, w_{avg}$ are its components in the three directions. For the given tetrahedron with node points $(1, 2, 3, 4)$, these are calculated as follows:

$$u_{avg} = (u_1 + u_2 + u_3 + u_4)/4; \quad v_{avg} = (v_1 + v_2 + v_3 + v_4)/4; \quad w_{avg} = (w_1 + w_2 + w_3 + w_4)/4 \tag{2.20}$$

$$U_{avg} = \sqrt{({u_{avg}}^2 + {v_{avg}}^2 + {w_{avg}}^2)} \tag{2.21}$$

The transformation equations are:

$$X = \{(x - x_c)cos\theta' + (z - z_c)sin\theta'\}sin\phi' + (y - y_c)cos\phi' \tag{2.22}$$

$$Y = -\{(x - x_c)cos\theta' + (z - z_c)sin\theta'\}cos\phi' + (y - y_c)sin\phi' \tag{2.23}$$

$$Z = -(x - x_c)sin\theta' + (z - z_c)cos\theta' \tag{2.24}$$

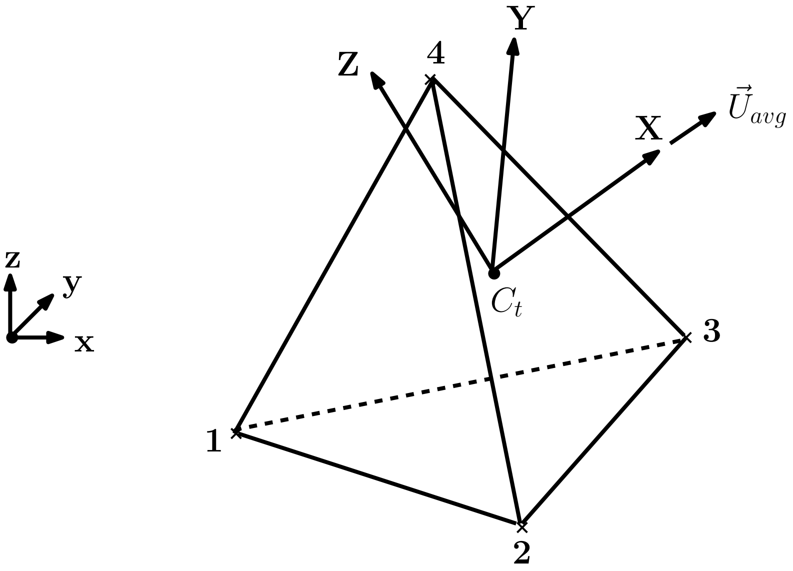

Figure 2.4 Local coordinate system

### 2.4.2 Interpolation Function for a General Variable ‘Φ′

Baliga [34] derived an interpolation function for tetrahedral unstructured meshes that incorporates the 1-D exponential solution and accounts for the three-dimensionality of the flow. A flow variable $\Phi$ is interpolated using the Power Law scheme in the $X$ direction, whereas in the $Y$ and $Z$ directions, it is considered to vary linearly. The interpolation function for a variable $\Phi$ is given by:

$$\Phi = A\xi + BY + CZ + D \tag{2.25}$$

By Power law, we have:

$$\xi = \frac{X - X_{max}}{Pe_{\triangle} + [[0, (1 - 0.1|Pe_{\triangle}|^5)]]} \tag{2.26}$$

where, $Pe_{\triangle}$ is the element Peclet number given by:

$$Pe_{\triangle} = \frac{\rho U_{avg}(X_{max} - X_{min})}{\mu} \tag{2.27}$$

and

$$X_{max} = max(X_1, X_2, X_3, X_4) \qquad X_{min} = min(X_1, X_2, X_3, X_4) \tag{2.28}$$

The coefficients $A, B, C, D$ in Eq. 2.25 are found by satisfying the equation at the four node points of a tetrahedral $1, 2, 3, 4$ (refer to Fig. 2.4). The coefficients can be written in the following form:

$$A = L_1\Phi_1 + L_2\Phi_2 + L_3\Phi_3 + L_4\Phi_4 = \Sigma L_i\Phi_i$$

$$B = M_1\Phi_1 + M_2\Phi_2 + M_3\Phi_3 + M_4\Phi_4 = \Sigma M_i\Phi_i$$

$$C = N_1\Phi_1 + N_2\Phi_2 + N_3\Phi_3 + N_4\Phi_4 = \Sigma N_i\Phi_i$$

$$D = O_1\Phi_1 + O_2\Phi_2 + O_3\Phi_3 + O_4\Phi_4 = \Sigma O_i\Phi_i \tag{2.29}$$

The detailed derivation of the $L_i, M_i, N_i$ and $O_i$ is given in Appendix (A).

### 2.4.3 Flux Computation

Having defined a local coordinate system and the interpolation functions for the flow variables, we are now in a position to calculate the respective flux $J$ through the control surfaces. The derivation is shown here for a general variable $\Phi$, which represents the three velocities $u, v, w$. The total flux of the variable $\Phi$ is given by:

$$J_X^\Phi = \rho u\Phi - \mu\frac{\partial\Phi}{\partial X} \tag{2.30}$$

The fluxes are then expanded using the interpolation function in Eq. 2.25 and the expressions for the coefficients in Eq. 2.29 as follows:

$$J_X^\Phi = \rho u[(\Sigma L_i\Phi_i)\xi + (\Sigma M_i\Phi_i)Y + (\Sigma N_i\Phi_i)Z + (\Sigma O_i\Phi_i)] - \mu[(\Sigma L_i\Phi_i)(\frac{\rho U_{avg}\xi}{\mu} + 1)]$$

$$\Rightarrow \boxed{J_X^\Phi = (\rho f_i - \rho U_{avg}L_i\xi - \mu L_i)\Phi_i} \tag{2.31}$$

where, $i$ stands for a node point and,

$$f_i = u[L_i\xi + M_iY + N_iZ + O_i]$$

Similarly, in the $Y$ and $Z$ directions:

$$J_Y^\Phi = \rho v\Phi - \mu\frac{\partial\Phi}{\partial Y}$$

$$J_Y^{\Phi} = \rho v[(\Sigma L_i\Phi_i)\xi + (\Sigma M_i\Phi_i)Y + (\Sigma N_i\Phi_i)Z + (\Sigma O_i\Phi_i)] - \mu\Sigma M_i\Phi_i$$

$$\Rightarrow \boxed{J_Y^{\Phi} = (\rho g_i - \mu M_i)\Phi_i} \tag{2.32}$$

where,

$$g_i = v[L_i\xi + M_iY + N_iZ + O_i]$$

and

$$J_Z^{\Phi} = \rho w\Phi - \mu\frac{\partial\Phi}{\partial Z}$$

$$J_Z^{\Phi} = \rho w[(\Sigma L_i\Phi_i)\xi + (\Sigma M_i\Phi_i)Y + (\Sigma N_i\Phi_i)Z + (\Sigma O_i\Phi_i)] - \mu\Sigma N_i\Phi_i$$

$$\Rightarrow \boxed{J_Z^{\Phi} = (\rho h_i - \mu N_i)\Phi_i} \tag{2.33}$$

where,

$$h_i = w[\xi L_i + M_iY + N_iZ + O_i]$$

It must be noted that a control volume is made up of triangular shaped median duals. In Fig. 2.5, one such median dual surface between nodes 1 and 3 of a tetrahedron can be seen. The direction of flow over the tetrahedral face $1-2-3$ determines the direction of the normals for each of the median duals constructed on it. Let the normal for a median dual, as represented in Fig. 2.5, be denoted by $(n_x, n_y, n_z)$. We also define the mid points of all the edges of the median dual viz. $r, s, t$. Let the area of the median dual be denoted by $A_{rst}$. The fluxes $J_X^{\Phi}$, $J_Y^{\Phi}$ and $J_Z^{\Phi}$ through the points $r, s$ and $t$ are found. The flux through the median dual is then computed using Gauss's quadrature rule. The flux of any variable "Φ" through the median dual face $r-s-t$ then becomes:

$$\oint_{r-s-t}(\vec{J}.\hat{n})\mathrm{d}S = \frac{A_{rst}}{3}\left[(J_X^r + J_X^s + J_X^t)n_x + (J_Y^r + J_Y^s + J_Y^t)n_y + (J_Z^r + J_Z^s + J_Z^t)n_z\right] \tag{2.34}$$

This procedure is repeated for all the median duals that make up the control volume around a node point.

### 2.4.4 Interpolation Function for Pressure

Pressure is considered to vary linearly in a tetrahedral element. In the global coordinate system, the interpolation function for pressure is:

$$p = -(\alpha x + \beta y + \gamma z + \eta) \tag{2.35}$$

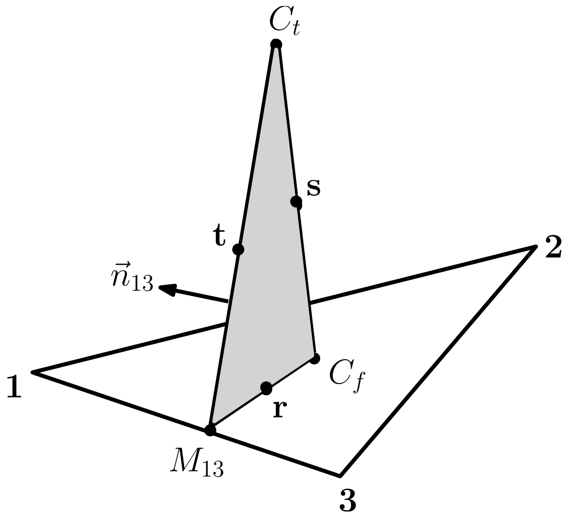

Figure 2.5 Median-dual between two node points

where, $\alpha, \beta, \gamma$ and $\eta$ are coefficients found by satisfying Eq.2.35 at the four node points of the tetrahedron. The details of the derivation are given in Appendix (B). Since pressure is linearly interpolated, the derivatives of pressure within a tetrahedral element are constants. These pressure gradient terms then evaluate to:

$$-\frac{\partial p}{\partial x} = \alpha \qquad -\frac{\partial p}{\partial y} = \beta \qquad -\frac{\partial p}{\partial z} = \gamma \tag{2.36}$$

From Appendix (B), these coefficients and therefore, the pressure gradients can be written in terms of the pressures at the four node points of the tetrahedral element:

$$-\frac{\partial p}{\partial x} = \bar{L}_1 p_1 + \bar{L}_2 p_2 + \bar{L}_3 p_3 + \bar{L}_4 p_4$$

$$-\frac{\partial p}{\partial y} = \bar{M}_1 p_1 + \bar{M}_2 p_2 + \bar{M}_3 p_3 + \bar{M}_4 p_4$$

$$-\frac{\partial p}{\partial z} = \bar{N}_1 p_1 + \bar{N}_2 p_2 + \bar{N}_3 p_3 + \bar{N}_4 p_4 \tag{2.37}$$

## 2.5 Integration and Discretization of the Momentum Equations

Next, the momentum Eqs.2.15-2.17 are integrated to arrive at a set of discretized algebraic equations. Let us denote a representative node by the symbol '$P$' and use the $u$-momentum equation as a model for discretization. The same logic can be easily extended in the other two directions. Integrating Eq. 2.15 over a control volume 'd∀' and over a time interval 'd$t$' :

$$\iint\limits_{\Delta\forall}\left(\frac{\partial(\rho u)}{\partial t}+\frac{\partial J_x^u}{\partial x}+\frac{\partial J_y^u}{\partial y}+\frac{\partial J_z^u}{\partial z}=S_x'-\frac{\partial p}{\partial x}\right)\mathrm{d}\forall\,\mathrm{d}t \tag{2.38}$$

where, '$\Delta\forall$' is the volume of the control volume surrounding the node point '$P$'.

The LHS of the above equation can be written as:

$$\frac{\partial J_x^u}{\partial x}+\frac{\partial J_y^u}{\partial y}+\frac{\partial J_z^u}{\partial z}=\nabla.\vec{J}^u \tag{2.39}$$

We can rewrite the above equation in the local coordinate system as follows:

$$\nabla.\vec{J}^u=\frac{\partial J_X^u}{\partial X}+\frac{\partial J_Y^u}{\partial Y}+\frac{\partial J_Z^u}{\partial Z} \tag{2.40}$$

The integral form of the momentum equation looks like:

$$\iint\limits_{\Delta\forall}\left(\frac{\partial(\rho u)}{\partial t}+\frac{\partial J_X^u}{\partial X}+\frac{\partial J_Y^u}{\partial Y}+\frac{\partial J_Z^u}{\partial Z}=S_x'-\frac{\partial p}{\partial x}\right)\mathrm{d}\forall\,\mathrm{d}t \tag{2.41}$$

Note that the LHS is in terms of the local coordinate system to reduce the amount of false diffusion, while the RHS (i.e. the pressure gradients and the source terms) is cast in the global coordinate system. Gauss's divergence theorem relates the volume integral of a vector $\vec{B}$ over '$\Delta\forall$' to a surface integral.

$$\int_{\Delta\forall}\left(\nabla.\vec{B}\right)\mathrm{d}\forall=\oint_S\left(\vec{B}.\hat{n}\right)\mathrm{d}S \tag{2.42}$$

where, $\hat{n}$ is the outward facing normal to the control surface under consideration. Using Gauss's theorem and the time integration scheme described in a previous section, Eq. 2.41 is transformed into the following form:

$$\frac{\rho(u_p-u_p^o)\Delta\forall}{\triangle t}+f\oint\left(\vec{J}^u.\hat{n}\right)\mathrm{d}S+(1-f)\oint\left(\vec{J}^u.\hat{n}\right)^0\mathrm{d}S=f\left(S_x'-\frac{\partial p}{\partial x}\right)\Delta\forall+(1-f)\left(S_x'-\frac{\partial p}{\partial x}\right)^o\Delta\forall \tag{2.43}$$

### 2.5.1 Integration of the LHS

We use the flux interpolation functions developed in Section 2.4.3 to compute the fluxes in Eq. 2.43. Referring back to Fig. 2.5 and using Gauss's quadrature rule for this median-dual, we get:

$$\oint_{r-s-t} (\vec{J}.\hat{n})\mathrm{d}S = \frac{A_{rst}}{3}\left[(J_X^r + J_X^s + J_X^t)n_x + (J_Y^r + J_Y^s + J_Y^t)n_y + (J_Z^r + J_Z^s + J_Z^t)n_z\right] \tag{2.44}$$

where, $(n_x, n_y, n_z)$ denote the components of the normal vector through the median-dual surface $r-s-t$. The flux around the given node point '$P$' is, therefore, seen to have contributions from all it's neighbors. For example, in Fig. 2.5, grid point-1 has contributions from the nodes 2 and 3 when looking at this particular face. Each triangular face has six median duals constructed on it and as we visit each median-dual in this fashion, we are able to account for the fluxes through all the median-duals and sum up the contributions to each node point. Upon substituting the expressions for the fluxes and collecting all the terms pertaining to a grid point together, the LHS looks like:

$$\begin{aligned} LHS = \frac{\rho\big(u_p - u_p^o\big)\forall}{\triangle t} + f(a_P u_P - \sum_{i=1}^{N} a_{nb}u_{nb}) + \\ (1-f)\big(a_P u_P - \sum_{i=1}^{N} a_{nb}u_{nb}\big)^o \end{aligned} \tag{2.45}$$

In the above equation, '$a_P$' is the collection of terms pertaining to the node '$P$', while '$a_{nb}$' denotes the contributions from all it's neighboring nodes. '$N$' stands for the number of neighbors of node '$P$'.

### 2.5.2 Integration of the RHS

The interpolation function for pressure was discussed in Section 2.4.4. The source term $S_x'$ is assumed to be constant over a tetrahedral element. For a node point '$P$', we assemble the pressure gradient terms by accounting for the contribution from all its neighbors. If each node point is shared by '$m$' number of tetrahedrons, then each of these tetrahedrons will contribute towards the source term for the given node point. The RHS then becomes:

$$RHS = \Delta\forall \sum_{i=1}^{m} \big[f\{{S_X}' + \bar{L_1}p_1 + \bar{L_2}p_2 + \bar{L_3}p_3 + \bar{L_4}p_4\} + (1-f)\{{S_X}' + \bar{L_1}p_1 + \bar{L_2}p_2 + \bar{L_3}p_3 + \bar{L_4}p_4\}^o\big] \tag{2.46}$$

### 2.5.3 Total Discretization Equation

Combining Eqs. 2.45 and 2.46, we get the final $u$-momentum equation for a grid point '$P$' as follows:

$$\boxed{a_p u_p = f\{\sum_{i}^{N} a_{nb} u_{nb}\} + b_u^o + b_u} \tag{2.47}$$

where;

$$a_p = \frac{\rho\Delta\forall}{\triangle t} + f a_p$$

$$b_u^o = \big[\frac{\rho\Delta\forall}{\triangle t} - (1-f)a_P\big]{u_P}^o + (1-f)(\sum_{i=1}^{N} a_{nb} u_{nb})^o$$
$$+ (1-f)\Delta\forall\sum_{i=1}^{m}\{{S_X}' + \bar{L_1}p_1 + \bar{L_2}p_2 + \bar{L_3}p_3 + \bar{L_4}p_4\}^o$$

$$b_u = f\sum_{i=1}^{m}\{{S_X}' + \bar{L_1}p_1 + \bar{L_2}p_2 + \bar{L_3}p_3 + \bar{L_4}p_4\}\Delta\forall \tag{2.48}$$

In Eq. 2.48, '$N$' stands for the number of node neighbors of grid point '$P$' and '$m$' is the number of tetrahedral elements of which node '$P$' is a part. The $v$ and $w$ momentum equations can be developed in the same manner.

### 2.5.4 Boundary Condition

The discretized equations are modified at the boundaries to account for the prescribed values at the boundary faces. There can be two types of boundary conditions:

- given $\Phi$ $(u, v, w)$
- given flux $F^{\Phi}$

The boundary stencil is accordingly modified as follows:

$$a_p\Phi_p = f\{\sum_{i}^{N} a_{nb}\Phi_{nb}\} + b_{\Phi} - F_p^{\Phi} + \dot{m}_p\Phi_p \tag{2.49}$$

where, $F_p^{\Phi}$ is the flux of the variable $\Phi$, $\dot{m}_p$ is the mass flux leaving the domain through the boundary face. In case of the boundary condition where the value of $\Phi$ is specified at a boundary node '$P$', Eq. 2.49 is used to find the boundary flux $F_p^{\Phi}$. Whereas, in case of boundary flux being the known quantity, then Eq. 2.49 is used to find the value of the variable $\Phi$ at the boundary nodes.

## 2.6 Velocity-Pressure Coupling and Implementation

In the previous section, the three discretized momentum equations in four unknowns namely the velocities $u, v, w$ and pressure $p$, were developed. So far, we do not have an explicit equation governing the pressure field. In the finite volume based SIMPLER approach by Patankar [19], pressure is obtained indirectly through the continuity equation. However, if special care is not taken in developing this equation in the unstructured framework, it can lead to spurious pressure fields like checkerboard pressure. Baliga [31] introduced the unequal order method for this purpose, which is similar to the staggered grid formulation in the structured framework. Under the unequal order method, each tetrahedral element is further divided to four tetrahedrons. The pressure solution points coincide with the main grid points, while the velocities are solved on the grid resulting from the subdivision. While such an approach was effective in checking phenomenon like checkerboard pressures, it meant that the pressure was being solved on a coarser grid than the velocities, which resulted in reduced accuracy. As a solution to this, Prakash and Patankar [32] developed the equal order velocity-pressure interpolation method, which allows for the pressure and velocities to be solved on the same grid, albeit with some required modifications to prevent spurious solutions. The basic idea of the equal order method is that the velocity field used to solve the continuity equation should be dependent on the pressure differences between adjacent grid points. The velocities are, therefore, modified in order to ensure that checkerboard pressure fields are not permissible and that mass conservation criteria is satisfied. This modified velocity field is termed as the "artificial" velocity here and the procedure to derive such an artificial velocity field is discussed below.

### 2.6.1 Definition of Pseudo Velocities $(\hat{u}, \hat{v}, \hat{w})$ and Source Term Coefficients $(d^u, d^v, d^w)$

In order to develop an artificial velocity field, we first introduce the concept of pseudo velocities and the source term coefficients. Once again, we shall show all derivations with respect to the $u$-momentum equation and the same logic can be followed with the other two momentum equations. From Eqs. 2.47 and 2.48, the $u$-velocity can be written as:

$$u_p = \frac{f \sum_{i=1}^{N}(a_{nb}u_{nb}) + b_u^o}{a_p^u} + \frac{\forall\{{S_X}' + \bar{L_1}p_1 + \bar{L_2}p_2 + \bar{L_3}p_3 + \bar{L_4}p_4\}f}{a_p^u} \tag{2.50}$$

The pseudo $u$ velocity at node '$P$' is then defined as:

$$\hat{u}_p = \frac{f \sum_{i=1}^{N}(a_{nb}u_{nb}) + b_u^o}{a_p^u} \tag{2.51}$$

where, '$N$' stands for the summation over node neighbors of node $P$. We define the coefficient associated with the source terms as follows:

$$d_p^u = \frac{\forall}{a_p^u} \tag{2.52}$$

where, $\forall$ is the control volume surrounding node $P$. The $v$ and $w$ pseudo velocities and the source term coefficients can be found in a similar manner. It is assumed that these pseudo velocities $(\hat{u}, \hat{v}, \hat{w})$ and the source term coefficients $(d^u, d^v, d^w)$ vary linearly within a tetrahedral element.

### 2.6.2 Definition of the Artificial Velocity Field

The artificial velocity, as shown in Fig. 2.6, is denoted by $\vec{\tilde{U}}$ and is defined for a tetrahedral element as given below:

$$\vec{\tilde{U}} = \tilde{u}\hat{i} + \tilde{v}\hat{j} + \tilde{w}\hat{k} \tag{2.53}$$

where, the velocity components are defined as:

$$\begin{aligned}
\tilde{u} &= \hat{u} + d^u\big(S'_x - \frac{\partial p}{\partial x}\big) \\
\tilde{v} &= \hat{v} + d^v\big(S'_y - \frac{\partial p}{\partial y}\big) \\
\tilde{w} &= \hat{w} + d^w\big(S'_z - \frac{\partial p}{\partial z}\big)
\end{aligned} \tag{2.54}$$

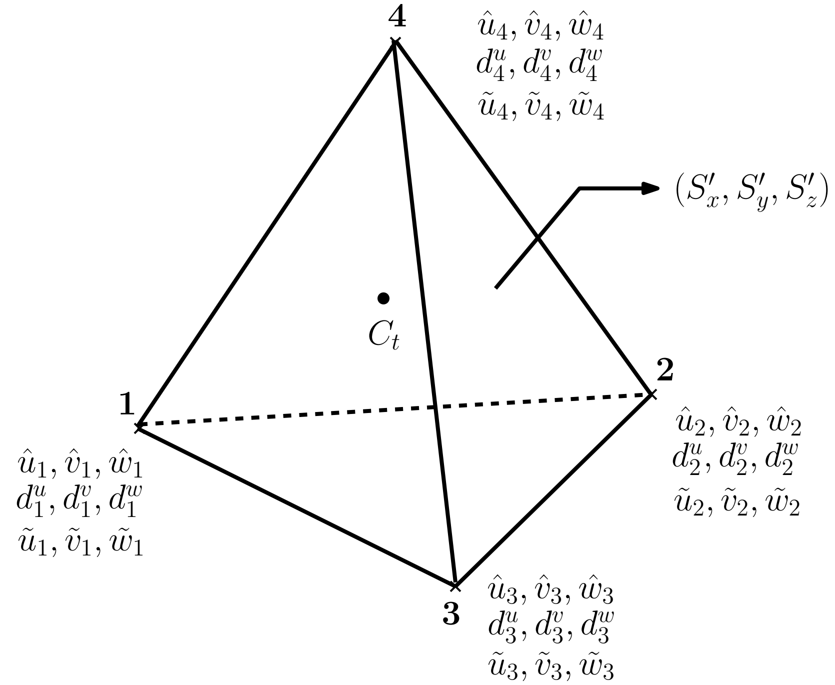

Figure 2.6 Artificial velocity interpolation in a tetrahedral element

Using the definitions of the pseudo velocities and the source term coefficients, the artificial velocities for a node point '$P$' becomes:

$$\tilde{u}_p = \hat{u}_p + d_p^u\{f \sum_{i=1}^{m}(S'_x + \bar{L}_1 p_1 + \bar{L}_2 p_2 + \bar{L}_3 p_3 + \bar{L}_4 p_4)\}$$

$$\tilde{v}_p = \hat{v}_p + d_p^v\{f \sum_{i=1}^{m}(S'_y + \bar{M}_1 p_1 + \bar{M}_2 p_2 + \bar{M}_3 p_3 + \bar{M}_4 p_4)\}$$

$$\tilde{w}_p = \hat{w}_p + d_p^w\{f \sum_{i=1}^{m}(S'_z + \bar{N}_1 p_1 + \bar{N}_2 p_2 + \bar{N}_3 p_3 + \bar{N}_4 p_4)\} \tag{2.55}$$

As can be seen from the above equations, the artificial velocity field is dependent on the surrounding pressure values. In the present method, it is the artificial velocity field, and not the nodal velocity, that is used to satisfy the continuity criteria and the resulting equation is then solved to find the pressure, ensuring that checkerboard pressure fields are not a permissible solution. Since it is the artificial velocity field that is used to solve the mass conservation equation, the coefficients of the momentum equations are also cast in terms of this mass conserving artificial velocity field to preserve overall conservation. The derivation of the coefficients of the momentum equations has already been covered in Section 2.5. The following sections show

how the coefficients are re-cast in terms of the artificial velocity, followed by the derivation of a pressure equation from the continuity equation.

### 2.6.3 Interpolation of the Artificial Velocity at the Control Volume Faces

To find the coefficients of the momentum equations in terms of the artificial velocity field, the same steps as were taken while developing the coefficients using the nodal velocity field are followed. The local coordinate system is found using Eqs. 2.20 - 2.22, but with the nodal velocities $(u, v, w)$ replaced by $(\tilde{u}, \tilde{v}, \tilde{w})$. In order to find the fluxes through the median-dual control surfaces, we need to find the artificial velocities through each of these median-duals. Referring back to Fig. 2.5, the artificial velocity values at the points $r, s$ and $t$ need to be found. It has already been stated that the pseudo velocities and the source term coefficients vary linearly within a tetrahedral element, which means that the artificial velocity field can also be linearly interpolated within a tetrahedral element. In Fig. 2.5, the artificial velocities at the three node points that make up the tetrahedral face $1-2-3$ are:

$$\begin{aligned}
\tilde{u}_1 &= \hat{u}_1 + d_1^u\{f\sum_{i=1}^{m}(S_x' + \bar{L_1}p_1 + \bar{L_2}p_2 + \bar{L_3}p_3 + \bar{L_4}p_4)\} \\
\tilde{u}_2 &= \hat{u}_2 + d_2^u\{f\sum_{i=1}^{m}(S_x' + \bar{L_1}p_1 + \bar{L_2}p_2 + \bar{L_3}p_3 + \bar{L_4}p_4)\} \\
\tilde{u}_3 &= \hat{u}_3 + d_3^u\{f\sum_{i=1}^{m}(S_x' + \bar{L_1}p_1 + \bar{L_2}p_2 + \bar{L_3}p_3 + \bar{L_4}p_4)\}
\end{aligned} \tag{2.56}$$

where, number '4' denotes the fourth node point of the tetrahedron of which face $1-2-3$ is a part. The $\tilde{v}$ and $\tilde{w}$ components can be accordingly found. The artificial velocity at the center of the face '$cf$' and the tetrahedron center '$ct$' is found as follows:

$$\tilde{u}_{cf} = \frac{\tilde{u}_1 + \tilde{u}_2 + \tilde{u}_3}{3} \tag{2.57}$$

$$\tilde{u}_{ct} = \frac{\tilde{u}_1 + \tilde{u}_2 + \tilde{u}_3 + \tilde{u}_4}{4} \tag{2.58}$$

With the values at the three face vertices, the face center and the tetrahedron centroid known, linear interpolation is used to find the values at the corners of the median-dual $r-s-t$.

- Artificial velocity through ’$r$’

$$\vec{\tilde{U}}_r = \frac{5(\vec{\tilde{U}}_1 + \vec{\tilde{U}}_3) + 2\vec{\tilde{U}}_2}{12} \tag{2.59}$$

- Artificial velocity through ‘$s$’

$$\vec{\tilde{U}}_s = \frac{7(\vec{\tilde{U}}_1 + \vec{\tilde{U}}_2 + \vec{\tilde{U}}_3) + 3\vec{\tilde{U}}_4}{24} \tag{2.60}$$

- Artificial velocity through ‘$t$’

$$\vec{\tilde{U}}_t = \frac{3(\vec{\tilde{U}}_1 + \vec{\tilde{U}}_3) + (\vec{\tilde{U}}_2 + \vec{\tilde{U}}_4)}{8} \tag{2.61}$$

In this manner, all the median-duals are traversed to first calculate the artificial velocities through them, which are in turn used to compute the coefficients of the momentum equations according to Eqs. 2.44-2.47.

## 2.7 Pressure Equation

The basic idea in the present method is to use the artificial velocity field $\vec{\tilde{U}}$ in the continuity equation and cast it as an equation for pressure. The continuity equation written for a median-dual, as depicted in Fig. 2.5, is given by:

$$\int_{r-s-t} \rho \vec{\tilde{U}}.\hat{n} \mathrm{d}S = 0 \tag{2.62}$$

where, $\vec{\tilde{U}}$ is the artificial velocity vector through the center of the median-dual face. Expanding further, the equation becomes:

$$\rho\left[ (\frac{\tilde{u}_r + \tilde{u}_s + \tilde{u}_t}{3}) n_x + (\frac{\tilde{v}_r + \tilde{v}_s + \tilde{v}_t}{3}) n_y + (\frac{\tilde{w}_r + \tilde{w}_s + \tilde{w}_t}{3}) n_z \right] = 0 \tag{2.63}$$

Substitution and expansion of the artificial velocity expressions in the above equation yields the coefficients of the pressure equation. Assembling the coefficients for a node point $Q$, taking into account the contribution from neighboring nodes, the pressure equation can be written as:

$$\boxed{a'_Q p_Q = \sum_{i=1}^{N} (a'_{nb} p_{nb}) + b_p} \tag{2.64}$$

where, $a'_Q$ is the collection of all the terms pertaining to node '$Q$', while $a'_{nb}$ represents the contribution from all its neighbors. $b_P$ is a collection of all the other remaining terms that make up the source term for the pressure equation. A derivation of the above equation is given in Appendix(C).

### 2.7.1 Pressure Equation for the Boundaries

For the boundary, the discretized pressure equation needs to be modified to account for the mass flow leaving the boundary face. This is done by subtracting the mass flux $\dot{m}_Q$ from the right hand side of the pressure equation to yield the following equation:

$$a'_Q p_Q = \sum_{i=1}^{N} (a'_{nb} p_{nb}) + b_p - \dot{m}_Q \tag{2.65}$$

where, point '$Q$' now represents a boundary node.

## 2.8 Pressure Correction

The momentum and pressure equations developed so far are sufficient to solve for the three velocities and pressure. In general, the velocities obtained at the end of a solution iteration will not satisfy the continuity equation and until they do, the solution is said to be not converged. The convergence of the solution procedure can be accelerated by using a pressure correction equation at every iteration. This pressure correction is used to correct the velocities in order to obtain a velocity field that satisfies the mass conservation equation. This is especially useful in the present method wherein mass conservation equation is solved using the artificial velocity field and therefore, does not directly affect the nodal velocities. Patankar [19] popularized such a pressure correction technique named the SIMPLER algorithm, which is adopted here.

If the pressure field $p^*$ is used to solve for the velocities $u^*, v^*$ and $w^*$, then we use these to find the artificial velocities as follows:

$$\begin{aligned}
\tilde{u}^* &= \hat{u}^* + d^u\big(S'_x - \frac{\partial p^*}{\partial x}\big) \\
\tilde{v}^* &= \hat{v}^* + d^v\big(S'_y - \frac{\partial p^*}{\partial y}\big) \\
\tilde{w}^* &= \hat{w}^* + d^w\big(S'_z - \frac{\partial p^*}{\partial z}\big)
\end{aligned} \tag{2.66}$$

This star scripted velocity field is a guessed value and it will not satisfy the continuity equation. Let the pressure correction be denoted by $p'$. Then the corrected pressure is given by:

$$p = p * + p' \tag{2.67}$$

With this corrected pressure, the artificial velocities that satisfy the continuity equation are:

$$\begin{aligned} \tilde{u} &= \hat{u}^* + d^u \left( S'_x - \frac{\partial (p^* + p')}{\partial x} \right) \\ \tilde{v} &= \hat{v}^* + d^v \left( S'_y - \frac{\partial (p^* + p')}{\partial y} \right) \\ \tilde{w} &= \hat{w}^* + d^w \left( S'_z - \frac{\partial (p^* + p')}{\partial z} \right) \end{aligned} \tag{2.68}$$

If the velocities are rewritten as starred velocity plus a correction term:

$$\begin{aligned} \tilde{u} &= \tilde{u}^* + \tilde{u}' \\ \tilde{v} &= \tilde{v}^* + \tilde{v}' \\ \tilde{w} &= \tilde{w}^* + \tilde{w}' \end{aligned} \tag{2.69}$$

From Eq. 2.68, the corrected velocities are given by:

$$\begin{aligned} \tilde{u}' &= -d^u \left( \frac{\partial p'}{\partial x} \right) \\ \tilde{v}' &= -d^v \left( \frac{\partial p'}{\partial y} \right) \\ \tilde{w}' &= -d^w \left( \frac{\partial p'}{\partial z} \right) \end{aligned} \tag{2.70}$$

If we compare the above equations with the pressure equation, the difference is only in the source term. For the pressure correction equation, the source terms used in the pressure equation are replaced by the following terms:

$$\begin{aligned} S^u_{p'} &= S'_x - \frac{\partial p^*}{\partial x} \\ S^v_{p'} &= S'_y - \frac{\partial p^*}{\partial y} \\ S^w_{p'} &= S'_z - \frac{\partial p^*}{\partial z} \end{aligned} \tag{2.71}$$

and also, $\hat{u}, \hat{v}$ and $\hat{w}$ are replaced by $\hat{u}^*, \hat{v}^*$ and $\hat{w}^*$, respectively. The pressure correction equation for a node '$Q$', therefore, becomes:

$$a'_Q p'_Q = \sum_{i=1}^{N} (a'_{nb} p'_{nb}) + b'_p \tag{2.72}$$

For a boundary node, this gets modified to account for the mass flux and takes the following form:

$$a'_Q p'_Q = \sum_{i=1}^{N} (a'_{nb} p'_{nb}) + b'_p - \dot{m}_Q \tag{2.73}$$

where, $a'_Q$ and $a'_{nb}$ are the same coefficients as used in the pressure equation. Once the pressure correction $p'$ is obtained, the corrected artificial velocity field $\vec{\tilde{U}}'$ can be found and used to correct the nodal velocities. Prakash [33] developed the following velocity correction formula for a representative node point '$Q$':

$$u'_Q = \frac{-d^u_Q}{\Delta\forall_Q} \sum_{i=1}^{m} \Delta\forall_i (\frac{\partial p'}{\partial x})_i$$

$$v'_Q = \frac{-d^v_Q}{\Delta\forall_Q} \sum_{i=1}^{m} \Delta\forall_i (\frac{\partial p'}{\partial y})_i$$

$$w'_Q = \frac{-d^w_Q}{\Delta\forall_Q} \sum_{i=1}^{m} \Delta\forall_i (\frac{\partial p'}{\partial z})_i \tag{2.74}$$

where, '$\Delta\forall_Q$' is the volume of the control volume around node $Q$ and '$m$' runs over the number of tetrahedral elements around node $Q$. The nodal velocities can then be corrected as follows:

$$u_Q = u^*_Q + u'_Q$$

$$v_Q = v^*_Q + v'_Q$$

$$w_Q = w^*_Q + w'_Q \tag{2.75}$$

The boundary velocities are not corrected because it would change the prescribed boundary condition.

## 2.9 Relaxation

In the above development, three momentum equations, a pressure equation and a pressure correction equation were derived. These discretized equations are solved using Gauss Seidel iteration technique with alternate sweeps over the computational domain to ensure convergence. In order to accelerate convergence of the solution procedure, an external relaxation is enforced on the discretized equations. Let the relaxation factor be denoted by $\beta'$. Then a relaxed equation for a general variable '$\Phi$' at a node $P$ becomes:

$$a_p\Phi_p = \beta'\big[f\sum_{i=1}^{N} a_{nb}\Phi_{nb} + b_\Phi\big] + a_p(1-\beta')\Phi_p^o \tag{2.76}$$

where, $a_p$, $a_{nb}$ and $b_\Phi$ have their usual meaning. Note that the pressure correction equation is not relaxed. For SIMPLER based algorithms, it has been found from previous research [19] that an under-relaxation is required for acceleration of the solution process. This means that the value of the relaxation factor should be less than one i.e. $\beta' \leq 1$.

# CHAPTER 3. UNSTEADY ROTOR MODEL FOR DISCRETE BLADES

In the previous chapter, the modeling of the governing equations using a finite volume median-dual based methodology was discussed. In this chapter, the rotor modeling technique that is used in conjunction with the flow solver to simulate rotorcraft flows is described. The development of the rotor sources $(S'_x, S'_y, S'_z)$ and their coupling with the discretized momentum conservation equations are explained.

## 3.1 Momentum Source Method

The present work uses the momentum source method to model the effect of a rotor [36]. According to the momentum source approach, which was first applied to vertical axis wind turbines, the function of a rotating rotor is to impart momentum to the flow. The rotor is, thus, replaced by distributed sources of momentum in the flow. The direction and magnitude of the imparted momentum depend on the rotor geometry and local flow characteristics. The advantages of this method are that it requires no apriori assumption about the wake structure and the need for a body-fitted rotor grid is also eliminated. Use of momentum sources to represent the rotor admittedly compromises the reality of the simulation very close to the surface by not resolving the (chord wise and span wise) boundary layer flow on the rotor. However, the versatility of the method that makes it compatible with a variety of flow solvers and its ability to solve rotorcraft flows economically has made this approach a very attractive technique for rotor modeling.

The original version of the rotor model using momentum source approach was steady in nature, wherein the spinning rotor was represented by time-averaged momentum sources. In the current work, a time-accurate, unsteady momentum source based rotor model, that has certain advantages over its earlier version, has been developed and implemented. Before we go into the details of the unsteady rotor model itself, it would be worthwhile to take a look at the steady rotor model and its scope.

## 3.2 Steady Rotor Model

In the steady rotor model, the rotor is treated as a solid disk with blades present throughout the rotor disk plane. The fact that a rotor is actually made up of discrete blades, which change position with time, is not taken into account. The rotor disk is discretized into concentric circles centered at the rotor center. The control volumes of the computational domain with which the entire rotor disk intersects are determined and this process is completed before the time iterations of the unsteady flow solver start and is not repeated again. At any given instant in time, the rotor forces are determined using the currently available velocity field. The question of where and how to add this rotor source term in the computational domain now arises. It must be noted here that a practical rotor is not a disk, but is made up of discrete blades. However, the steady rotor model does not consider the presence of discrete blades. It does not determine the instantaneous location of each rotor blade as the rotor rotates, instead approximates the blades to be present throughout the disk plane. This means that at every instant in time, the steady rotor model adds a unique source term to each control volume intersected by the entire disk plane. This results in time-averaging of the rotor's influence. For an $N_b$-bladed rotor, the time averaged rotor source term $\vec{S} = (S'_x, S'_y, S'_z)$ to be added to the discretized momentum equations is:

$$\vec{S} = \frac{N_b \Delta\theta}{2\pi}(-\vec{F}) \tag{3.1}$$

where, $\Delta\theta$ is the distance that a blade would travel while traversing through a control volume and $-\vec{F}$ is the instantaneous force acting on that control volume, which depends on the velocity field. The source term is averaged over $2\pi$ to account for the fact that the rotor has been modeled as a disk and this source term is now added to all the control volumes intersected by the rotor disk plane. Therefore, at every instant in time, the influence of the rotor is felt throughout the disk plane and this results in an averaged flow field. While such time-averaged momentum source modeling is adequate to predict overall blade loading, it is not capable of capturing the discrete unsteady features of a rotorcraft flow like blade passage effects. This leads to the need for a rotor model that accounts for discrete blade aerodynamics of a rotorcraft flow. Such a model has been developed in this work and the details are given in the following sections.

## 3.3 Unsteady Rotor Model for Discrete Blades

The effect of a rotating rotor is to impart momentum to the flow. The direction and magnitude of the imparted momentum depend on the characteristics of the rotating blades and the aerodynamic forces exerted by them. The process of evaluating such a momentum-based influence of the rotor can be broken down into two sub-processes. The first sub-process is to determine the region of the computational domain where such an influence has to be added. In the current research, this step is termed as finding the rotor “intersections” with the computational domain. The second task is to determine the magnitude of the rotor source itself that acts in these specific rotor intersected regions.

### 3.3.1 Coordinate Systems

The implementation of the above methodology requires the description of the rotor geometry, which is done by using four different coordinate systems. An explanation of these coordinate systems and mutual transformations between them are now presented.

#### 3.3.1.1 Computational Domain Coordinates

The governing equations are solved in an unstructured framework, where the three coordinate directions are denoted by $(x, y, z)$, with unit vectors $\hat{\imath}$, $\hat{\jmath}$ and $\hat{k}$. In this system, the center of the rotor is designated by $(x_c, y_c, z_c)$ and the axis of rotation is perpendicular to the disk, along $\vec{\Omega}$ where

$$\vec{\Omega} = \Omega_1 \hat{\imath} + \Omega_2 \hat{\jmath} + \Omega_3 \hat{k} \tag{3.2}$$

and $|\vec{\Omega}| = \Omega$ is the rotational speed in radians per second.

#### 3.3.1.2 Rotor Based Cartesian System

The computational coordinate system is aligned such that one axis is along the freestream velocity and the other two axes are mutually perpendicular to it. But the rotor is usually at an arbitrary orientation with respect to the freestream. This results in the need for a rotor based coordinate system that can be related to the computational coordinate system. The rotor based Cartesian coordinate system $(\xi, \eta, \zeta)$ has its origin at the rotor center and the axis $\xi$ points in the direction perpendicular to the rotor disk plane, as shown in Fig. 3.1. To form a mutually perpendicular right handed coordinate system, axes $\eta$ and $\zeta$ have to lie in the plane of the rotor. The transformation from this rotor based Cartesian coordinate system to the computational coordinate system can be achieved by first translating the origin and then using the method of Euler angle rotations. This is given below.

$$\begin{bmatrix} \xi \\ \eta \\ \zeta \end{bmatrix} = \begin{bmatrix} \cos B & \sin A \sin B & -\cos A \sin B \\ 0 & \cos A & \sin A \\ \sin B & -\sin A \cos B & \cos A \cos B \end{bmatrix} \times \begin{bmatrix} x - x_c \\ y - y_c \\ z - z_c \end{bmatrix} = \mathbf{M_1} \times \begin{bmatrix} x - x_c \\ y - y_c \\ z - z_c \end{bmatrix} \tag{3.3}$$

where, angle '$B$' denotes the tilt of the rotor with respect to the computational coordinate system and angle '$A$' denotes its sideslip. A rigorous derivation of the above transformation is given in Ref. [40].

#### 3.3.1.3 Rotor Based Cylindrical Polar Coordinate System

For the purpose of convenience in defining the rotor, we further define a rotor based cylindrical polar coordinate system $(r, \theta, z)$ as shown in Fig. 3.2. In this system, the $z$ axis is aligned along $\xi$, $r$ points radially outwards and $\theta$ is such that:

$$\theta = \frac{\pi}{2} - \psi \tag{3.4}$$

where, $\psi$ is the azimuthal angle of the rotor taken anticlockwise from the positive $x$ axis. The unit vectors in this system are related to those in the $(\xi, \eta, \zeta)$ system by the following matrix

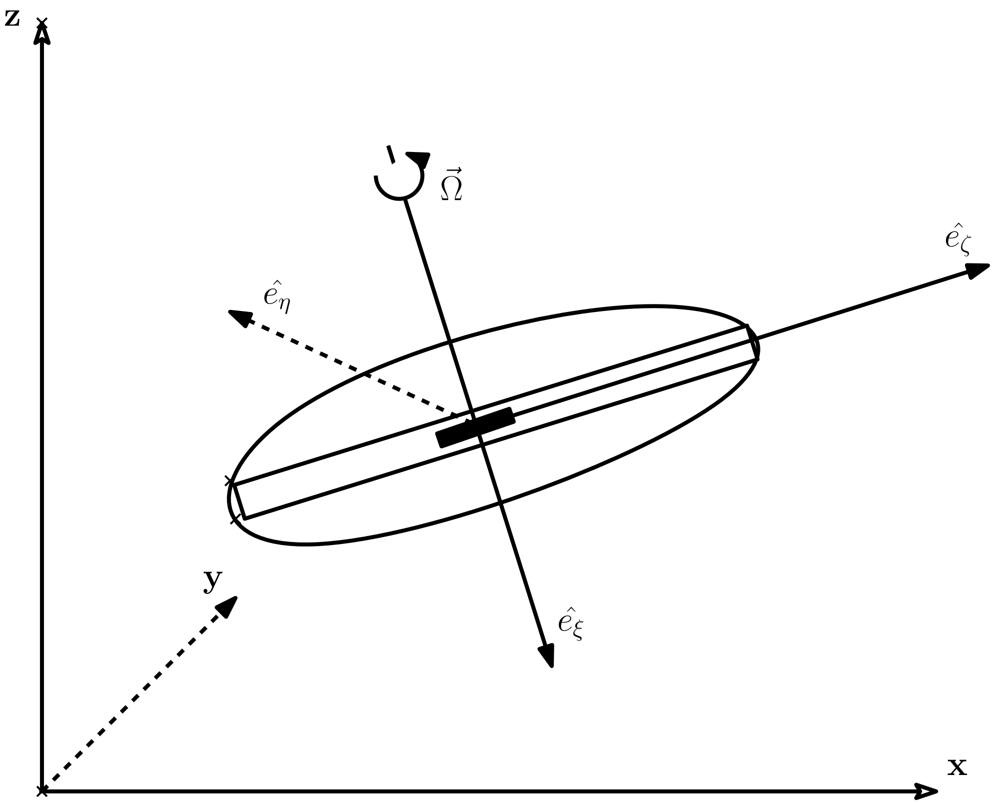

Figure 3.1 Rotor based Cartesian coordinate system

relation.

$$\begin{bmatrix} \hat{e}_r \\ \hat{e}_\theta \\ \hat{e}_z \end{bmatrix} = \begin{bmatrix} 0 & \cos\theta & \sin\theta \\ 0 & -\sin\theta & \cos\theta \\ 1 & 0 & 0 \end{bmatrix} \times \begin{bmatrix} \hat{e}_\xi \\ \hat{e}_\eta \\ \hat{e}_\zeta \end{bmatrix} = \mathbf{M_2} \times \begin{bmatrix} \hat{e}_\xi \\ \hat{e}_\eta \\ \hat{e}_\zeta \end{bmatrix} \tag{3.5}$$

In case the rotor blade has a deflection with respect to the plane of rotation [1], we further define a blade fixed coordinate system $(n, \theta, s)$, where $s$ is in the spanwise direction of the blade or in other words, it is the locus of the centers of pressure of the airfoil sections. $\hat{e}_\theta$ is the same as in the previous system and $\hat{e}_n$ is defined to complete the right handed system. A curved blade is depicted in Fig. 3.3.

Thus, the $(n, s)$ axes always lie in the $r$-$z$ plane and if there is no deflection i.e. $\delta = 0$, then the $n$ axis becomes opposite to $z$ while the $s$ axis coincides with $r$. The transformation between

---

[1] Since the current procedure does not model the structural dynamics of the blades, the deflections, if any, need to be specified apriori.

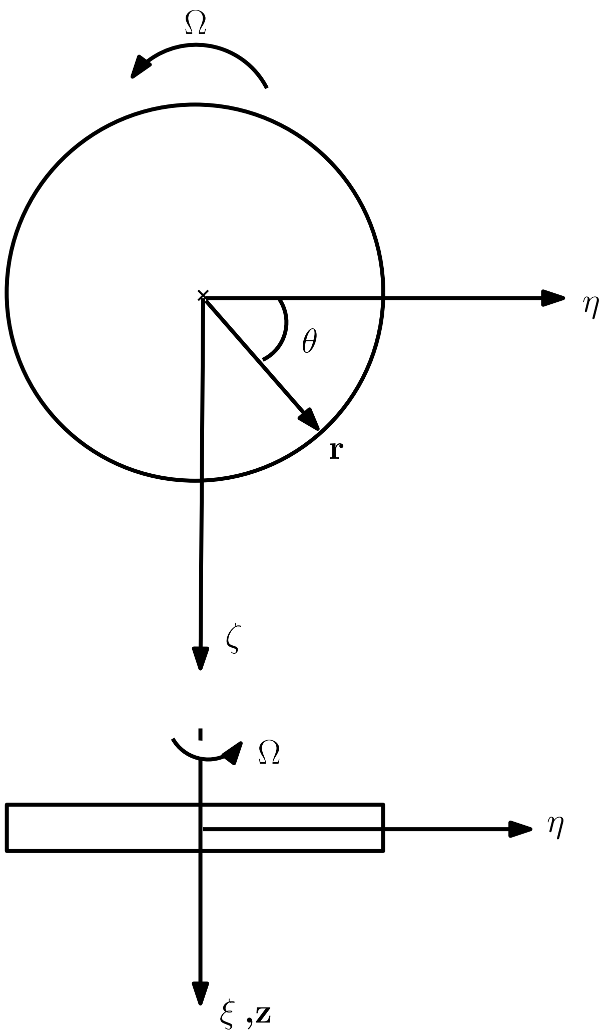

Figure 3.2 Rotor based cylindrical coordinate system

this system and the cylindrical system can be written as:

$$\begin{bmatrix} \hat{e}_n \\ \hat{e}_\theta \\ \hat{e}_s \end{bmatrix} = \begin{bmatrix} \sin\delta & 0 & -\cos\delta \\ 0 & 1 & 0 \\ \cos\delta & 0 & \sin\delta \end{bmatrix} \times \begin{bmatrix} \hat{e}_r \\ \hat{e}_\theta \\ \hat{e}_z \end{bmatrix} = \mathbf{M_3} \times \begin{bmatrix} \hat{e}_r \\ \hat{e}_\theta \\ \hat{e}_z \end{bmatrix} \tag{3.6}$$

If the distribution of deflection along the blade is given, then the following equation of a curved blade can be used:

$$\vec{\mathbf{R}}\left(s\right) = \hat{e}_r \int_0^s \cos\delta\left(s\right)\, ds + \hat{e}_z \int_0^s \sin\delta\left(s\right)\, ds \tag{3.7}$$

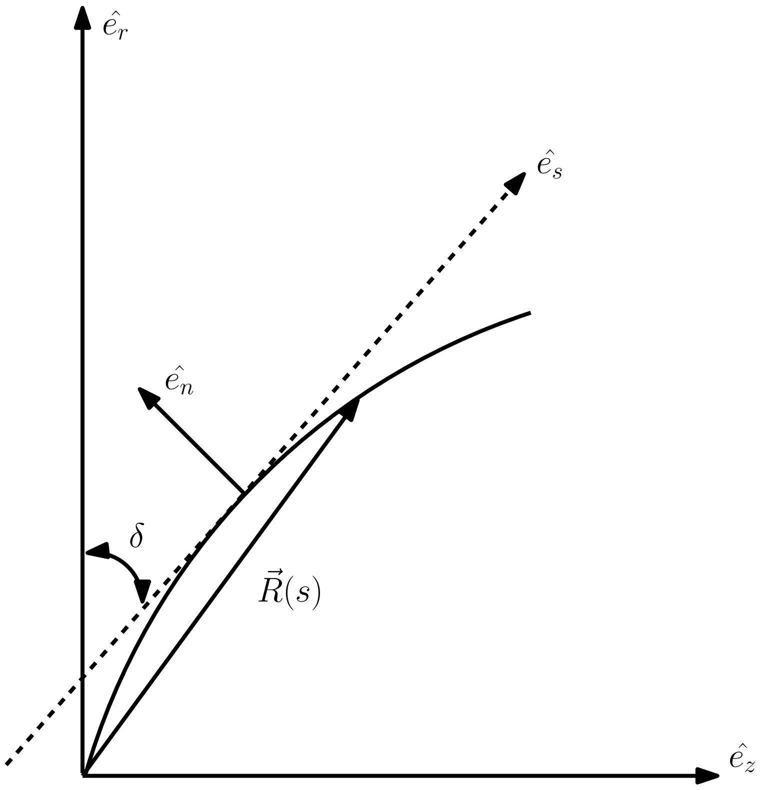

Figure 3.3 Curved blade

### 3.3.2 Rotor Discretization and Intersection

In this section, we shall discuss how the rotor is discretized and subsequently, explain the method of finding the rotor's intersection with the tetrahedral grid elements.

#### 3.3.2.1 Rotor Discretization

The unsteady rotor model considers the rotor to be made up of discrete blades and not as a simplified solid disk. The rotor blades are discretized into elements in the form of circular arcs, centered at the rotor center (See Fig. 3.4).

Blade properties such as blade chord, thickness, twist, out of plane deflection and cross sectional characteristics at the center of the element are assumed to prevail over the entire element. Each of these blade elements acts as a source of momentum, with the source assumed to be concentrated at the center of the element. Thus, each rotor blade behaves as a discrete line of momentum sources. For obtaining a time-accurate solution, it is required to trace

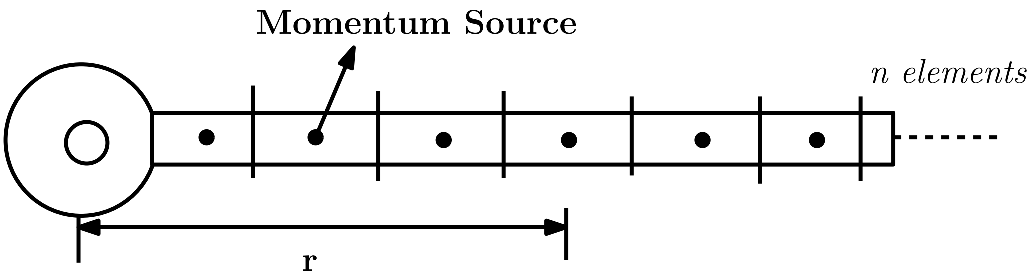

Figure 3.4 Rotor discretization

the time-dependent position of these blades and accordingly find their intersections with the computational grid. The blade position is simply taken to vary linearly with time i.e. the azimuthal position of each rotor blade is given by:

$$\psi = \Omega * time \tag{3.8}$$

#### 3.3.2.2 Rotor Intersections

It is evident that the main feature of the unsteady rotor model is that the instantaneous position of each rotor blade is determined at every instant in time and the rotor intersections are accordingly found. Each of the blade elements travel in an arc about the rotor center. Such an arc described by each blade element is oriented arbitrarily with respect to the three-dimensional computational domain, thereby making the process of finding intersections between the rotor and the computational domain difficult.

In the current research, the computational domain is made up of tetrahedral grid elements. We, therefore, have to find the intersection of an arc with tetrahedrons. The algorithm for finding the rotor intersections defines a natural coordinate system for each tetrahedron. Given a blade location i.e. the $(r, \theta, z)$ coordinates of a blade section, we find which tetrahedron that section lies in by transforming its polar coordinates to the tetrahedral based natural coordinates [**?** ]. We begin by finding the starting cell at a given time step and continue till all the tetrahedrons intersected by a particular blade, in that time step, are found. The angle subtended by a blade section at the rotor center while traversing through a tetrahedral element is computed and stored. This process is repeated for every discretized section of a blade, thereby giving all the possible intersections of the rotor with the computational domain at a given instant in time.

At this point, the difference between the steady and the unsteady rotor model is worth emphasizing again. The main distinction between the steady rotor model and the discrete blade unsteady rotor model is that in the latter, the rotor source terms are added only to those specific control volumes where the rotor blades are actually present, leaving out the rest of the rotor disk plane. For example, for a 2-bladed rotor, if one blade is located at an azimuthal position of $\psi$ at a given instant in time, the other blade would be at $\psi + 180^0$. Then the rotor source would be added to only the control volumes around these two specific regions.

#### 3.3.2.3 Time Step Requirement

After determining the tetrahedral elements where the rotor source has to be added, the question now arises as to how much of the rotor source term should be added to each of these specific cells. It might so happen that at the start of a time step, a blade is present at a position halfway through a tetrahedral element and by the end of that time step, it traverses that element plus half of the next element. A more general scenario would be where a blade line traverses through $x$ number of elements within one time step, some completely while others only partially. It would be erroneous to add the full magnitude of the rotor force to the elements which have only been traversed partially. We, therefore, find the $\Delta\theta$ distance that a blade line travels while passing through a tetrahedral element and average it by the total angular distance $(\Omega * \Delta t)$ that the blade travels in a particular time step. The unsteady source term to be added to a tetrahedral element takes the form:

$$\vec{S} = \frac{\Delta\theta}{\Omega\Delta t}\{-\vec{F}\} \tag{3.9}$$

where, $\Delta\theta$ is the angular distance that the blade traverses in passing through a tetrahedral element. If we take a very large value of the time step such that $\Omega\Delta t = 2\pi$, which means that a blade completes one revolution in one time step, it can be seen that Eq. 3.9 becomes the same as Eq. 3.1, which is used for a steady rotor with one blade $(N_b = 1)$. The unsteady rotor model then collapses into the steady rotor model, for now the rotor source terms are added throughout the disk plane. The steady rotor model can, therefore, be viewed as a limiting case of the unsteady rotor model.

It is evident that the choice of the time step is crucial in this method. A good choice of the time step would be one where a blade takes more than one time step to travel through one grid cell. In other words, the time step should be adequately small so as to ensure that a blade does not jump through more than one grid cell in a time step. The idea here is to make the ratio $(\Delta\theta/\Omega\Delta t)$ tend to one so that there is no averaging involved (See Figs. 3.5 and 3.6). These requirements are met by choosing the time step such that the blade tip travels by a distance equal to $n^{th}$ fraction of the chord length at the tip. For the present computations, $n = 0.5$. Thus,

$$\Delta t = \frac{0.5c_{tip}}{\Omega R} \tag{3.10}$$

Even for a tapered blade, since the chord length at the tip is the minimum, we can see that Eq. 3.10 furnishes a minimum usable $\Delta t$.

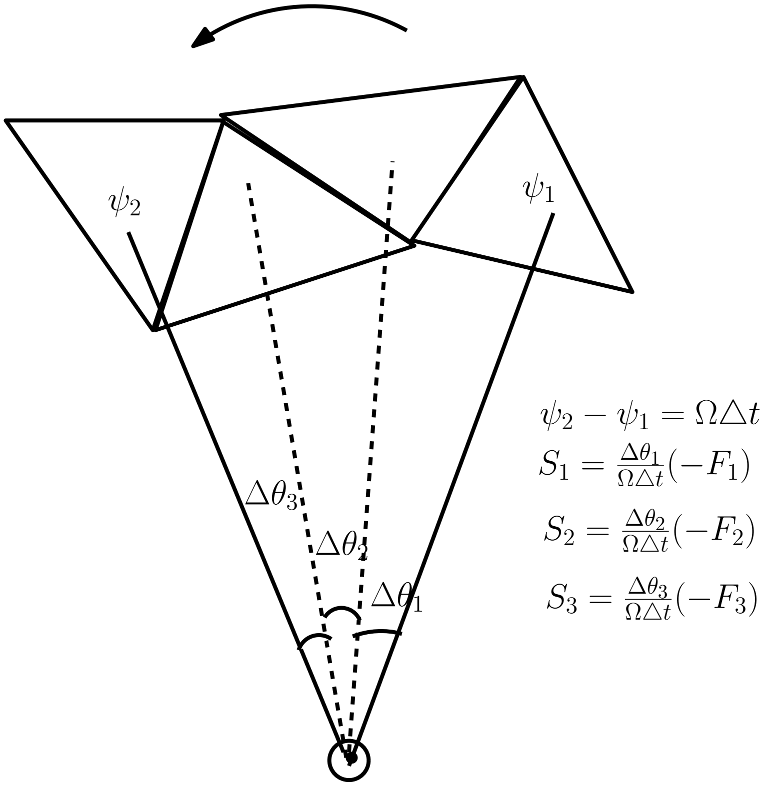

Figure 3.5 Blade traversing through multiple grid cells in one time step

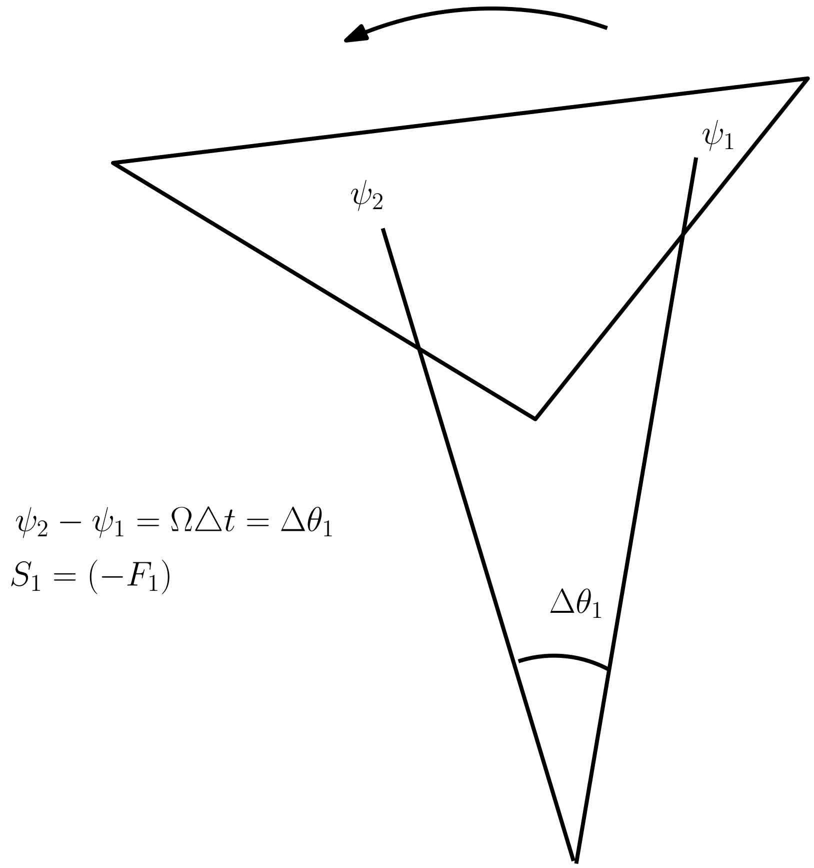

Figure 3.6 Blade remains in one grid cell for more than one time step

## 3.4 Calculation of Rotor Forces

The task now is to find the magnitude of the rotor force $\vec{F}$. Let the fluid velocity at any point '$s$' on a blade at an angular position $\theta$ be:

$$\vec{V} = u\hat{i} + v\hat{j} + w\hat{k} \tag{3.11}$$

Using Eqs. 3.3, 3.5 and 3.6, the same velocity can be written in the $(n, \theta, s)$ system as:

$$\vec{V} = v_s\hat{e}_s + v_\theta\hat{e}_\theta + v_n\hat{e}_n \tag{3.12}$$

where,

$$\begin{bmatrix} v_n \\ v_\theta \\ v_s \end{bmatrix} = \mathbf{M_3 M_2 M_1} \begin{bmatrix} u \\ v \\ w \end{bmatrix}. \tag{3.13}$$

The blade also has a velocity due to its rotation which can be written in the $(n, \theta, s)$ system as:

$$\vec{V}_{bl} = \mathbf{M_3 M_2 M_1} \left( \vec{\Omega} \times \bar{\mathbf{R}}(s) \right) \tag{3.14}$$

where, $\vec{\Omega}$ is as defined in Eq. 3.2 and $\vec{\mathbf{R}}(s)$ is the position vector of the point on the blade under consideration. Thus, the relative velocity $\vec{V}_{rel} = v'_s \hat{e}_s + v'_\theta \hat{e}_\theta + v'_n \hat{e}_n$, seen by the blade is:

$$\begin{aligned} \vec{V}_{rel} &= \vec{V} - \vec{V}_{bl} \\ &= \mathbf{M_3 M_2 M_1} \vec{V} \\ &- \mathbf{M_3 M_2 M_1} \left( \vec{\Omega} \times \vec{\mathbf{R}}(s) \right) \end{aligned} \tag{3.15}$$

The aerodynamic force acting in the spanwise direction is zero and therefore, only the velocity component in the plane normal to $\hat{e}_s$ is required for evaluating the aerodynamic forces. The angle made by this component with the $\hat{e}_\theta$ direction is given by (see Fig. 3.7)

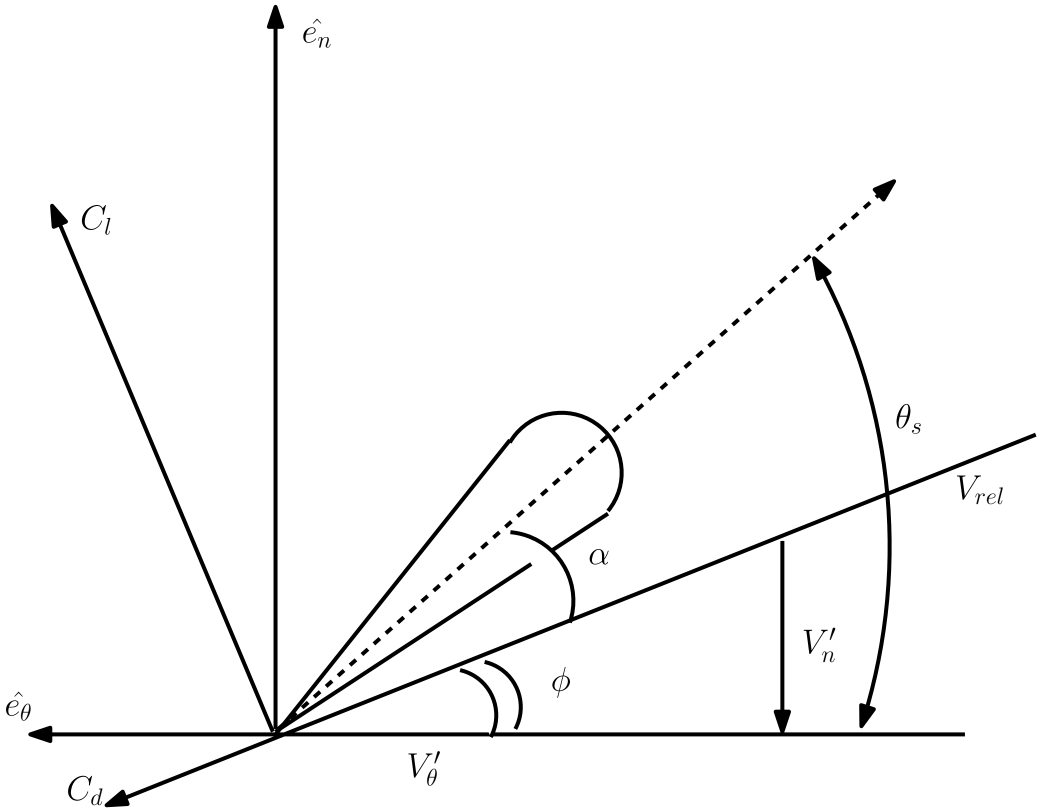

Figure 3.7 Airfoil cross-section

$$\phi = \arctan(-v'_n/v'_\theta) \tag{3.16}$$

If the section has a twist of angle $\theta_s$ with respect to the plane of rotation then, from Fig. 3.7, the effective angle of attack seen by the airfoil is:

$$\alpha = \theta_s - \phi \tag{3.17}$$

Once the effective angle of attack $\alpha$ and the components of the relative velocity seen by the airfoil are known, we can find the sectional aerodynamic coefficients $C_l$ and $C_d$ using the airfoil characteristics. The lift and drag forces can now be found from the aerodynamic coefficients.

$$\mathrm{L}' = \frac{1}{2}\rho {v'}^2 C_l c\ ds \tag{3.18}$$

$$\mathrm{D}' = \frac{1}{2}\rho {v'}^2 C_d c\ ds \tag{3.19}$$

where, c is the blade chord-length and ${v'}^2 = {v'_n}^2 + {v'_\theta}^2$. The lift and drag forces act perpendicular and parallel, respectively, to the relative velocity vector. Resolving these forces gives the forces in $\hat{e}_n$ and $\hat{e}_\theta$ directions.

$$f_n = \mathrm{L}' \cos\phi - \mathrm{D}' \sin\phi \tag{3.20}$$

$$f_\theta = \mathrm{L}' \sin\phi + \mathrm{D}' \cos\phi \tag{3.21}$$

Also, $f_s = 0$.

The aerodynamic forces $(f_n, f_\theta, f_s) = \vec{f}$ on the blade element can now be transformed back to the computational coordinate system $(x, y, z)$ using the inverse transformation relations.

$$\vec{F} = \mathbf{M_1}^{\mathrm{T}} \mathbf{M_2}^{\mathrm{T}} \mathbf{M_3}^{\mathrm{T}} \vec{f}. \tag{3.22}$$

$\vec{F}$ is the resultant force acting on a blade element at $(s, \theta)$, then $-\vec{F}$ is the instantaneous force acting on the fluid element at that location. The rotor force thus obtained is used in Eq. 3.9 to determine the instantaneous momentum source due to the rotor.

## 3.5 Rotor Source Terms in the Momentum Equations

The rotor sources found in the previous section are added to the tetrahedral elements that are intersected by the rotor blades. Since the discretized momentum equations are written in terms of the node points, and not the tetrahedral elements, we need to decide how this rotor source contribution will be accounted for the nodes of an intersected tetrahedron. The source term gets divided equally between the four nodes of a tetrahedron i.e. one-fourth of the momentum source, which is constant over a tetrahedral element, gets added to the discretized momentum equations of the four nodes which make up that tetrahedron. It must be noted here that a tetrahedron can be intersected by more than one blade section, in which case there will be more than one rotor source contribution to the discretized momentum equations for the node points of the concerned tetrahedron. It is good practice to discretize a rotor blade such that there are about 100 momentum sources along a blade radius.

In the next chapter, the validation results for the unstructured median-dual based flow solver are discussed. This will be followed by the validation results for the unsteady rotor model, obtained by testing the unsteady rotor model with an already available 3D structured code. It must be noted here that since both the structured and unstructured flow solvers use finite volume based SIMPLER algorithm, the coupling process of both the rotor models is quite similar. The difference is in the procedure of finding the rotor intersections as the type of grid cells varies between the structured (Cartesian hexahedral elements) and the unstructured (tetrahedral elements) flow solvers. The following flowchart summarizes the discrete blade unsteady rotor model and its coupling with an unsteady flow solver, be it structured or unstructured.

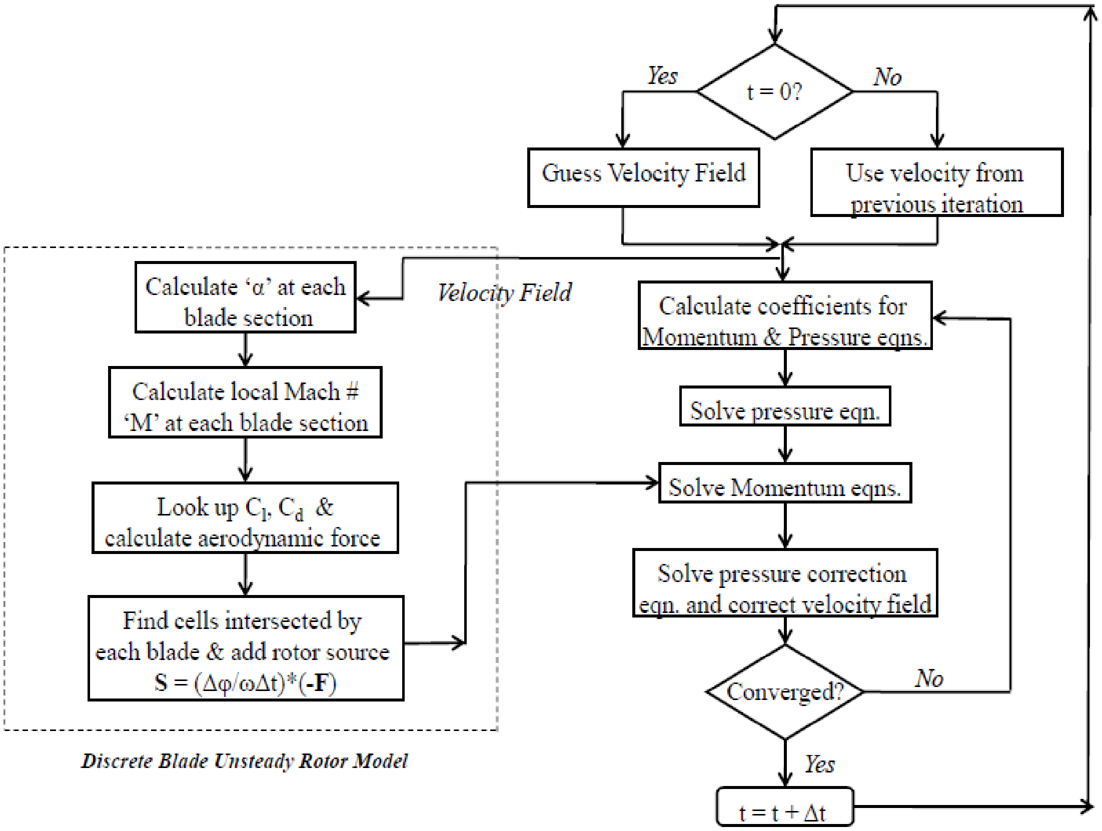

Figure 3.8 Flow chart

# CHAPTER 4. RESULTS AND DISCUSSION

## 4.1 3-D Unstructured Code Validation

The control volume based 3D unstructured flow solver was validated using benchmark problems in literature. The following sections describe each problem and the results obtained.

### 4.1.1 Lid Driven Cavity

The standard test case of the flow field within a three-dimensional, lid driven cavity is used to validate the solver. The schematic of the problem is shown in Fig. 4.1. The cavity is a unit cube with $L = 1\ m$ and the maximum $z$ plane is treated as the lid, moving with a constant velocity of $1\ m/s$. No-slip boundary condition is applied on all the other boundaries. The movement of the lid drives the flow inside due to the transport of shear stress by molecular viscosity. The Reynolds number for the flow is defined as:

$$Re = \frac{\rho U_{lid} L}{\mu} \tag{4.1}$$

where, $\rho$ is the fluid density, $\mu$ is the fluid viscosity and $U_{lid}$ is the lid velocity. Reynolds number of 100 and 1000 were simulated and compared with the benchmark solution of Yang et. al. [47]. The computational grids were generated by tessellating a 3-D structured grid into tetrahedrons using Tetgen. For the driven cavity problem, two computational grids were used. The coarser grid was generated by tessellating a 11 x 11 x 11 structured grid, resulting in 1331 nodes. The second grid has 21 x 21 x 21 i.e. 9261 grid points (See Fig. 4.2). Fully implicit time integration was used for all simulations with a time step of 0.01.

For the Reynolds number of 100, the velocity profiles of $u$ on the vertical centerline and $w$ on the horizontal centerline were obtained for grids 11 x 11 x 11 and 21 x 21 x 21 and compared

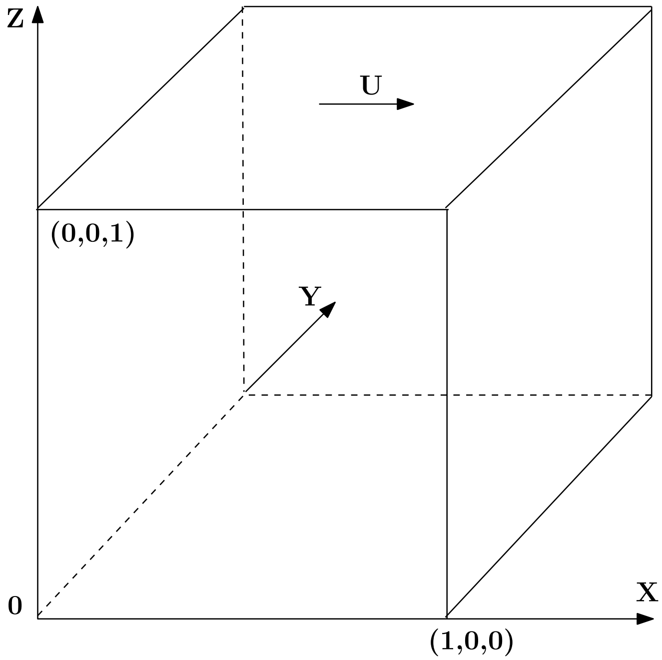

Figure 4.1 Driven cavity : Schematic

with computational results of Yang et. al. From Figs. 4.3(a) and 4.3(b), it can be seen that the finer grid matches better with the benchmark solution and the overall agreement is good. In Figs. 4.4-4.6, the instantaneous velocity vector plots on the three midplanes $z = 0.5$, $y = 0.5$ and $x = 0.5$ are depicted. The $z - y$ plane shows the presence of two counter-rotating vortices that move towards the corners of the cavity. The $x - z$ plane shows a primary vortex that is centered slightly above the center of the cavity. Because of inadequate grid resolution near the wall, no secondary vortices at the bottom corners of the domain are captured.

For $Re = 1000$ case, Fig. 4.7(a)-4.7(b) show the centerline 'u' and 'w' velocities, respectively, for the 21 x 21 x 21 grid case. A good agreement with the benchmark results of Yang et.al. is observed for the Reynolds number of 1000 also. Fig. 4.8-4.9 depict the velocity vector plots for the $Re = 1000$ case. Due to the higher Reynolds number, two vertical vortices appear in the $x - y$ plane, as compared to the nearly uniform backward flow for $Re = 100$. The primary vortex in $x - z$ plane is also seen to penetrate deeper into the cavity as compared to the lower Reynolds number of 100.

In order to capture the vortices better, a stretched grid with finer resolution near the wall was used for the $Re = 1000$ case. The grid is shown in Fig. 4.10 and Fig. 4.11-4.12 show the vector plots for the $Re = 1000$ with the finer grid. It can be seen that the vertical vortices in the $x - y$ plane are more discernible. Counter rotating vortices are observed in the $z - y$ plane, which could not be captured properly with the coarser grid. Fig. 4.13(a)-4.13(b) shows the iso-surfaces of absolute velocity $|\vec{v}| = 0.13$ for the $Re = 100$ and $Re = 1000$ cases for the 21 x 21 x 21 grid. The high speed core of the fluid is seen to become narrower with the increase in Reynolds number, penetrating deeper into the cavity. Fig. 4.14 shows the time decay of mass residual for the two Reynolds numbers and it can be seen that the solution has converged satisfactorily.

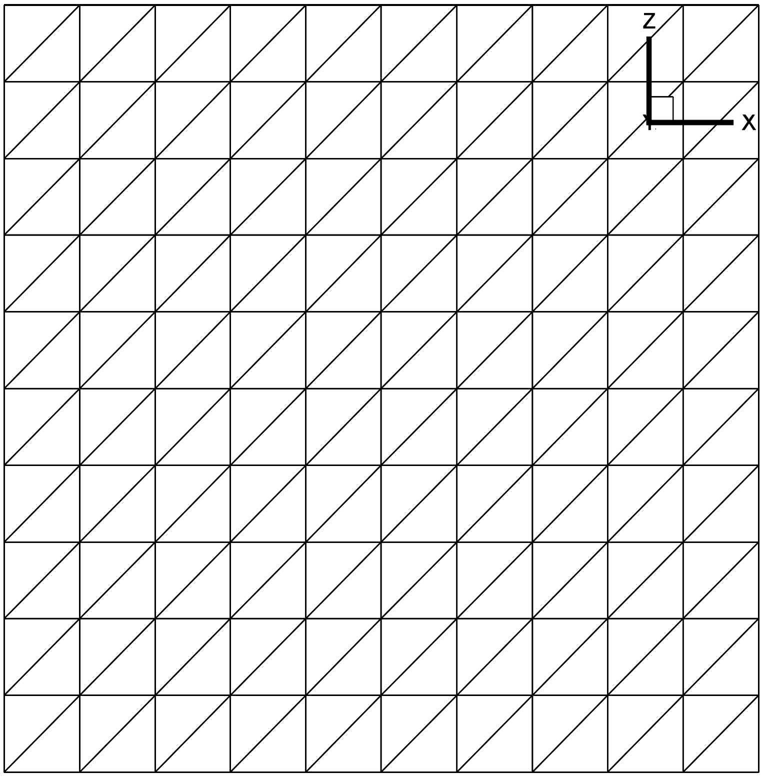

(a) 11 x 11 x 11 grid, Number of nodes = 1331

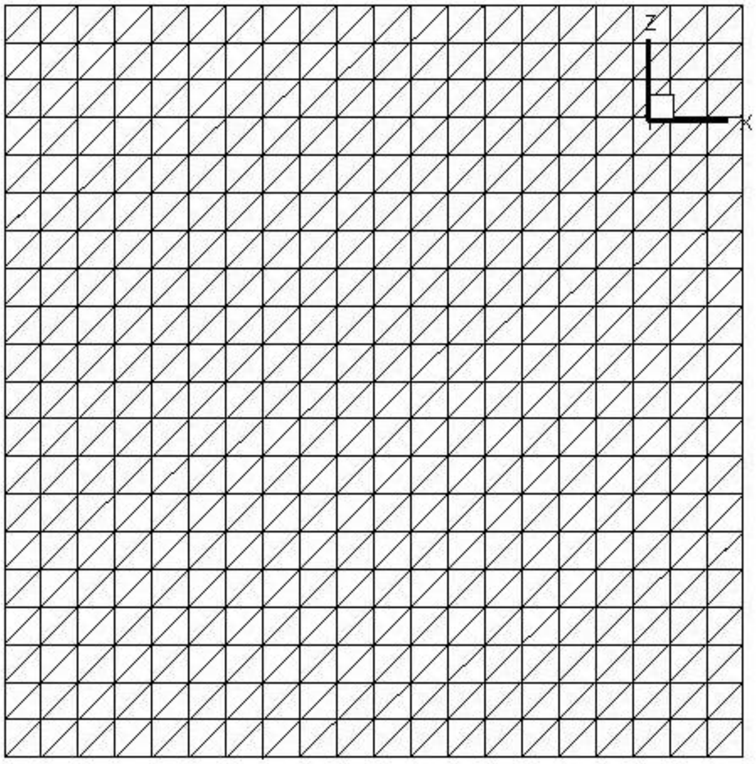

(b) 21 x 21 x 21 grid, Number of nodes = 9261

Figure 4.2 Computational Grids

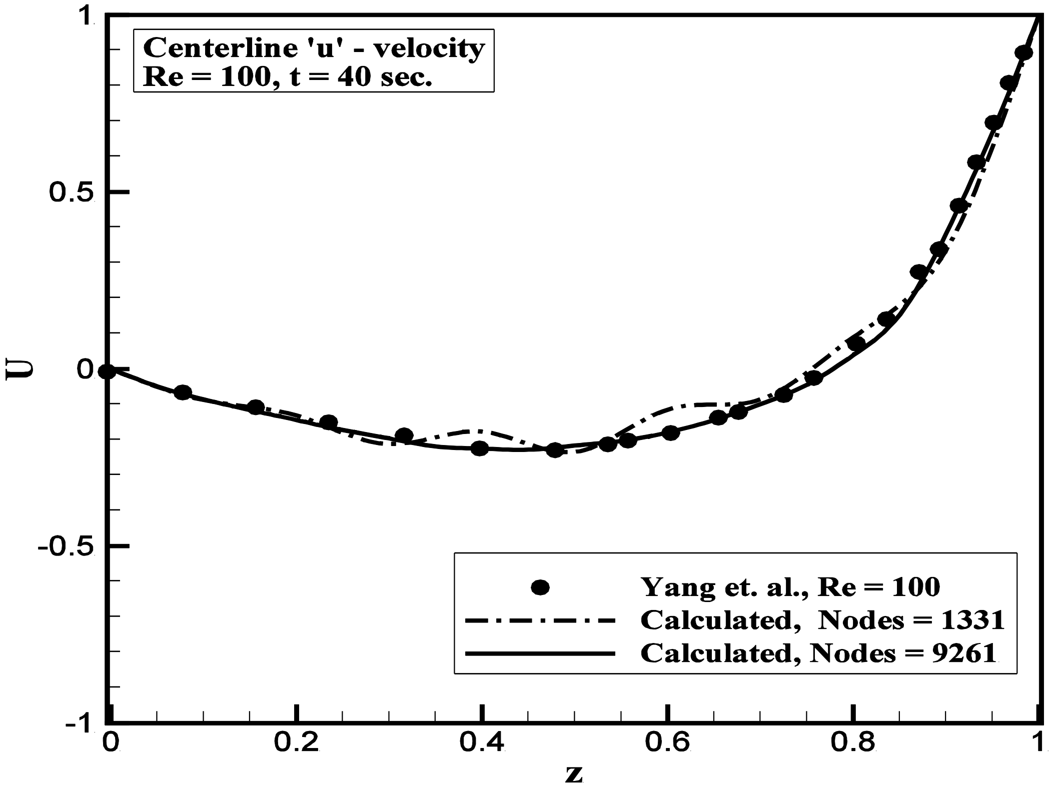

(a) U-velocity on vertical centerline

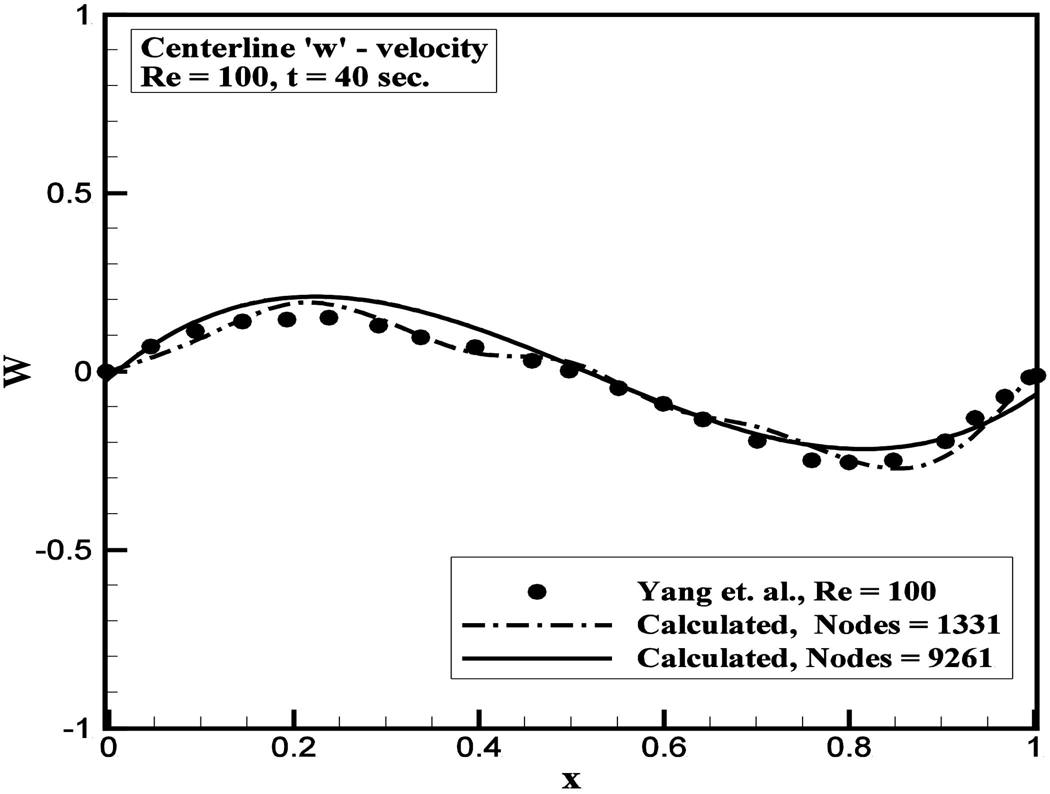

(b) W-velocity on horizontal centerline

Figure 4.3 Centerline velocity profiles, $Re = 100$

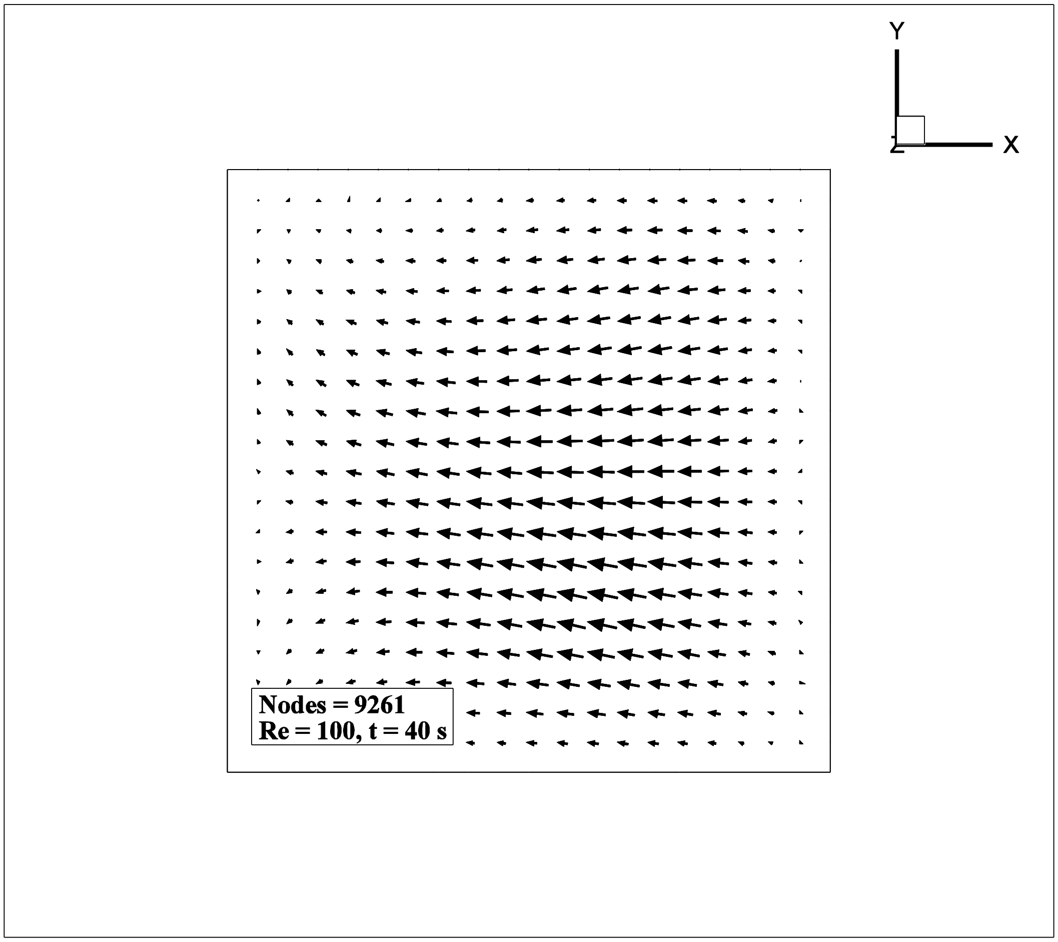

Figure 4.4 Velocity vectors $z = 0.5$, $Re = 100$

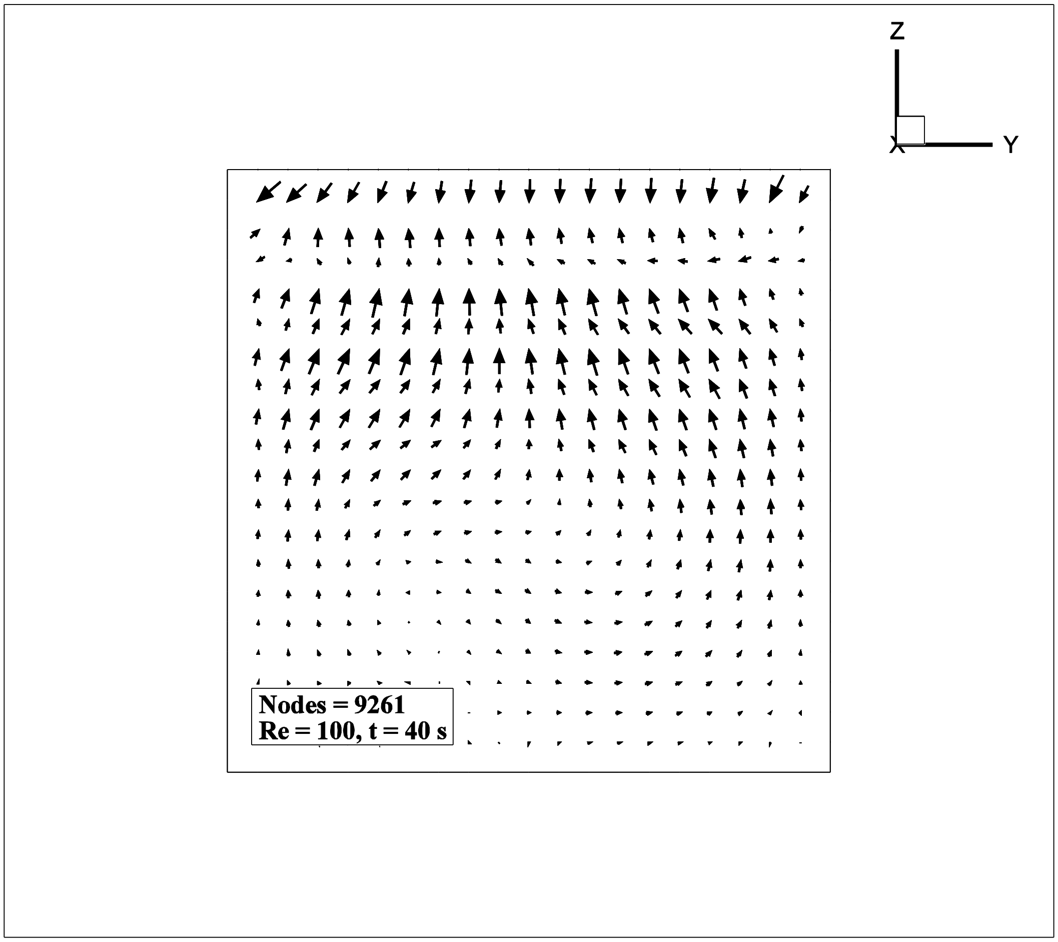

Figure 4.5 Velocity vectors $x = 0.5$, $Re = 100$

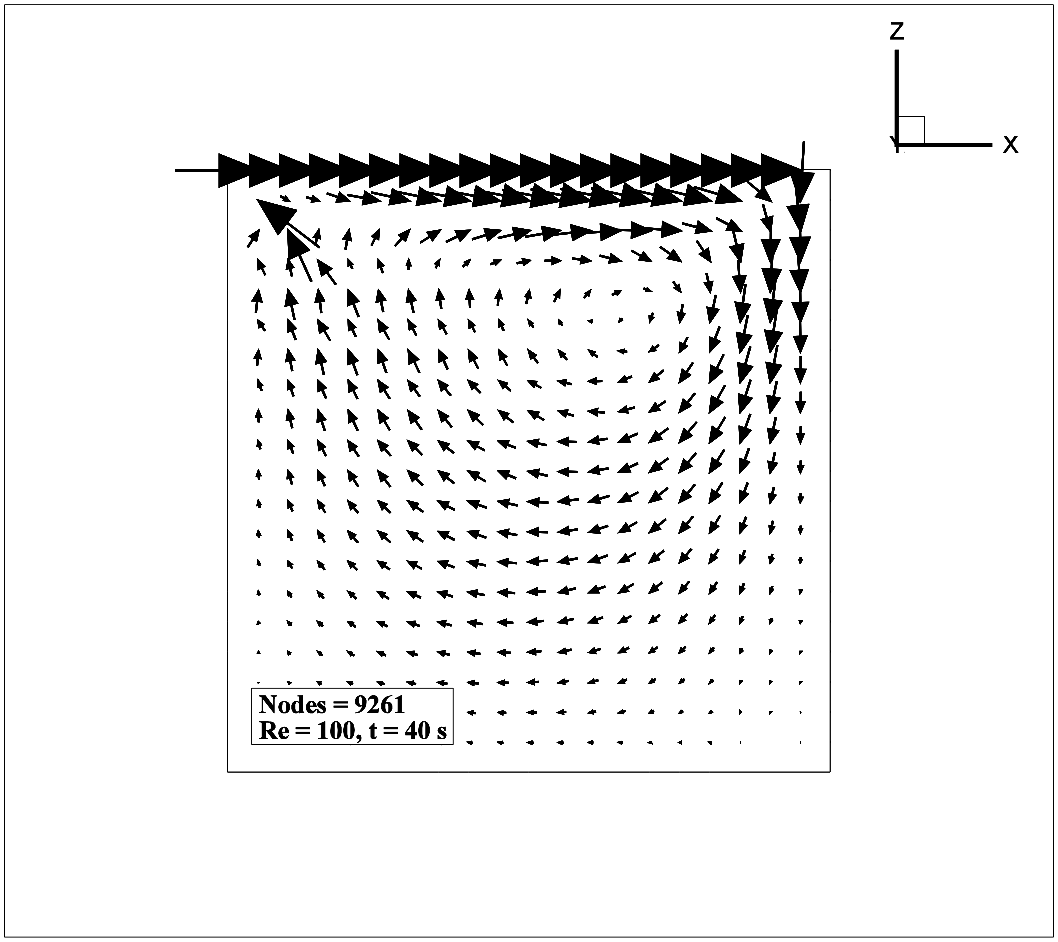

Figure 4.6 Velocity vectors $y = 0.5$, $Re = 100$

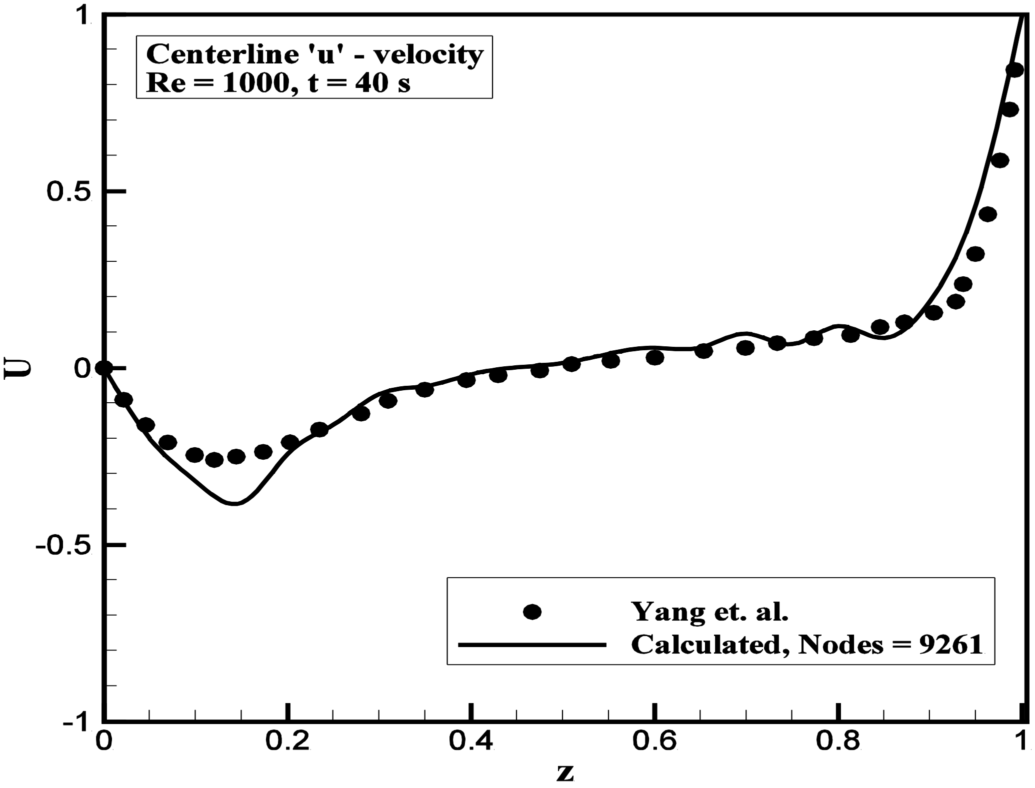

(a) U-velocity on vertical centerline

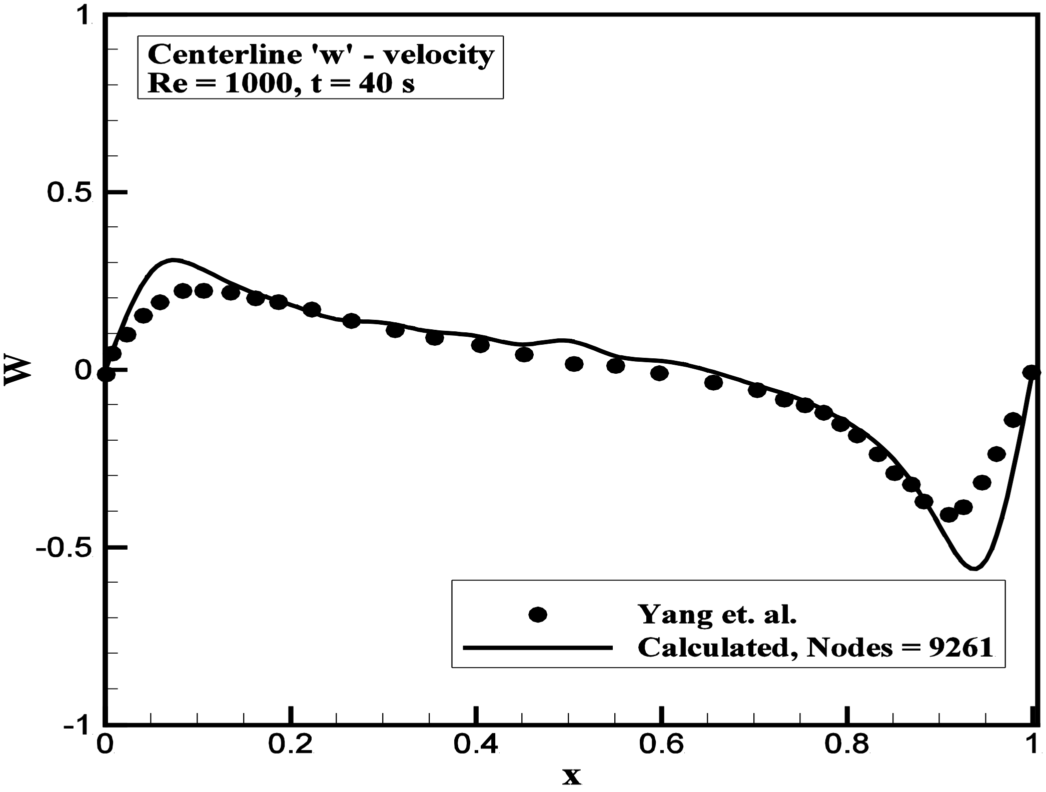

(b) W-velocity on horizontal centerline

Figure 4.7 Centerline velocity profiles, $Re = 1000$

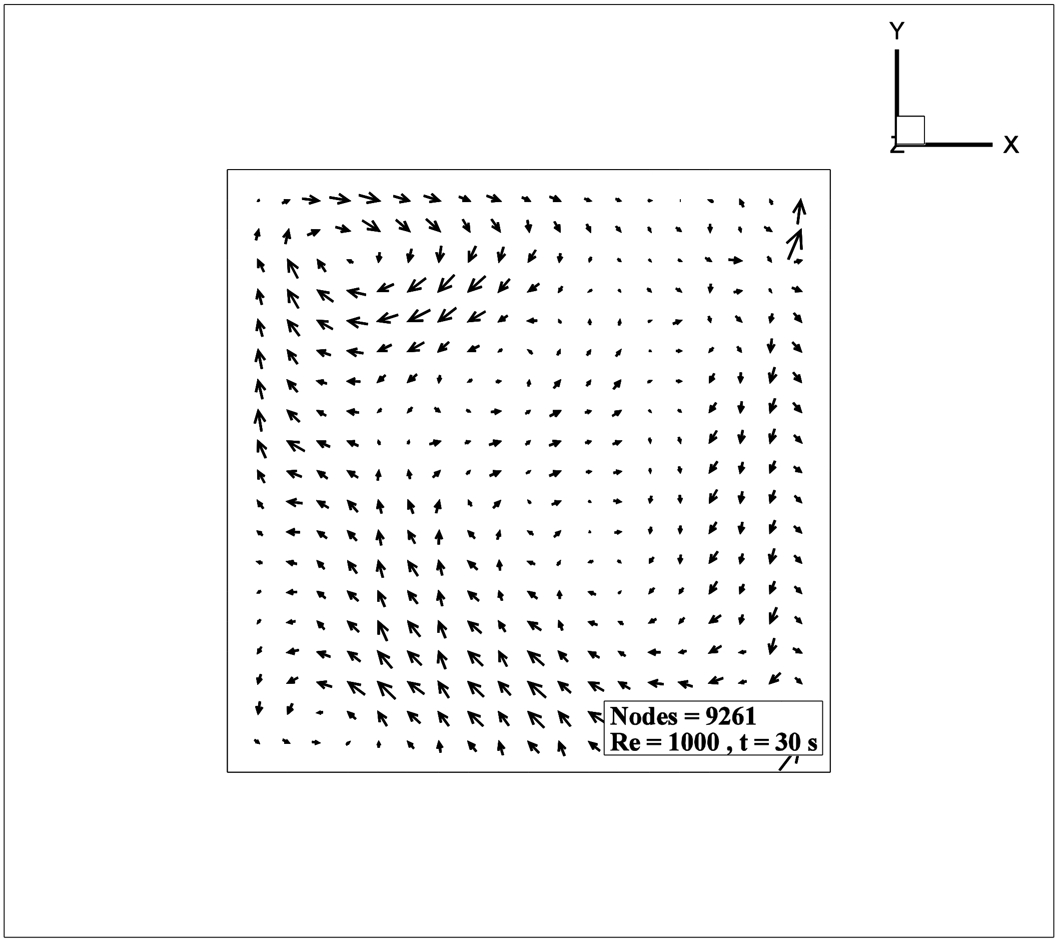

Figure 4.8  Velocity vectors $z = 0.5$, $Re = 1000$

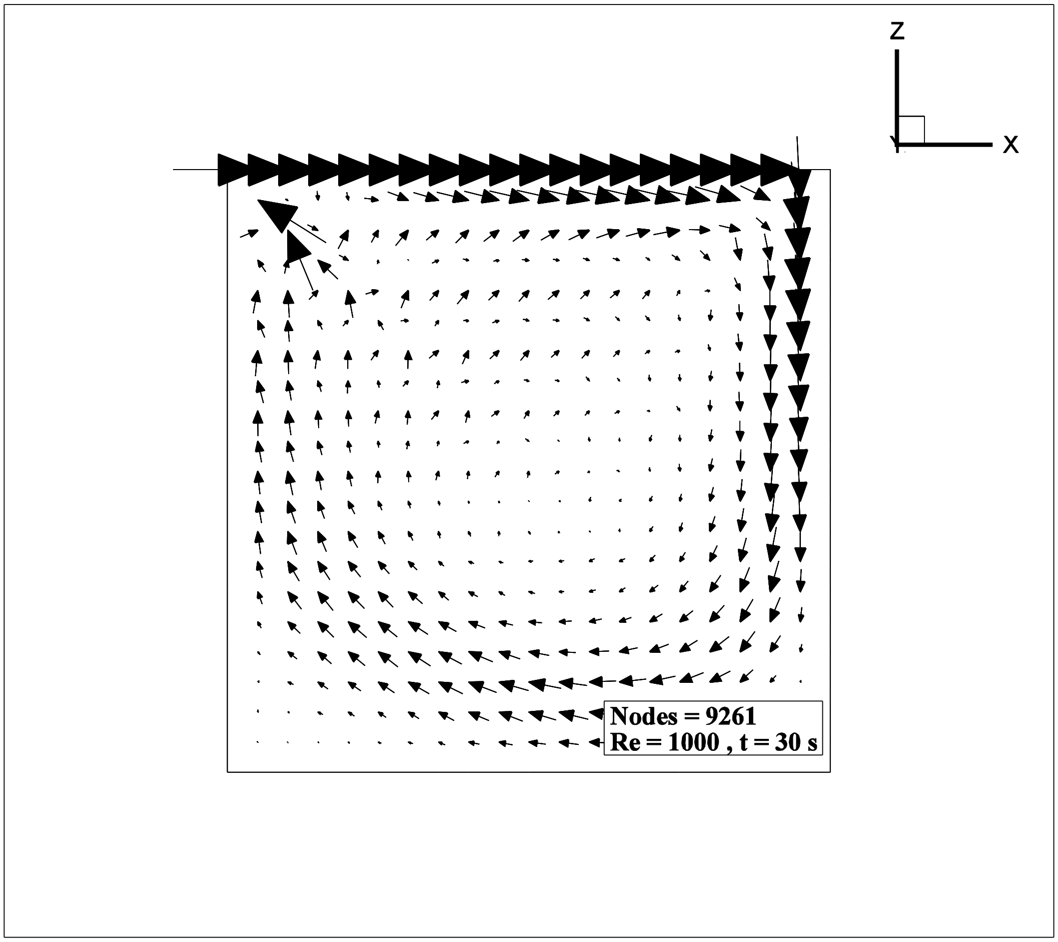

Figure 4.9 Velocity vectors $y = 0.5$, $Re = 1000$

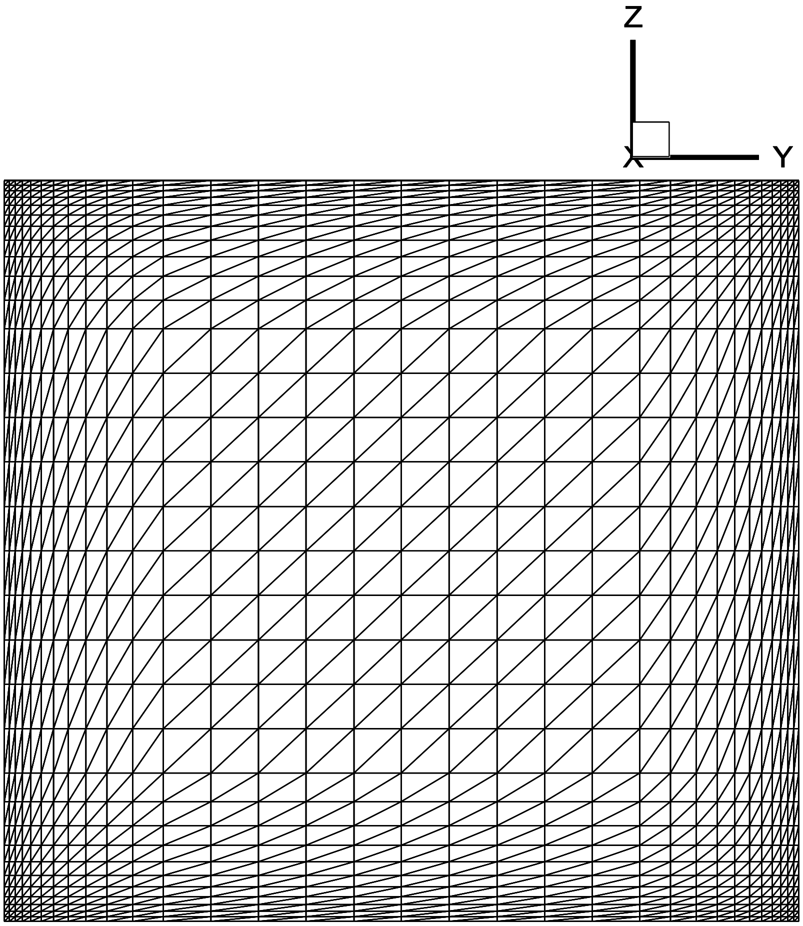

Figure 4.10 Stretched grid

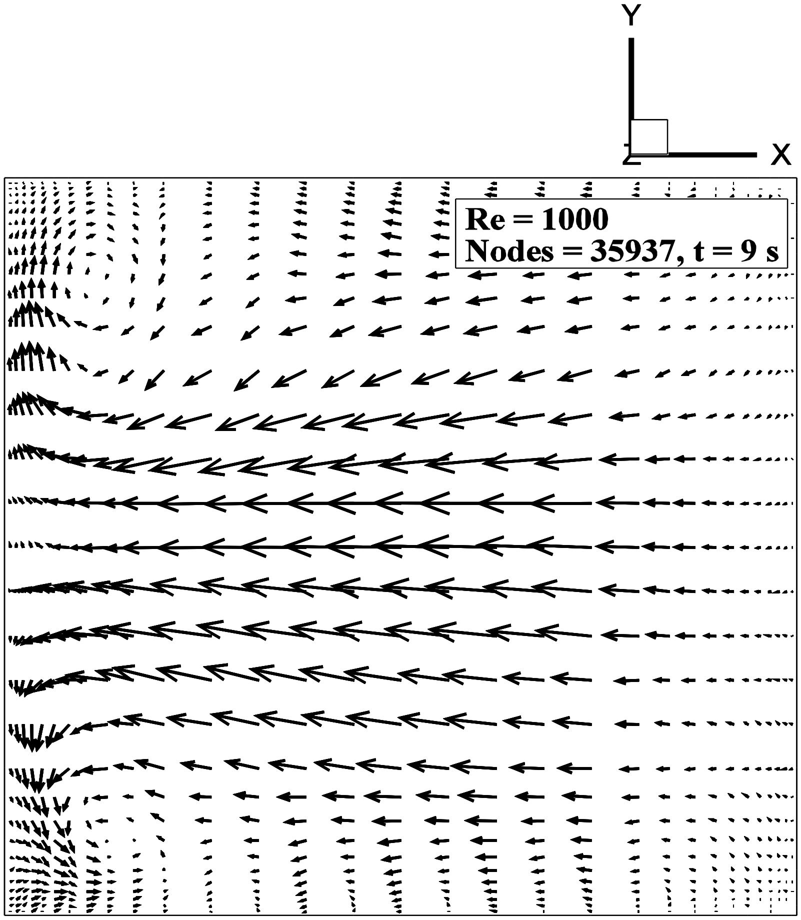

Figure 4.11 Velocity vectors $z = 0.5$, Stretched grid, $Re = 1000$

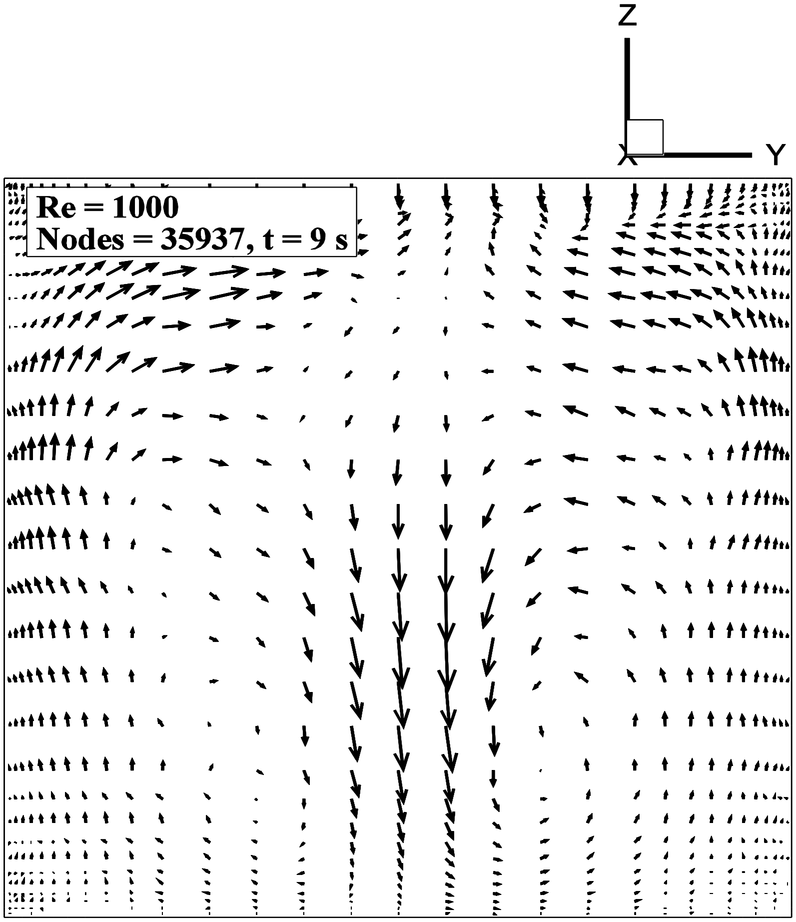

Figure 4.12 Velocity vectors $x = 0.5$, Stretched grid, $Re = 1000$

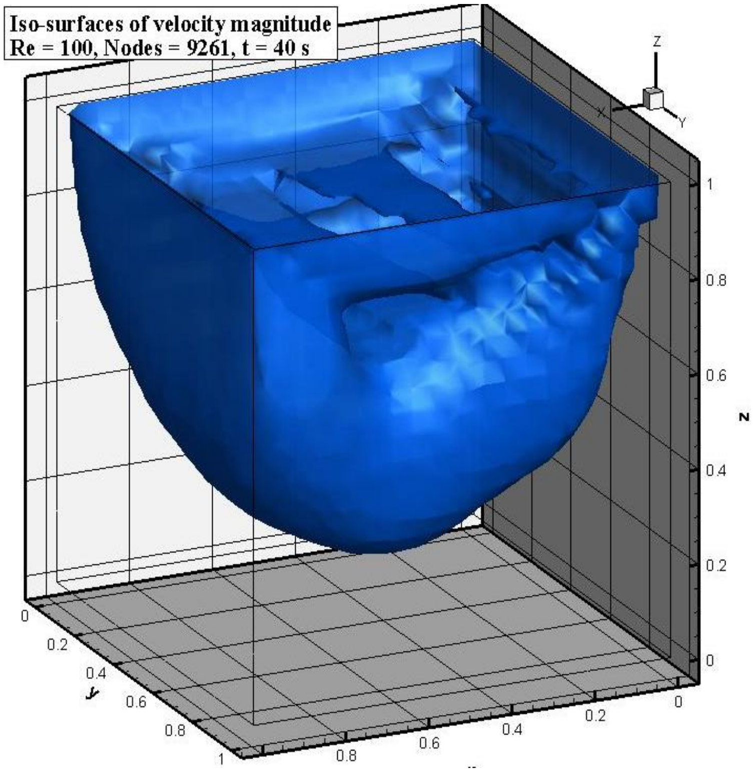

(a) $Re = 100$

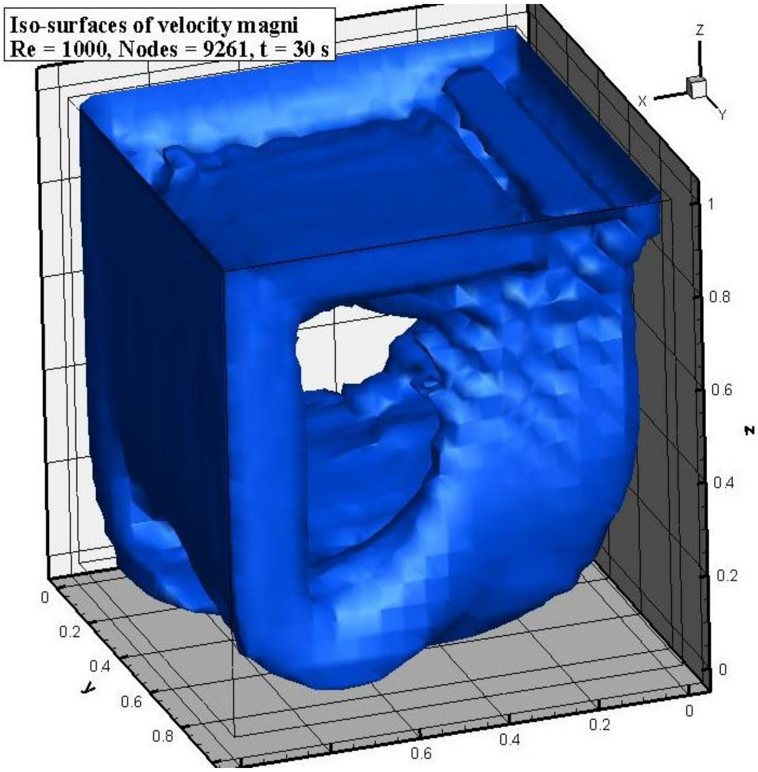

(b) $Re = 1000$

Figure 4.13 Iso-surfaces of velocity magnitude, $|\vec{v}| = 0.13$

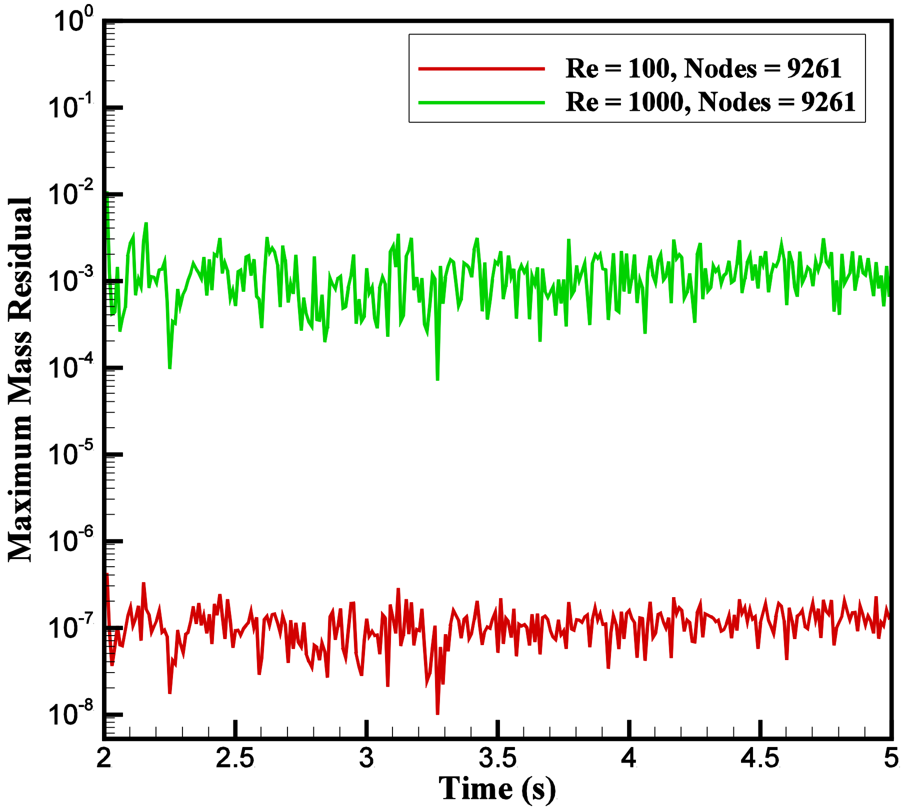

Figure 4.14 Lid driven cavity: Mass residuals

### 4.1.2 Oscillating Lid Driven Cavity

The three-dimensional flow driven by a sinusoidal oscillation of the top lid of a unit cavity was simulated. The inherent three-dimensionality and unsteadiness of the problem make it a challenging test case for validation. The schematic for this problem is similar to that shown in Fig. 4.1, except that the $z - max$ plane is now moving with an oscillating velocity given by:

$$U = U_o \cos \omega_1 t \tag{4.2}$$

where, $U_o = 1\ m/s$, $\omega_1 = \omega' U_o / L$ and $L = 1\ m$. The Reynolds number for such a flow is given by $Re = U_o L / \nu$. A Reynolds number of 100 with two different values of $\omega'$ were simulated to study the salient three-dimensional features of the confined cavity flow. The results obtained are compared with similar numerical computations conducted by Iwatsu. et. al. [48], where a third order finite difference method was used to simulate the problem on a non-uniform, non-staggered mesh. The computational grid used has 9261 node points, similar to the grid shown in Fig. 4.2(b). Fully implicit time scheme was used for time integration, with $\Delta t$ chosen according to the oscillation frequency.

For the Re = 100 case, two oscillation frequencies of $\omega' = 0.4$ and $\omega' = 10.0$ are studied. In Fig. 4.15, the character of the main flow on the symmetry plane $z = 0.5$ for $Re = 100, \omega' = 0.4$ is visualized through the $u - v$ component of velocity field. Starting at an initial instant $t = 8T + 3/4T$, where $T = 2\pi/\omega'$, first half cycle of oscillation is shown. The same plots for $Re = 100, \omega' = 10.0$ are depicted in Fig. 4.16. The effect of the oscillation frequency is manifested in the penetration depth, defined as the vertical distance from the top wall over which the motion of the top wall has direct influence. For the low $\omega'$ case in Fig. 4.15, the effect of the motion of the top wall penetrates deeper into the cavity as compared to the higher value of $\omega'$, where the fluid motion is confined to the narrow region close to the moving boundary. This observation is consistent with the findings of Iwatsu et. al. [48] for three-dimensional confined flows.

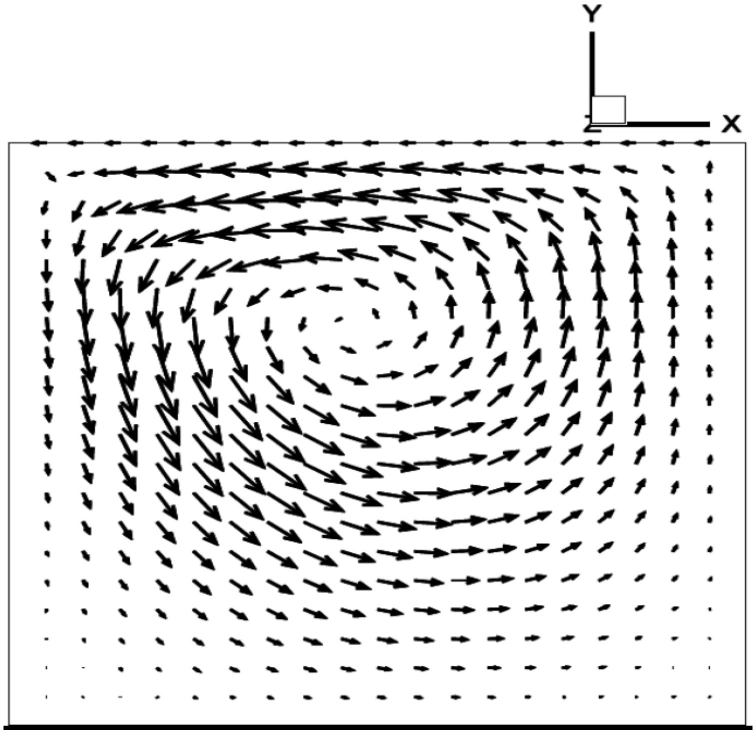

(a) t = 0

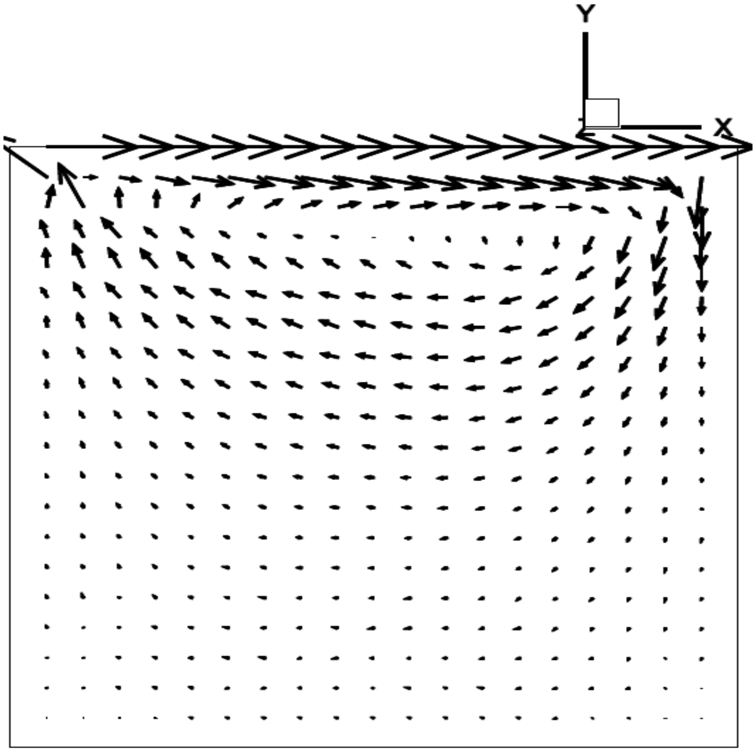

(b) t = T/8

Figure 4.15 $u - v$ velocity component in $z = 0.5$ plane, Re $= 100$, $\omega' = 0.4$
Starting instant t = 8T + 3/4T, $T = 2\pi/\omega'$

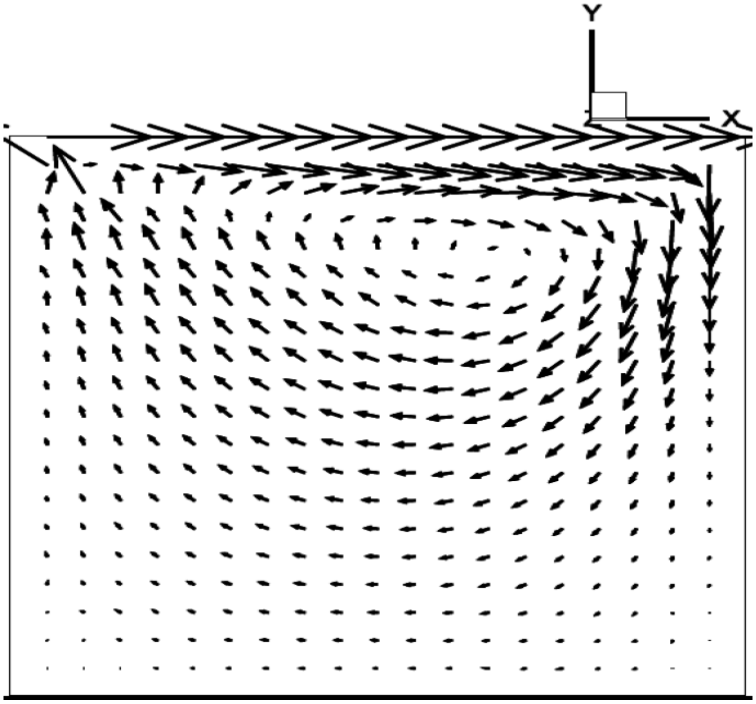

(c) t = T/4

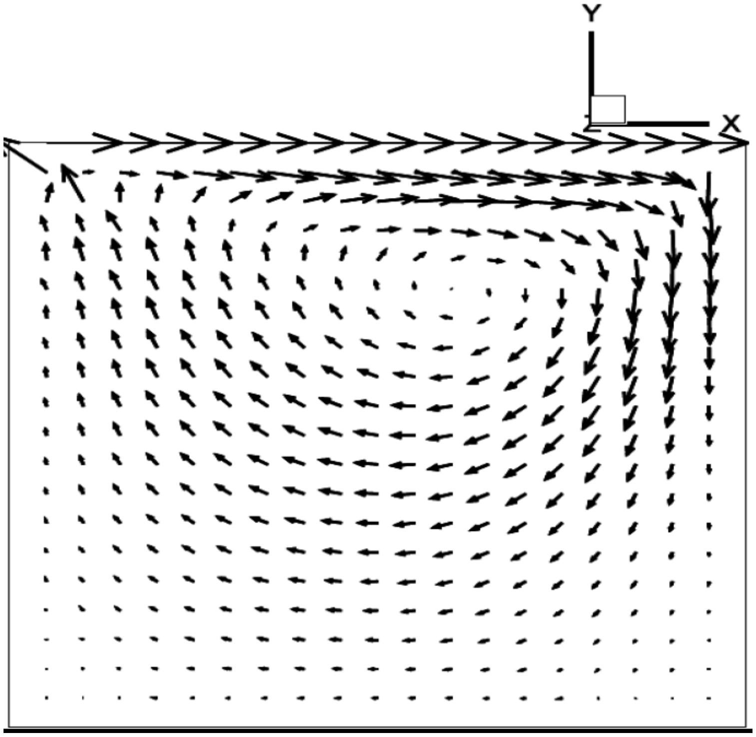

(d) t = 3/8T

Figure 4.15 (continued) $u - v$ velocity component in $z = 0.5$ plane, Re = 100, $\omega' = 0.4$, Starting instant t = 8T + 3/4T, $T = 2\pi/\omega'$

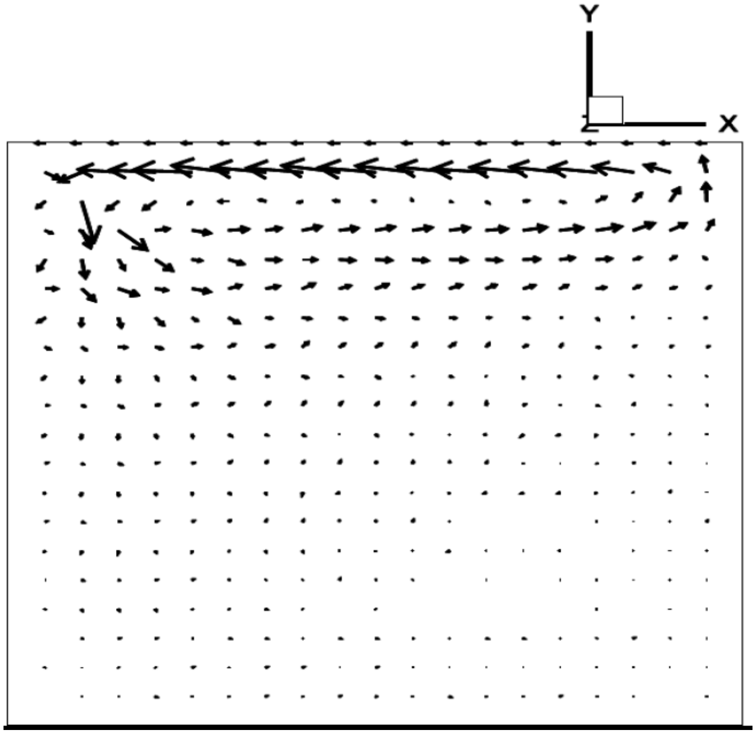

(a) t = 0

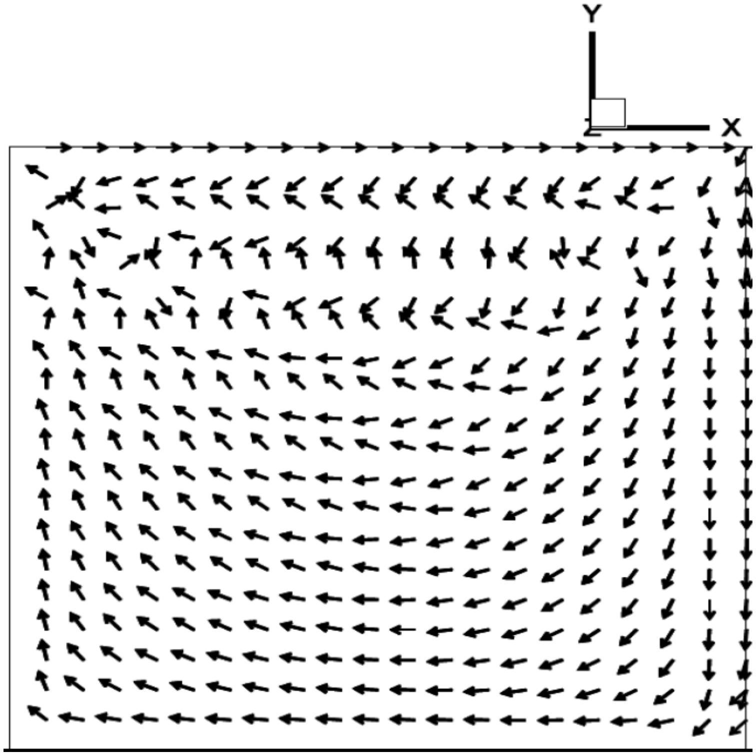

(b) t = T/8

Figure 4.16 $u - v$ velocity component in $z = 0.5$ plane, Re = 100, $\omega' = 10.0$
Starting instant t = 8T + 3/4T, $T = 2\pi/\omega'$

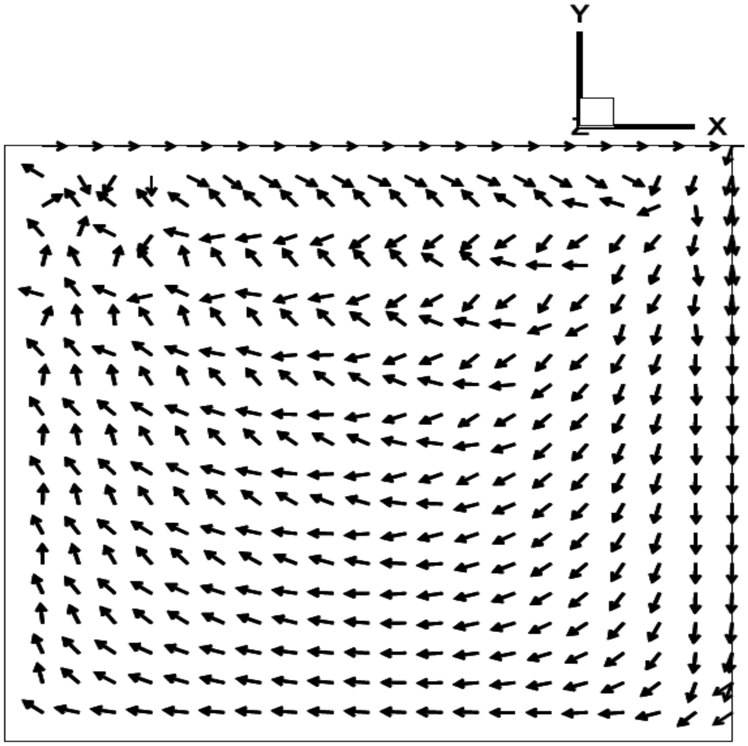

(c) t = T/4

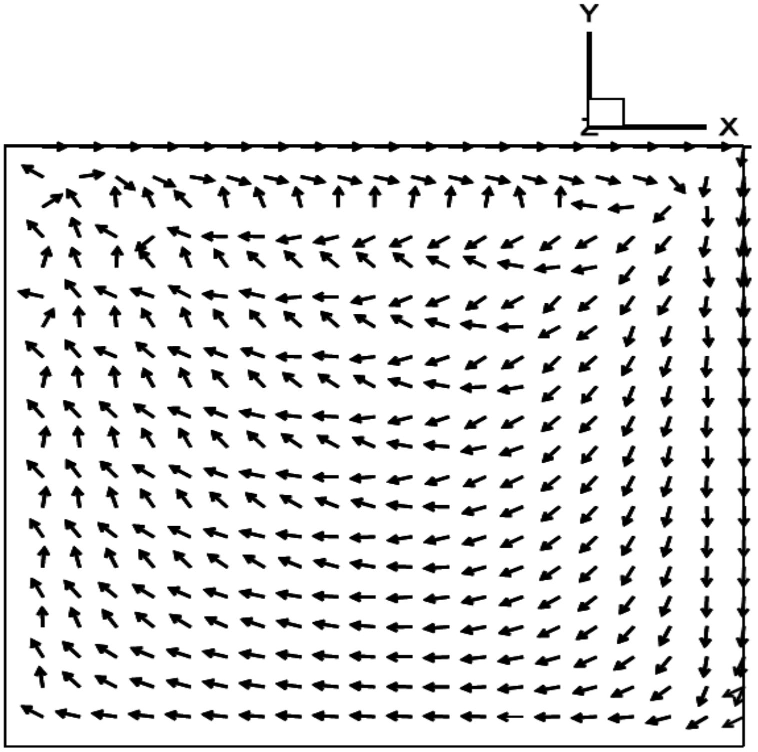

(d) t = 3/8T

Figure 4.16 (continued) $u - v$ velocity component in $z = 0.5$ plane, Re = 100, $\omega' = 10.0$, Starting instant t = 8T + 3/4T, $T = 2\pi/\omega'$

Next, the secondary flow behavior of the oscillating lid driven cavity is studied by comparing the $v-w$ velocity components on the symmetry plane $x = 0.5$ for $\omega' = 0.4$ and $\omega' = 10.0$. These are shown in Fig. 4.17 and Fig 4.18, respectively. When $\omega'$ is low, as in Fig. 4.17, the presence of the secondary flow is discernible, establishing the three-dimensionality of the overall flow pattern. Whereas for the higher value of $\omega'$, the main flow itself is weak in the vast majority of the cavity volume and the secondary flow patters are vanishingly small.

The transverse (z) variations of the principal velocity $u$ for the two values of $\omega'$ are presented in Fig. 4.19-4.20. The starting instant for recorded data is $17T + 3/4T$, where $T = 2\pi/\omega'$. The three-dimensionality of the flow becomes apparent near the end walls, especially for the lower $\omega'$, while much of the cavity interior sees fairly uniform u-velocity. The results obtained using the current unstructured solver agree reasonably well with the numerical results of Iwatsu et. al. [48].

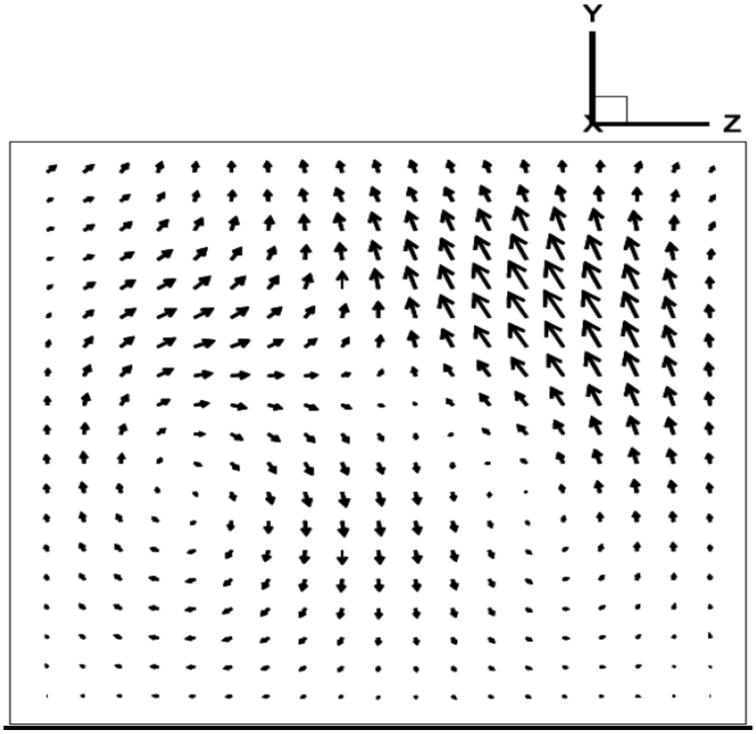

(a) t = 0

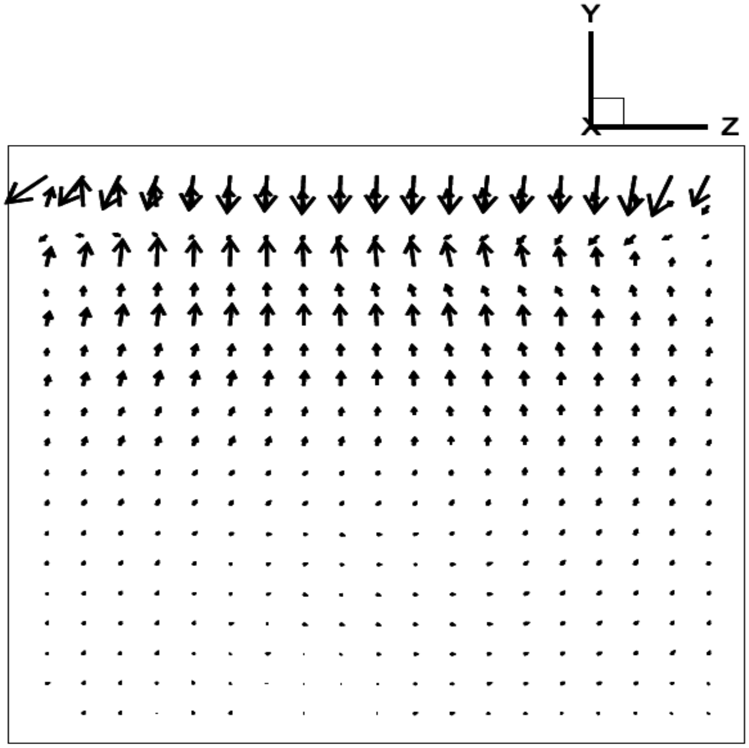

(b) t = T/8

Figure 4.17 $v - w$ velocity component in $x = 0.5$ plane, Re = 100, $\omega' = 0.4$
Starting instant t = 8T + 3/4T, $T = 2\pi/\omega'$

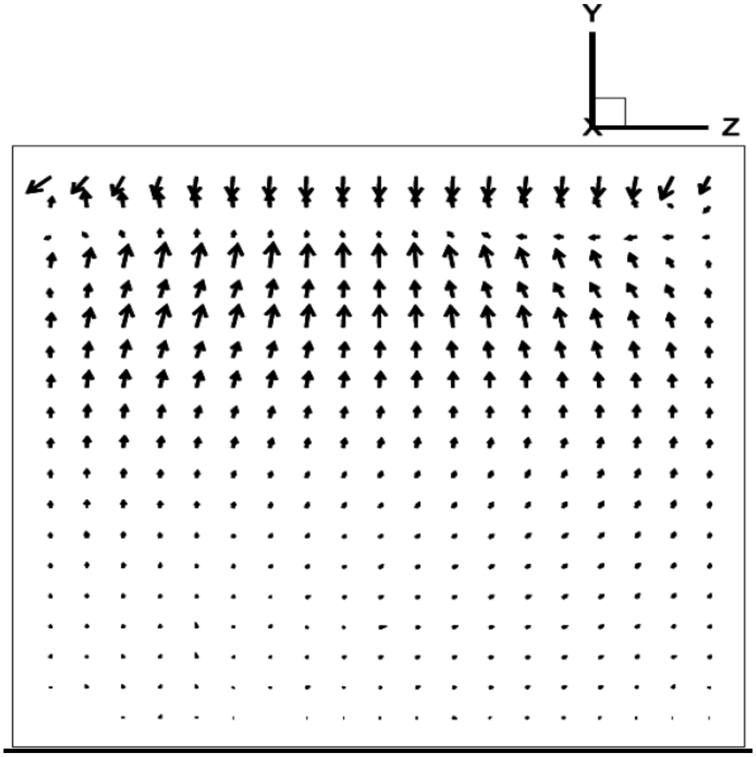

(c) t = T/4

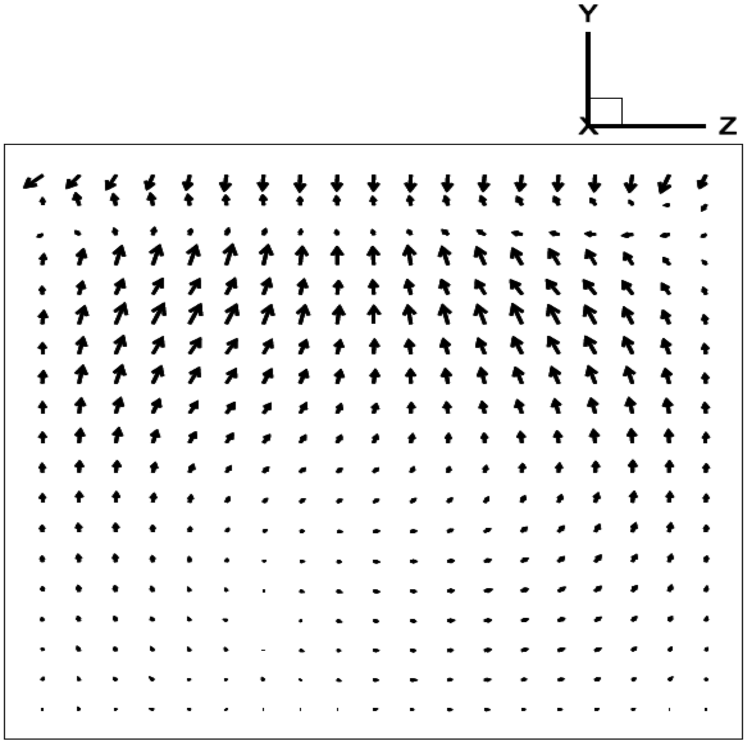

(d) t = 3/8T

Figure 4.17 (continued) $v - w$ velocity component in $x = 0.5$ plane, Re = 100, $\omega' = 0.4$, Starting instant t = 8T + 3/4T, $T = 2\pi/\omega'$

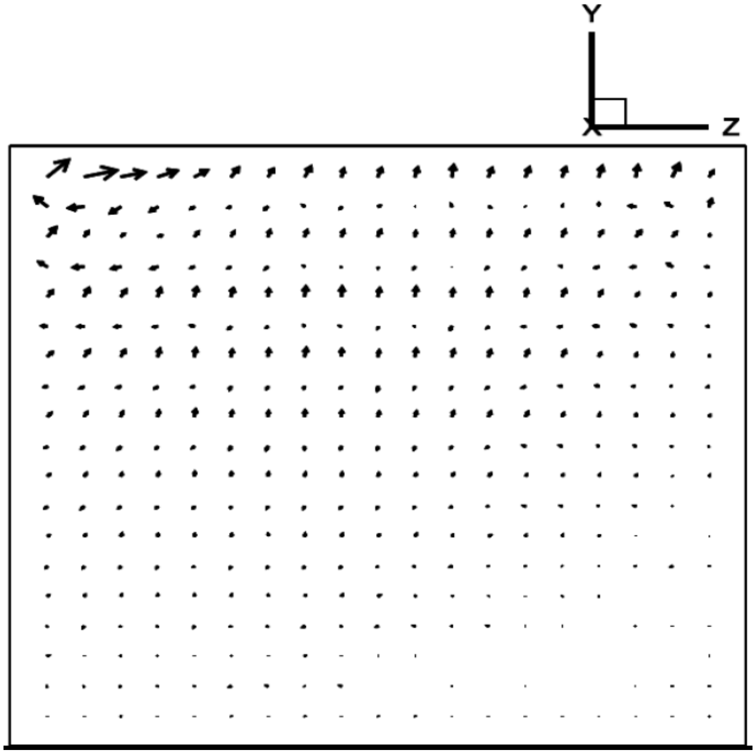

(a) t = 0

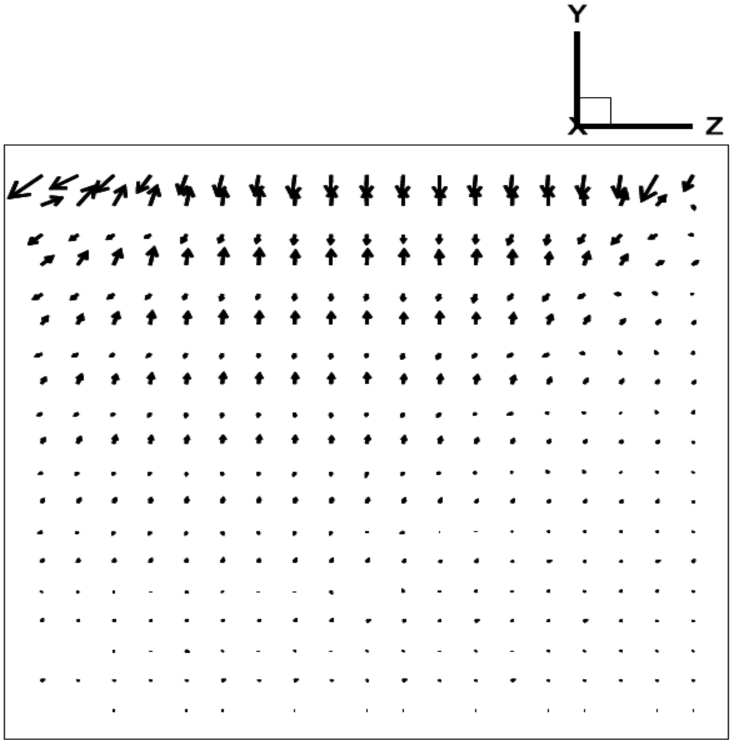

(b) t = T/8

Figure 4.18 $v - w$ velocity component in $x = 0.5$ plane, Re = 100, $\omega' = 10.0$
Starting instant t = 8T + 3/4T, $T = 2\pi/\omega'$

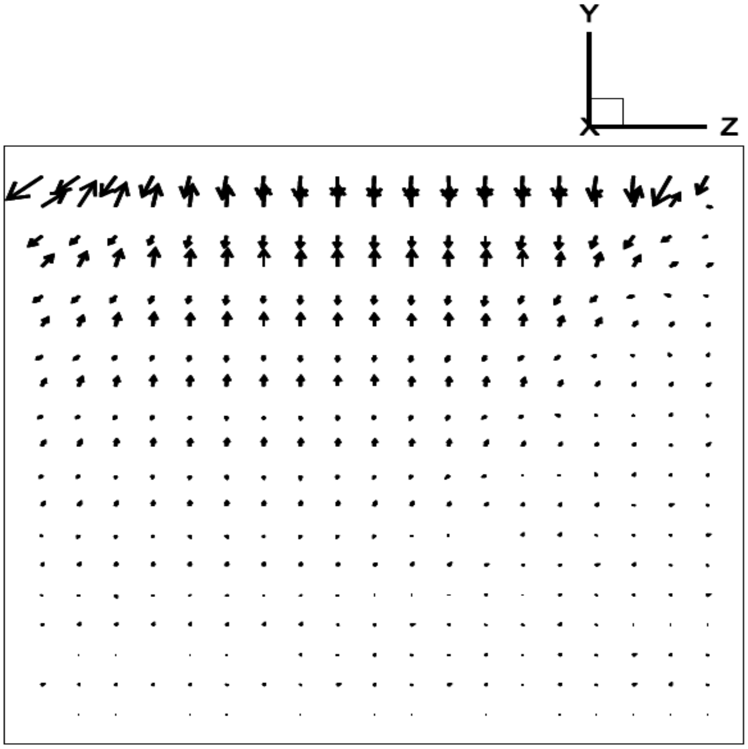

(c) t = T/4

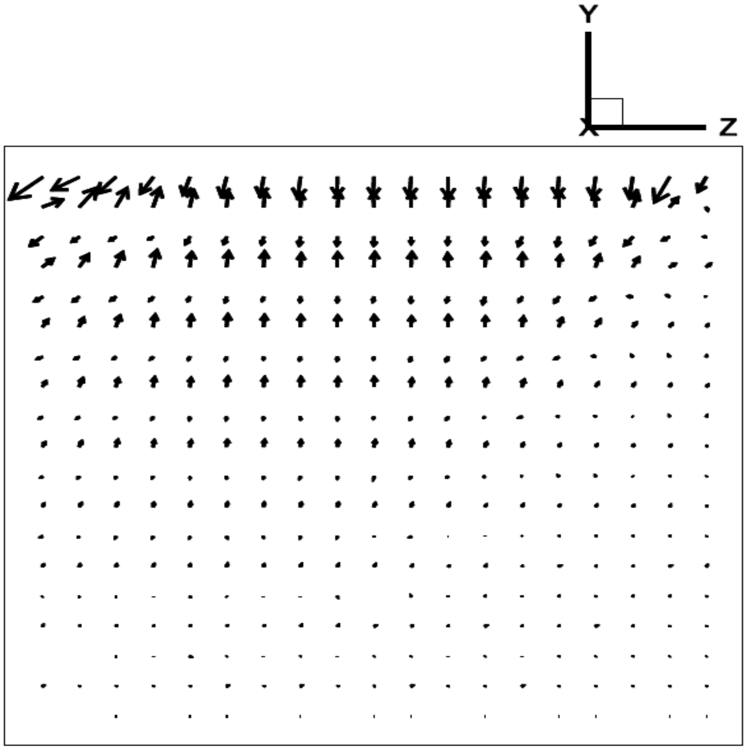

(d) t = 3/8T

Figure 4.18 (continued) $v - w$ velocity component in $x = 0.5$ plane, Re = 100, $\omega' = 10.0$, Starting instant t = 8T + 3/4T, $T = 2\pi/\omega'$

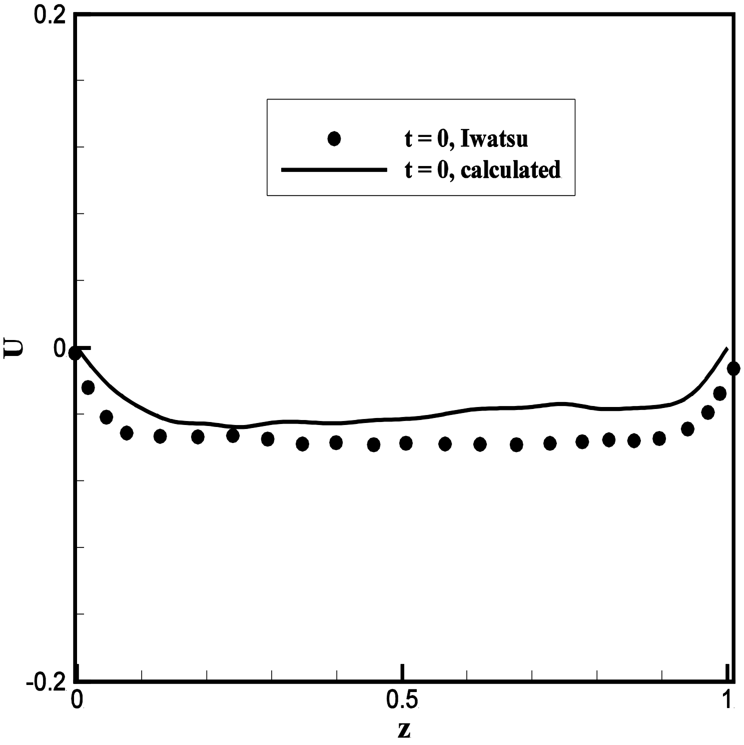

(a) t = 0

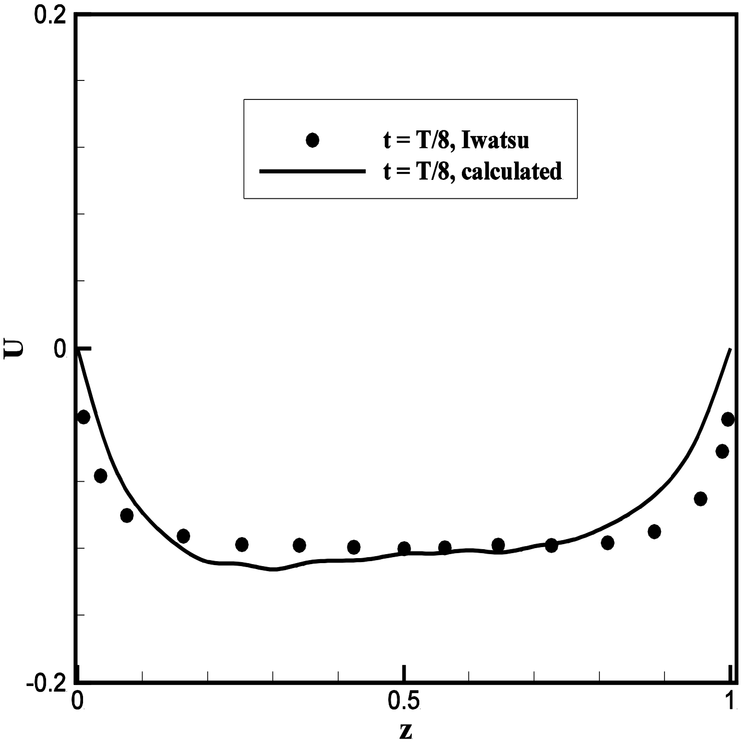

(b) t = T/8

Figure 4.19 Transverse (z) variation of u along $x = 0.5$ and $y = 0.75$, Re = 100, $\omega' = 0.4$ Starting instant t = 17T + 3/4T, $T = 2\pi/\omega'$

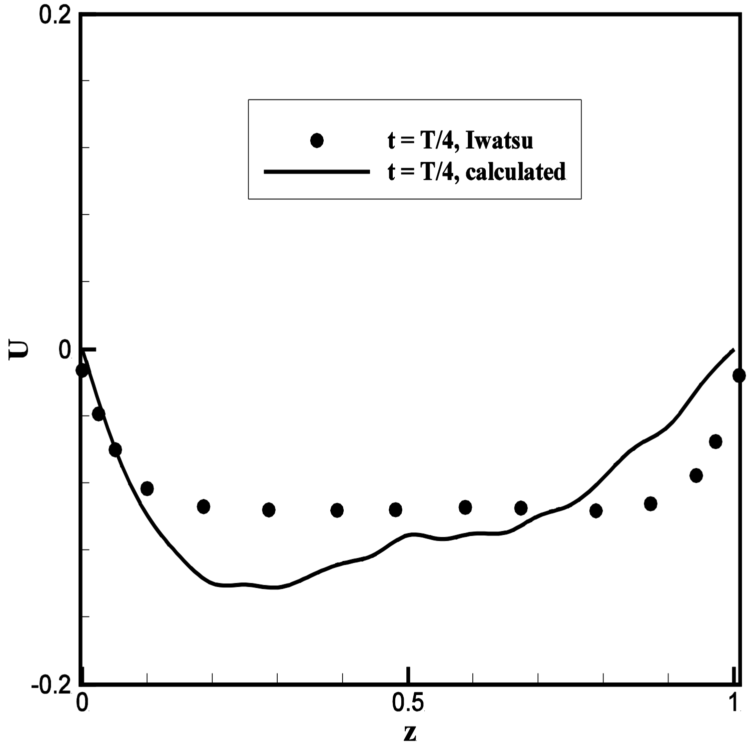

(c) t = T/4

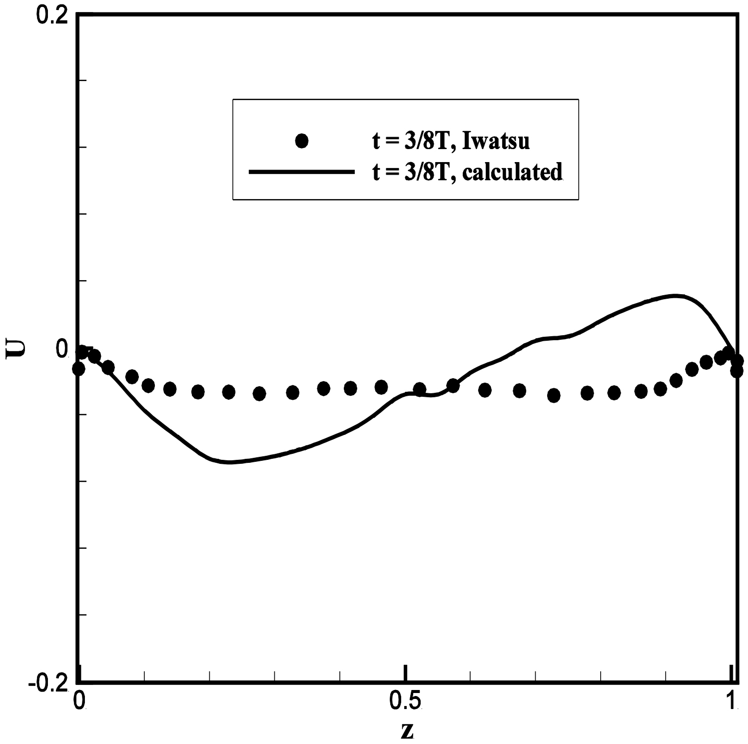

(d) t = 3/8T

Figure 4.19 (continued) Transverse (z) variation of u along $x = 0.5$ and $y = 0.75$, Re = 100, $\omega' = 0.4$, Starting instant t = 17T + 3/4T, $T = 2\pi/\omega'$

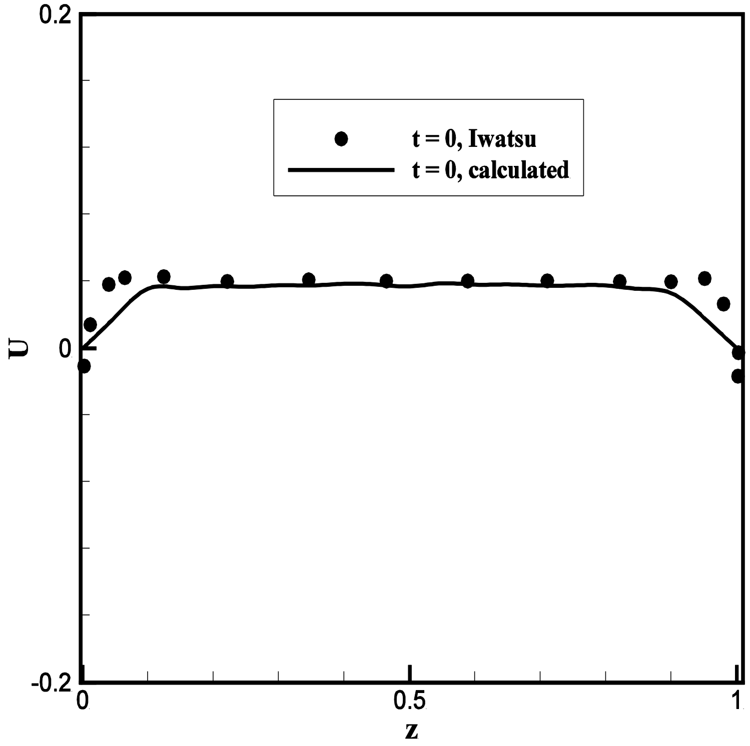

(a) t = 0

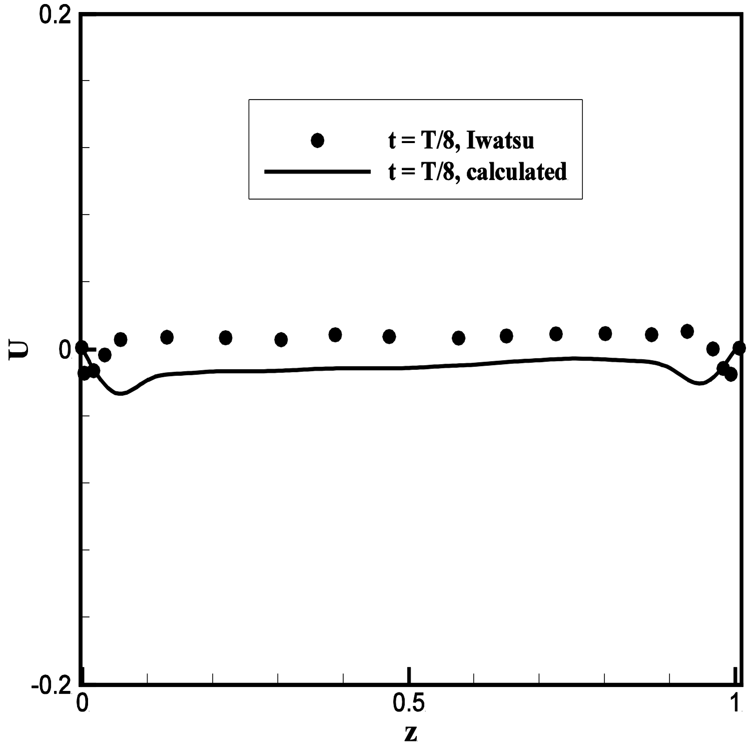

(b) t = T/8

Figure 4.20 Transverse (z) variation of u along $x = 0.5$ and $y = 0.75$, Re = 100, $\omega' = 10.0$ Starting instant t = 17T + 3/4T, $T = 2\pi/\omega'$

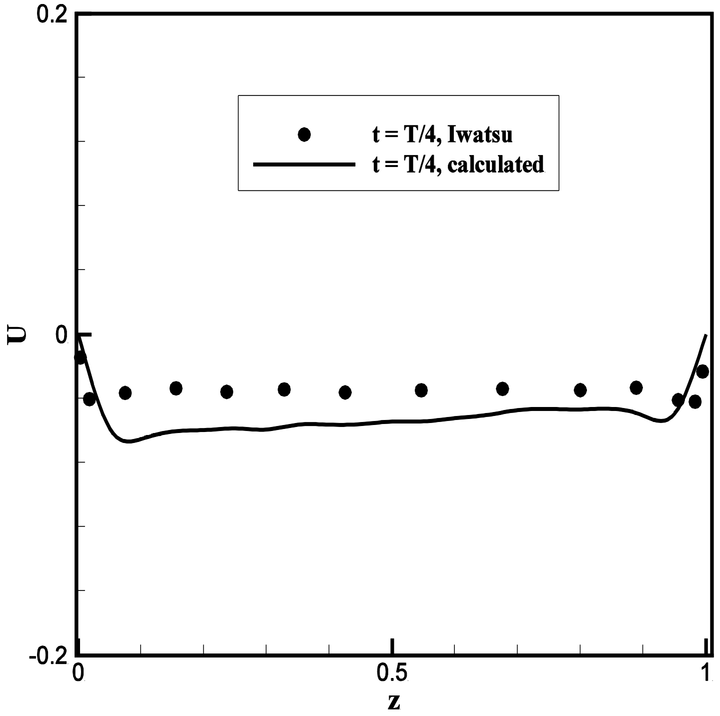

(c) t = T/4

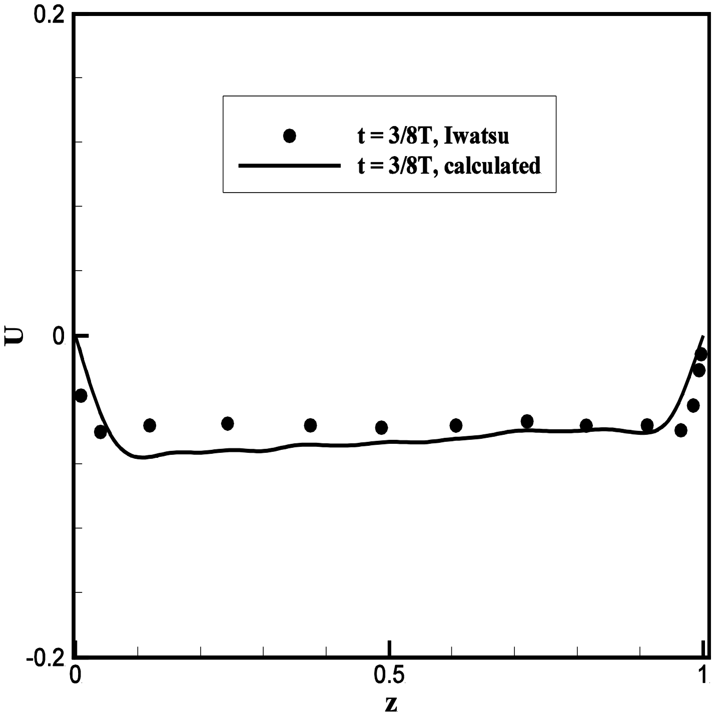

(d) t = 3/8T

Figure 4.20 (continued) Transverse (z) variation of u along $x = 0.5$ and $y = 0.75$, Re = 100 $\omega' = 10.0$, Starting instant t = 17T + 3/4T, $T = 2\pi/\omega'$

## 4.2 Unsteady Rotor : Validation

The discrete blade model is implemented in a well-tested 3-D Cartesian structured solver for benchmark testing of the new unsteady rotor model. The structured code uses finite volume primitive variable methodology to solve the unsteady, three-dimensional, laminar Navier-Stokes equations. A cell-centered first order spatial discretization scheme, using staggered cells, is used along with semi-implicit time integration. The influence of the rotor is incorporated in the form of momentum sources added to specific locations in the flowfield using the methodology described in Chapter-4. The flowfield is then solved for iteratively using the SIMPLER algorithm. The details of the structured flow solver are given in Ref. [49].

Three isolated hovering rotors, in and out of ground effect, are chosen to validate the unsteady rotor model with the structured solver. Three-dimensional Cartesian structured grids of sizes (78 x 78 x 71) , (93 x 93 x 66) and (98 x 98 x 65) are used. The grid is designed to have a high density near the rotor and it becomes increasingly coarser farther away from the rotor. A constant relaxation factor of 0.05 is used in the solution of the tridiagonal linear system resulting from the discretization of the momentum equations. A sample Cartesian grid is shown in Fig. 4.21.

The first rotor that is simulated is the model helicopter rotor by Caradonna and Tung (referred here as Rotor I). The second test case is the Rabbot rotor (referred here as Rotor II), while the third case is taken from experiments conducted by J. S. Light (referred here as Rotor III). The details of these test cases are taken from [50], [51] and [52], respectively. The important geometric parameters for these rotors are given in Table 4.1.

In all, three hovering cases are simulated. Cases 1 and 2 use Rotors I and II in out-of-ground (freestream) condition. Case 3 simulates Rotor III in ground effect (IGE). The flight conditions are summarized in Table 4.2. In addition to this data, standard values are also assumed for the kinematic viscosity of air and the freestream pressure. For simplicity, pitch and flap harmonics greater than the first are ignored. The lagging motion is also ignored. It must be noted here that Rotor III has the NPL9615 airfoil, whose airfoil data was not available. Case 3, which uses Rotor III, is therefore simulated using the standard NACA-0012 airfoil with the collective

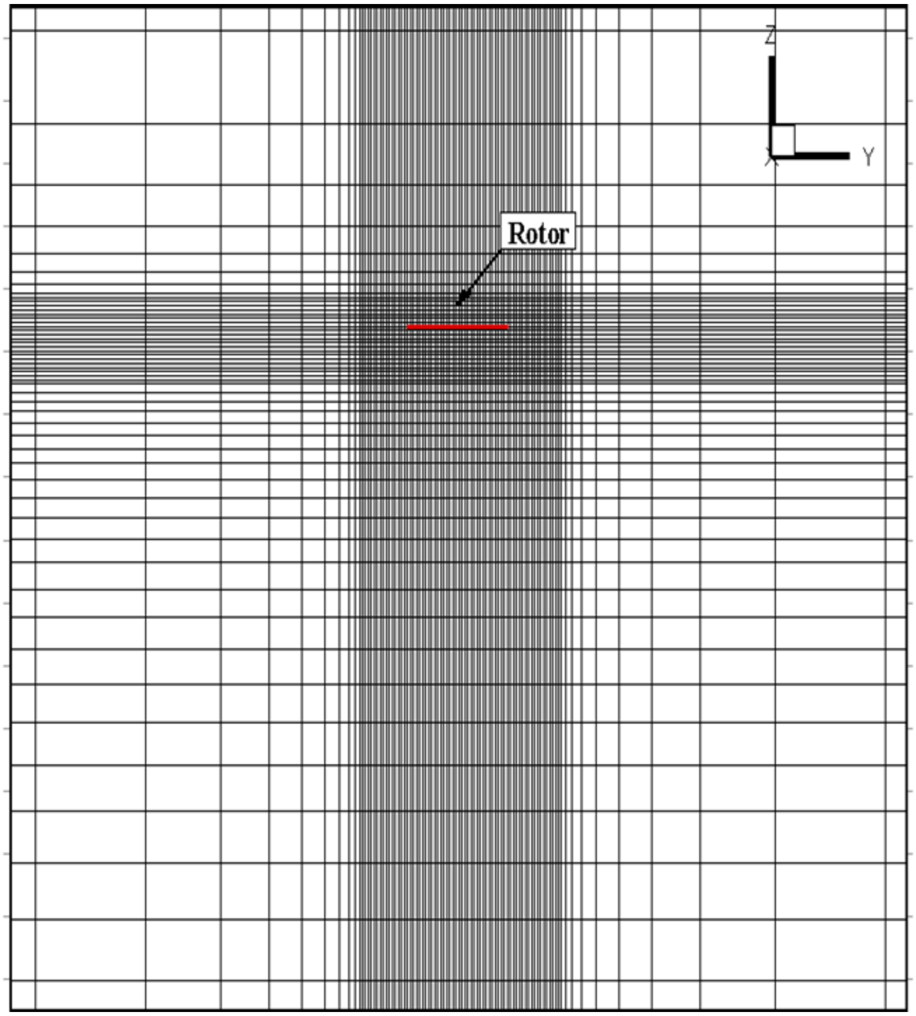

Figure 4.21 Cartesian structured grid

pitch adjusted to the same $C_T$ as the experiments. For this IGE hovering case, various rotor heights above the ground are presented.

### 4.2.1 Case 1: Caradonna Rotor

Simulations for Rotor - I in hover were conducted over a range of collective pitch angles. Flowfield as well as rotor loading was obtained using a time step of 0.005, with Crank-Nicolson time integration scheme. Correctly predicting the loading on the rotor blades is essential for evaluating the overall performance of the rotor. Blade load prediction can, therefore, serve as a crucial validation test for a rotor model. For Rotor-I in hover, the spanwise sectional lift

Table 4.1 Rotor Geometric Properties

| | Rotor I | Rotor II | Rotor III |
|---|---|---|---|
| Rotor radius, R (m) | 1.143 | 2.3241 | 1.105 |
| Chord, c (m) | 0.191 | 0.36 | 0.180 |
| Number of blades, $N_b$ | 2 | 2 | 4 |
| Collective Pitch, $\theta_c$ (deg.) | 2-12 | 3-9.2 | 13-19 |
| Reference twist, $\theta_{tw}$ (deg.) | 0 | 0 | 0 |
| Root cutout | 0.19R | 0.15R | 0.208R |
| Hinge offset | 0.0925R | 0 | 0 |
| Solidity, $N_b c/\pi R$ | 0.106 | 0.099 | 0.208 |
| Airfoil | NACA-0012 | NACA-0012 | NPL9615 |

Table 4.2 Summary of Test Cases

| | Case 1 | Case 2 | Case 3 |
|---|---|---|---|
| Rotor | I | II | III |
| $V_\infty, m/sec$ | 0.1 | 0.1 | 1.0 |
| $V_{tip}, m/sec$ | 149.58 | 151.3 | 204.2 |
| $\Omega_{tip}, rad/sec$ | 130.83 | 65.1 | 184.8 |
| $T, sec$ | 0.048 | 0.097 | 0.034 |
| $\alpha_D, deg$ | 0 | 0 | 0 |
| $\rho_\infty$, kg/m$^3$ | 1.2389 | 1.225 | 1.225 |

variation on the blades is computed and compared to experimental results. This is presented in Fig. 4.22 for a collective pitch of $8^0$ and $12^0$. The figures represent the instantaneous loading on the blades at $\psi = 0^0$ after 100 rotor rotations. The calculated results match well with the experimental data. The deviation near the outboard region of the blade is due to the absence of any tip correction to ensure that the lift at the tip of the rotor goes to zero. Tip correction will be explained in detail and implemented in a later section.

In Fig. 4.23, the pressure contours for Rotor-I above and below the rotor plane, for a collective pitch of $12^0$, are depicted. Fig. 4.24 shows the pressure contours on a cross plane passing through the center of the rotor, depicting the zero pressure contour cutting through the center of the rotor and also viewed is a variation of pressure coefficient along the radius. The appropriate pressure distribution, with high pressure below the rotor and low pressure above the rotor, is observed in these figures. Moreover, in Fig. 4.23, the pressure is localized over a narrow azimuth, which illustrates the fact that the unsteady rotor source is applied to a specific region where the blades are present and not throughout the rotor disk plane as in the steady rotor model. It can be seen that the pressure differential approaches zero near the tip and that the physics of the flow is correctly maintained by the current procedure. In Fig. 4.25, streamlines for Rotor-I in hover are plotted and a large contraction of the flow due to the rotor is observed.

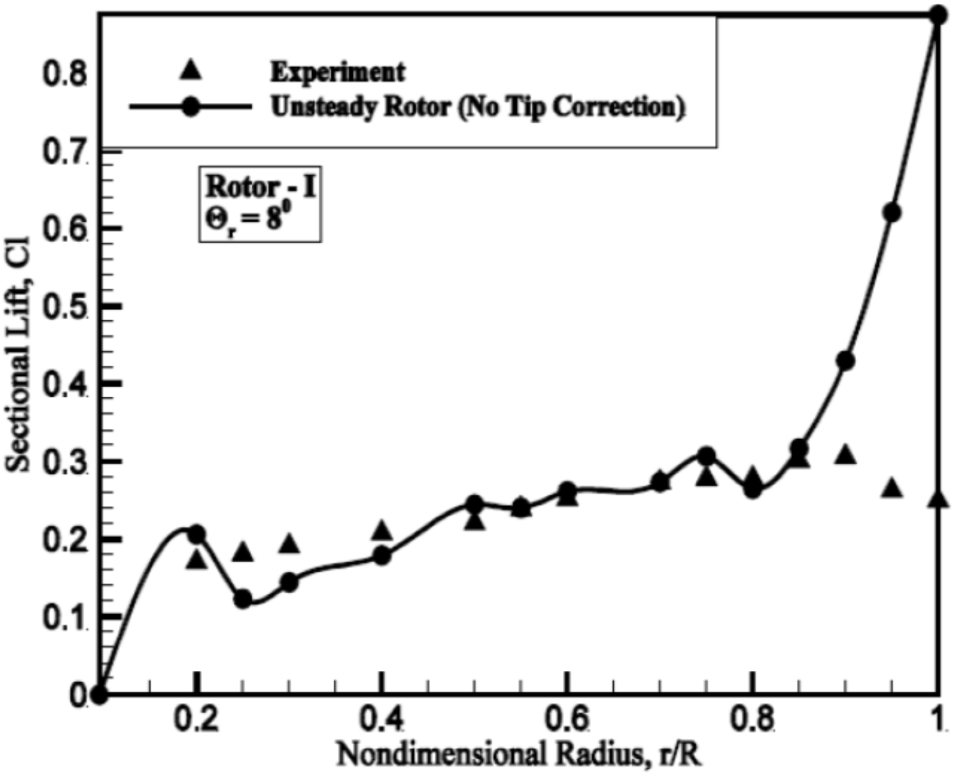

(a) $\theta_c = 8^0$

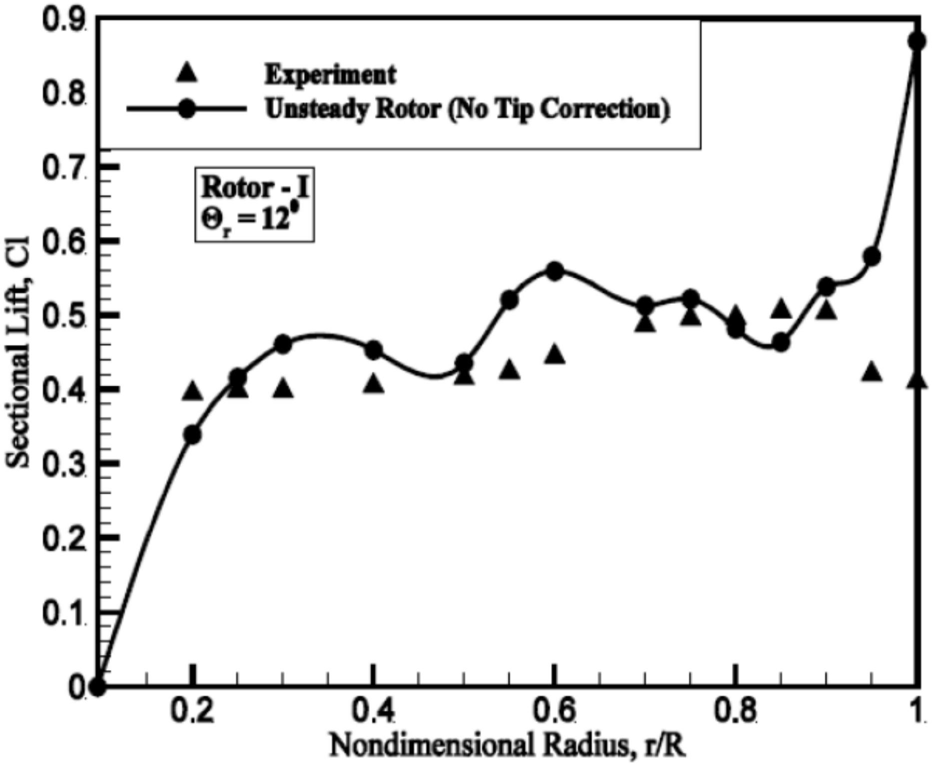

(b) $\theta_c = 12^0$

Figure 4.22 Spanwise sectional lift, Rotor - I

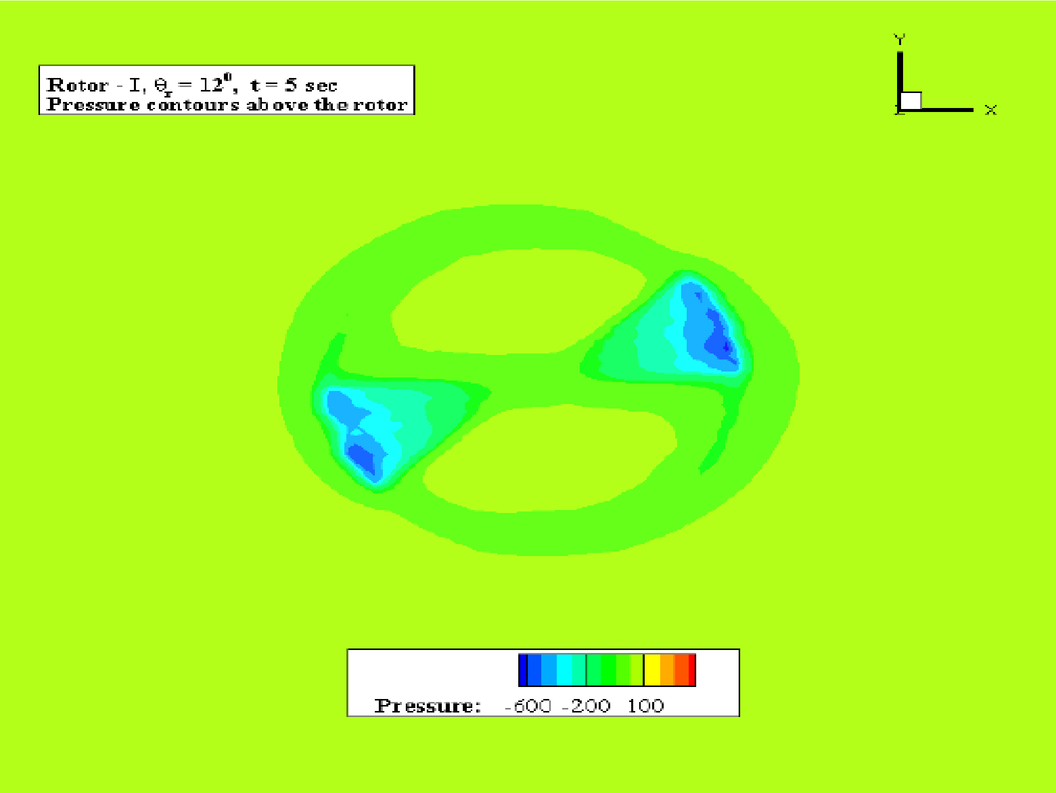

(a) Pressure above

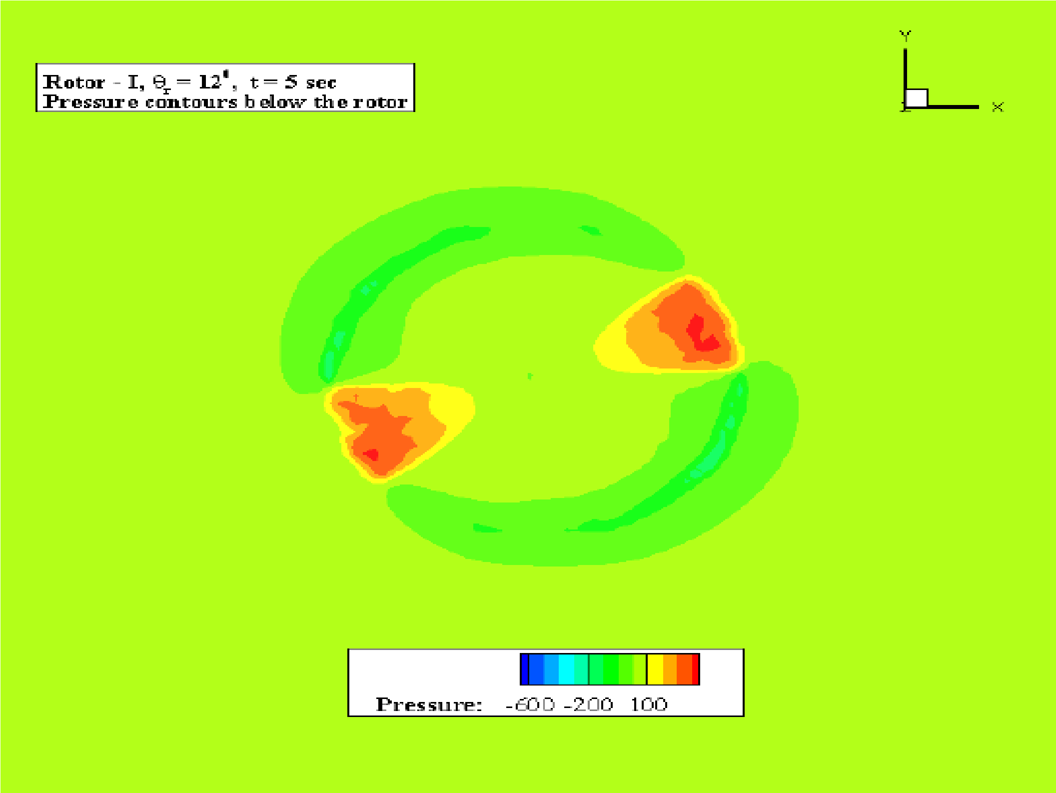

(b) Pressure below

Figure 4.23 Pressure contours on rotor plane, Rotor - I

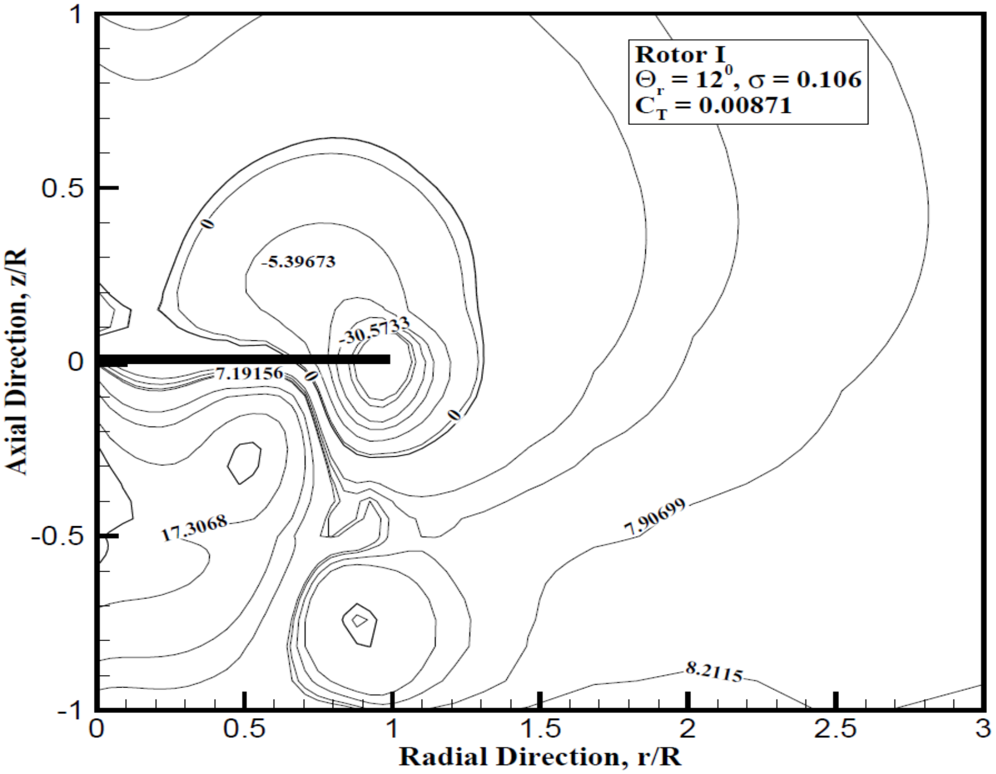

(a) Cross plane pressure

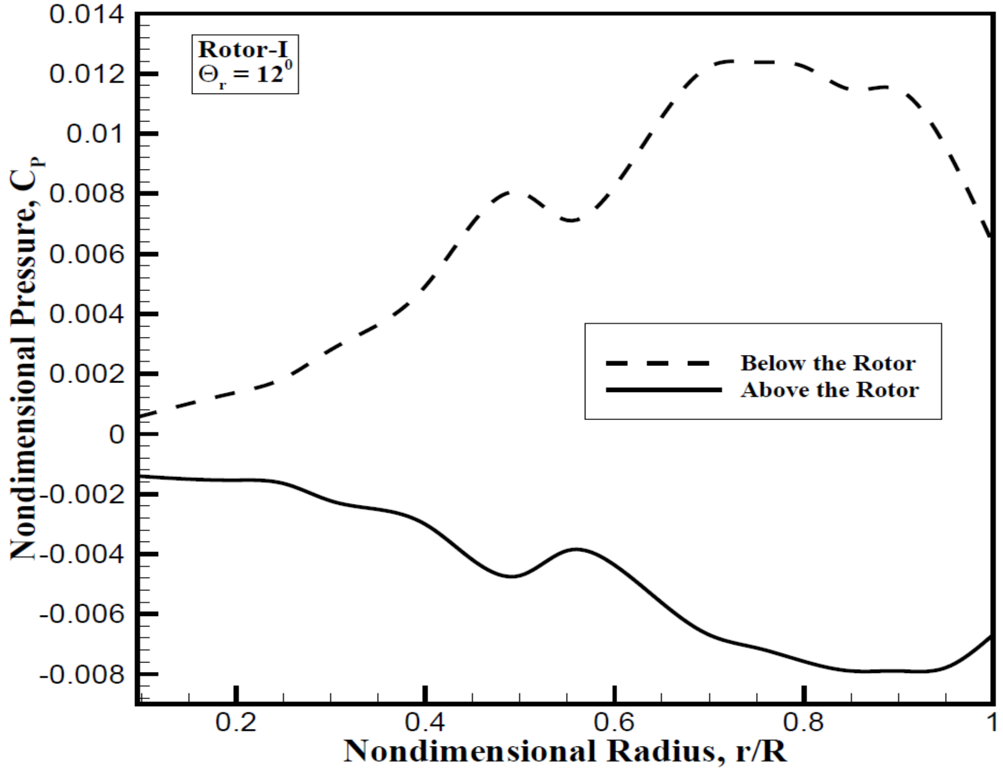

(b) Coefficient of pressure

Figure 4.24 Rotor - I, $\theta_c = 12^0$

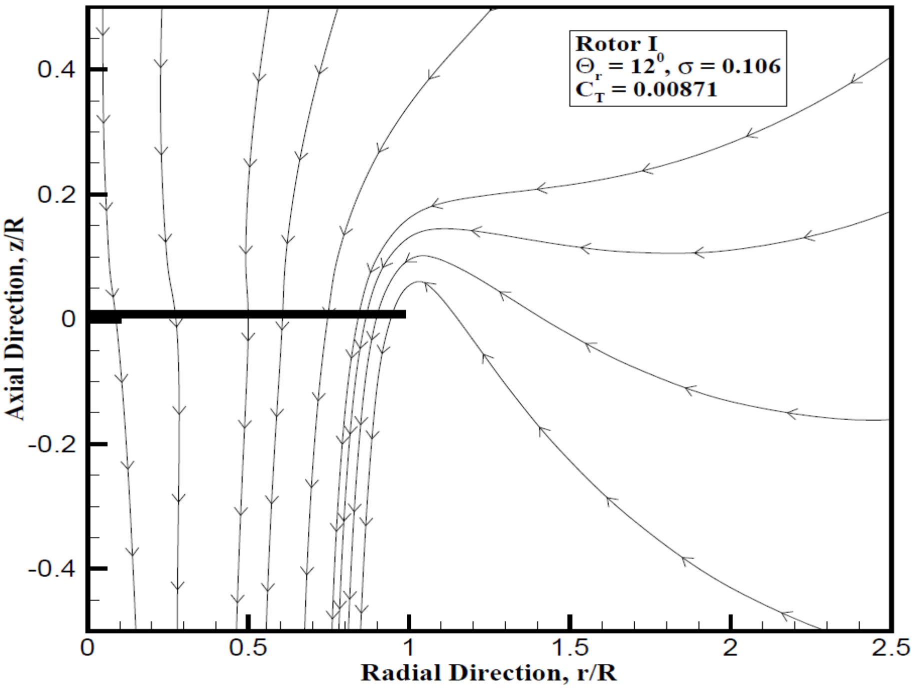

Figure 4.25 Streamlines near the rotor, Rotor - I, $\theta_c = 12^0$

A rotor changes the momentum of the streamtube that passes through it and in doing so, it imparts a rotation to the flow. For a rotor in hover, the vortices shed from the blade tip convect downwards to form a helical wake structure. The position and strength of these vortices and their interaction with each other as well as with the rotor blades affect the blade loading and the aero-acoustic characteristics of the rotor. Also, it is believed that in helicopter Brownout, the tip vortices play an important role in lifting up the dust from the surface. Predicting the position and structure of these vortices is, therefore, an important task.

The present rotor model attempts to predict the flow field in a time accurate manner and capture discrete vortices. But for the current case of Rotor-I, induced velocity at the rotor was not high enough to convect the tip vortices, so that they can be visualized as discrete cores before they get diffused. Also, a higher grid resolution is required to preserve the vortex cores upto a considerable distance below the rotor. Therefore, it was not possible to visualize the vortex cores in the rotor wake. However, the cumulative path followed by the tip vortices could be traced by analyzing the vorticity contours. Fig. 4.26 depicts the magnitude of the nondimensional vorticity along the rotor. It is observed that the magnitude of vorticity increases rapidly from a zero value outside the wake to a maximum value in a short radial distance into the wake and it again falls steeply to a minimum value. The position of the tip vortex core is taken to be at the point of maximum vorticity and the tip vortex path calculated in this manner is depicted in Fig. 4.27.

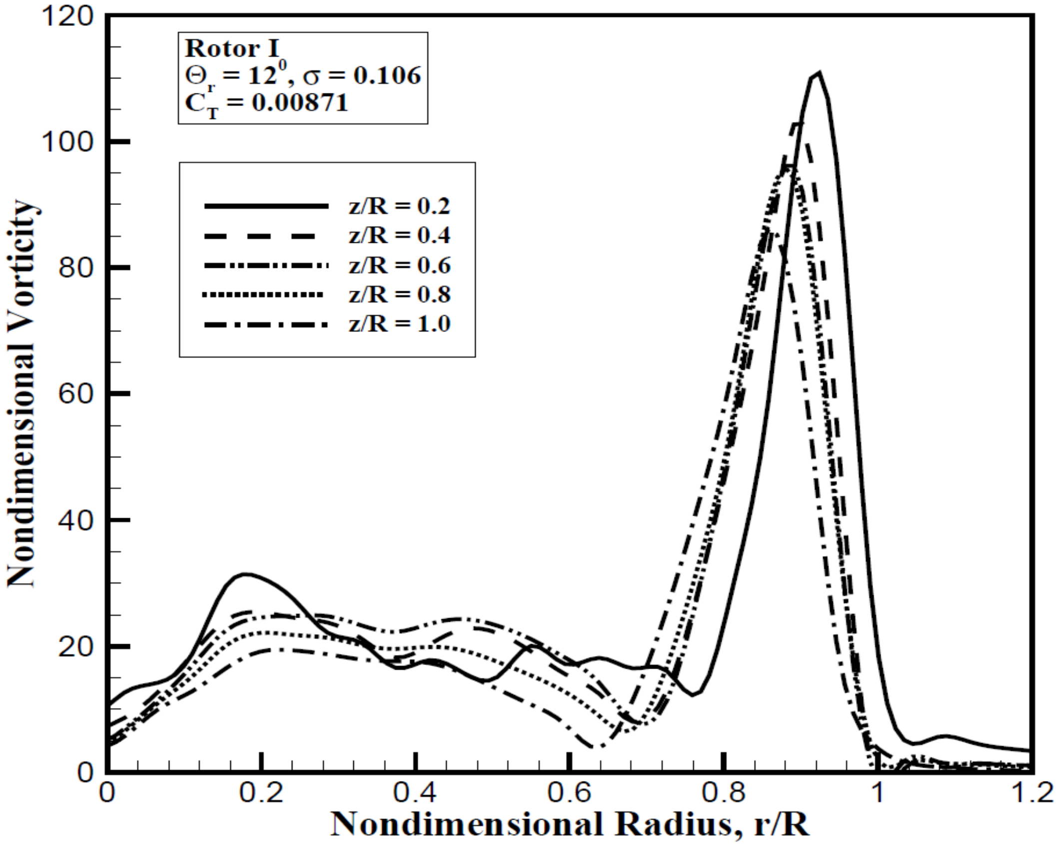

Figure 4.26 Nondimensional vorticity along the rotor, Rotor - I, $\theta_c = 12^0$

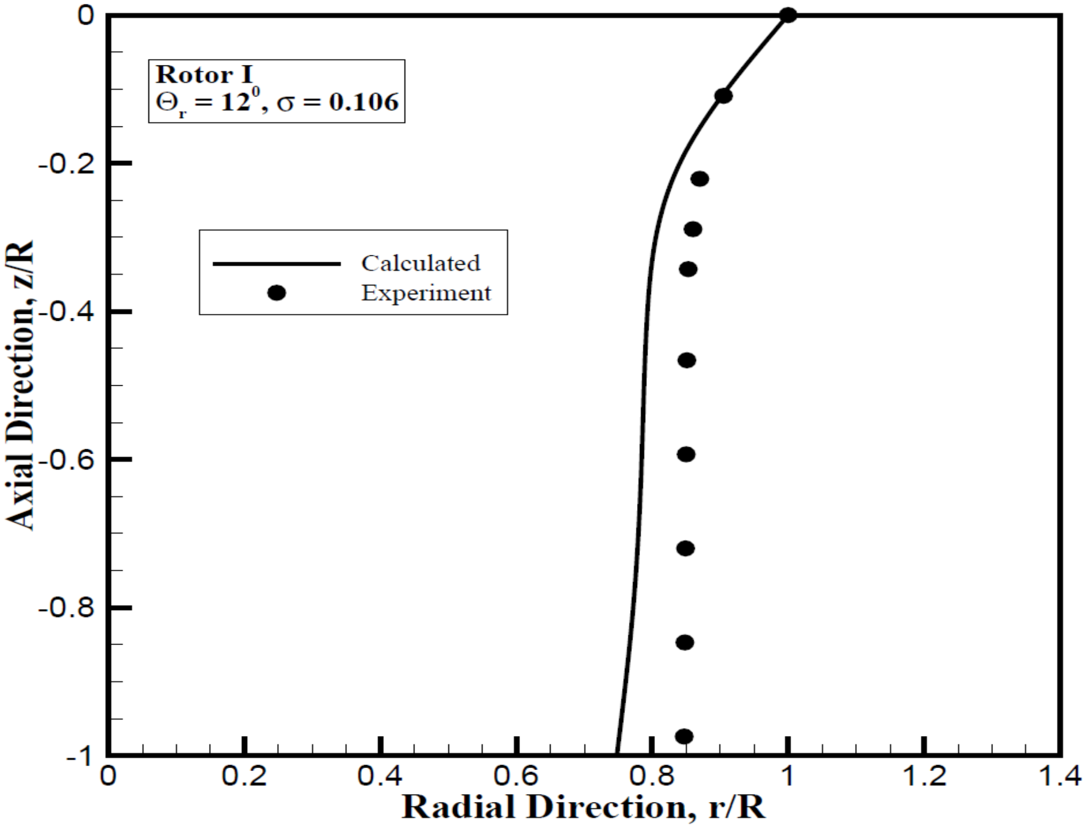

Figure 4.27 Tip vortex path, Rotor - I, $\theta_c = 12^0$

### 4.2.2 Case 2 : Rabbot Rotor

For the Rabbot rotor i.e. Rotor - II, a hover flight condition was simulated for various collective pitch angles and blade loading as well as the rotor flow behavior was studied. The spanwise loading on the rotor blade was computed and compared to experiment. In doing so, tip correction was applied to account for the pressure equalizing effect that is observed near the tip of the rotor. The tip correction procedure is briefly explained here [39]. At the tip, the pressure difference approaches zero while the angle of attack increases steeply. In reality, the lift at the tip of a rotor should go to zero. A simple procedure is used here to account for the actual three dimensional pressure distribution and the resulting sectional characteristics in this region. The pressure difference between the top and bottom of the rotor is computed at an outboard blade location of about 0.9R (taken as $r_{ref}$) and the difference in pressure beyond this location is divided by the difference in pressure at $r_{ref}$ to yield a correction factor for the angle of attack. Thus, a corrected angle of attack $\alpha_c$ is now used to look up the sectional characteristics at the tip.

$$\alpha_c = \{\alpha - \alpha_o\} * abs\{\frac{\Delta p_r}{\Delta p_{ref}}\}\{\frac{R-r}{R-r_{ref}}\} + \alpha_o \tag{4.3}$$

where, $\alpha_o$ is the zero lift angle of attack, $\Delta p_r$ refers to the pressure difference between the grid points above and below the rotor at a radial position $r$ and $ref$ refers to the location along the blade span where the correction procedure starts. Fig. 4.28 shows the radially varying aerodynamic loading for Rotor-II with tip correction for different values of collective pitch angles. It can be observed that tip correction improves the result in the outboard region, as compared to the no-tip correction results obtained for Rotor-I, and an overall good match with the experimental data is achieved.

A comparison of the rotor load predictions by the steady and unsteady rotor models is made in Fig. 4.29. It is interesting to note that both the steady and unsteady rotor models capture the overall blade loading trend, with the unsteady model coming closer to the experimental values. In Figs. 4.28-4.29, the calculated data represents the instantaneous loading on the blades at $\psi = 0^0$ after 50 rotor rotations.

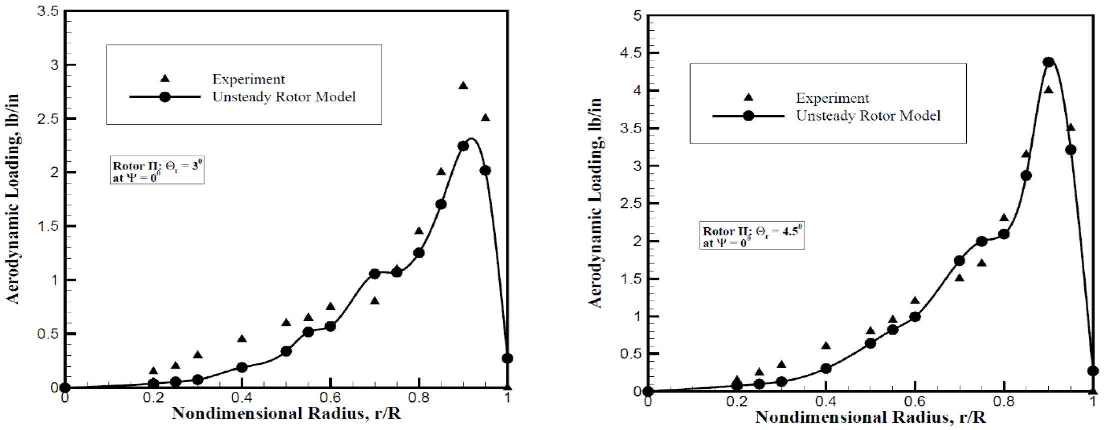

(a) $\theta_c = 3^0$ (b) $\theta_c = 4.5^0$

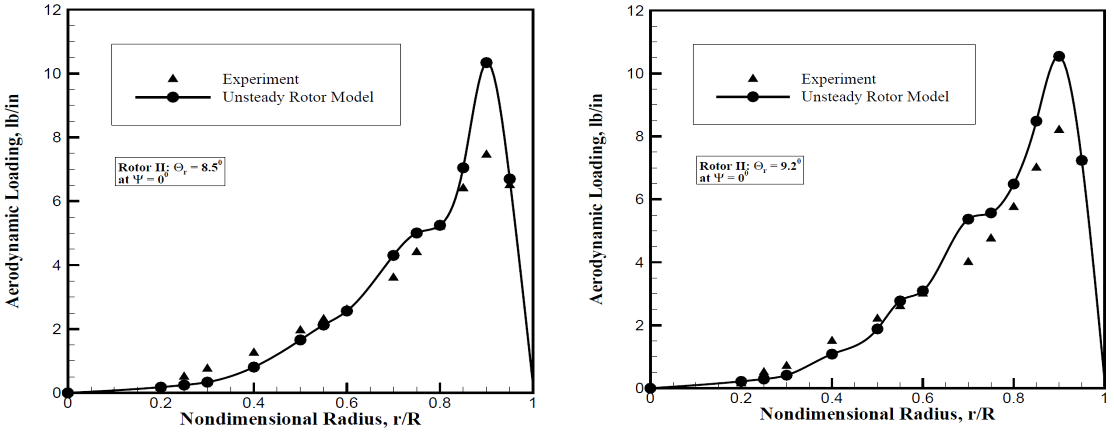

(c) $\theta_c = 8.5^0$ (d) $\theta_c = 9.2^0$

Figure 4.28 Spanwise aerodynamic loading, Rotor - II

For a rotor in hover, Figure of Merit (FM) is an important parameter that defines the rotor's efficiency. FM is calculated for Rotor-II operating at various $C_T$ values and is compared to the experimental values in Fig. 4.30(a). It can be observed that the present discrete blade unsteady rotor model makes a reasonable prediction of this parameter and thus, reliably estimates the efficiency of a hovering rotor. Also, the total thrust produced by a rotor and the torque required to generate this thrust are important considerations in designing the rotor and any analysis tool should be able to predict them. Fig. 4.30(b) presents the variation of the thrust coefficient $C_T$ with the blade collective pitch $\theta_c$. Since experimental data is not available for very high values of $\theta_c$, a comparison is made over a moderate range of blade pitch angles and the expected

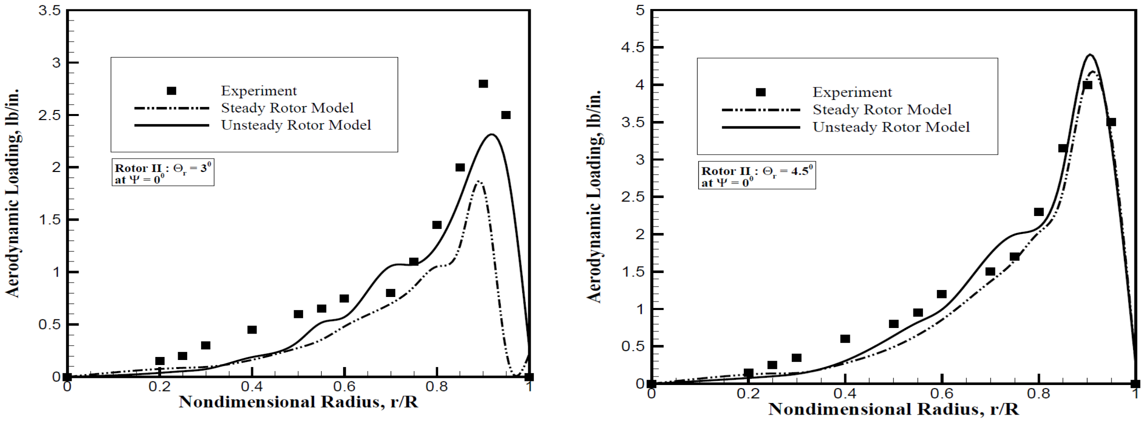

(a) $\theta_c = 3^0$

(b) $\theta_c = 4.5^0$

Figure 4.29 Spanwise aerodynamic loading comparison, Rotor - II

linear increase of $C_T$ with the root pitch is observed. In Fig. 4.30(c), predicted variation of the thrust coefficient with the coefficient of torque for Rotor-II is seen to compare well with the experimental data. It should be noted here that the $C_T$ and $C_Q$ values are averaged over 50 rotor rotations.

The unsteady behavior of the present rotor model is studied by comparing the time history of the thrust coefficient and comparing it with the steady rotor model. This is shown in Fig 4.31. In Fig. 4.31(a), the time history of the thrust coefficient for each of the two blades of Rotor-II as well as for the entire rotor is depicted. The oscillations in the time history are possibly due to the interaction of the blade with the wake of the preceding blade, and to a lesser extent, are also an attribute of the numerical scheme. The overall $C_T$ for the rotor is seen to be the cumulative of the blade $C_T's$. It is not possible to capture such a discrete blade behavior with the steady rotor model, as is seen in Fig. 4.31(b).

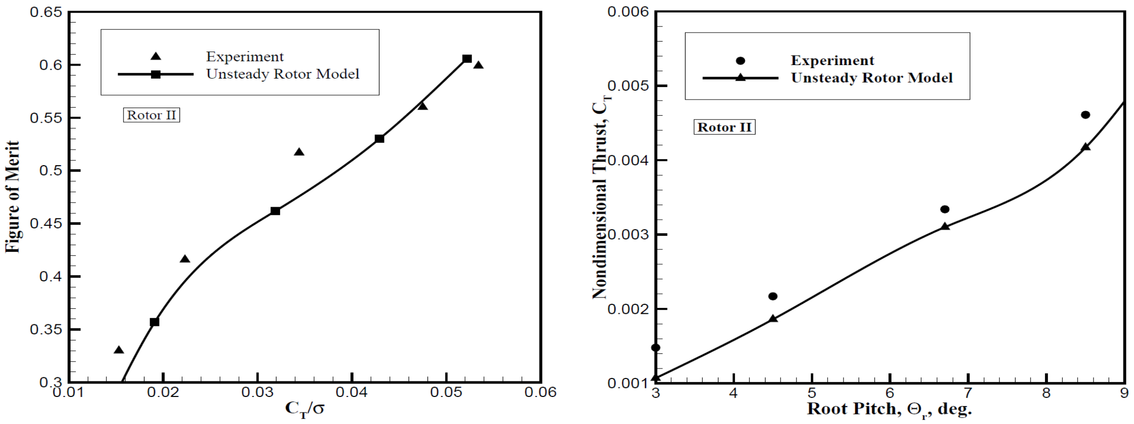

(a) Correlation of FM and thrust coefficient

(b) Effect of collective pitch on $C_T$

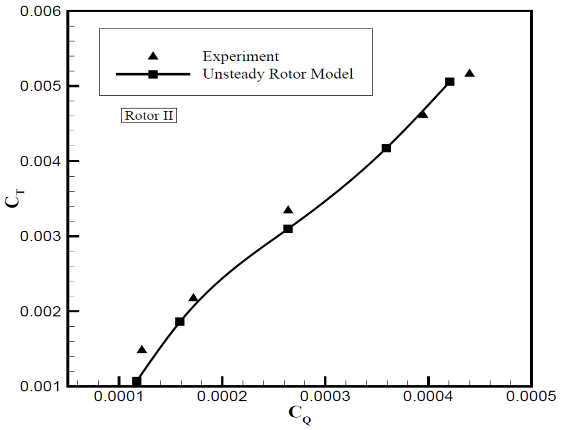

(c) Correlation of rotor thrust and torque

Figure 4.30 Performance characteristics, Rotor - II

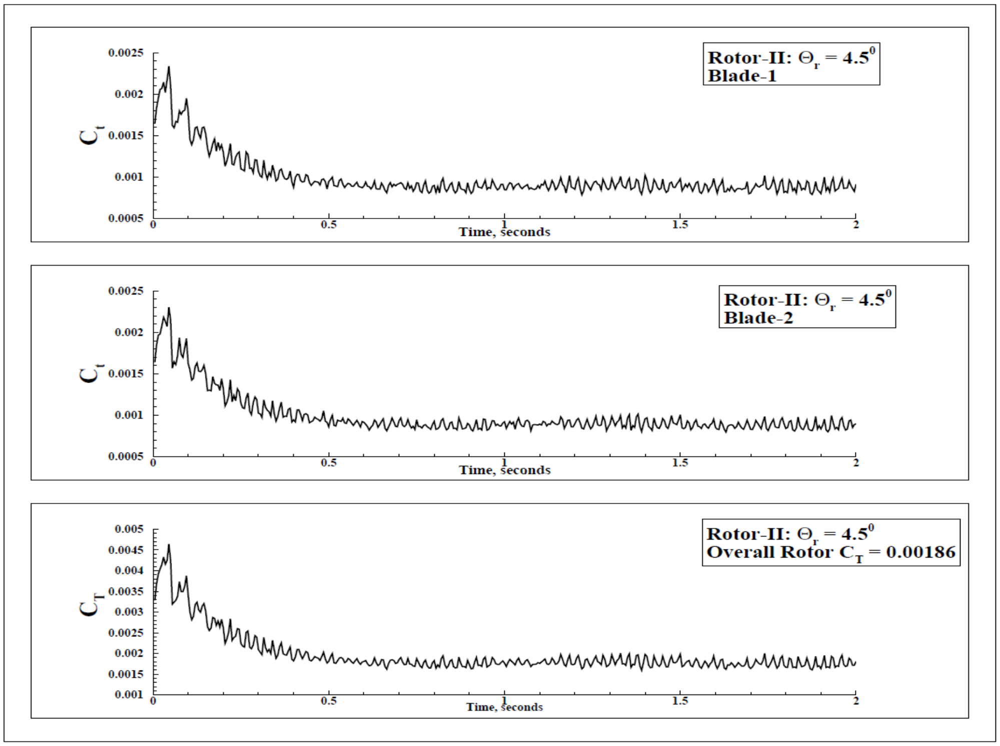

(a) Unsteady rotor model

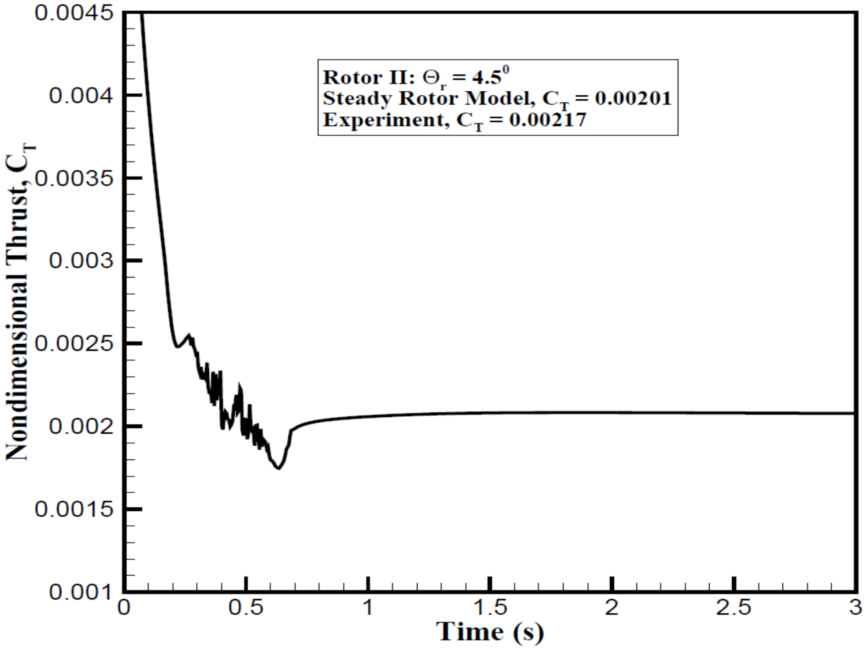

(b) Steady rotor model

Figure 4.31 Time history of thrust coefficient, Rotor - II

As a blade rotates, the pressure at a given point changes when the blade passes through it. In other words, a pressure pulse should be generated every time a blade passes through a point and this serves as an evidence of the discrete rotor blades and their unsteady effect on the flowfield. For an $n$-bladed rotor, there should be $n$-pulses observed within one time period. These pressure pulses are important from an aero-acoustic point of view and a rotor solution procedure should be able to capture this correctly. In order to study this phenomenon, a point lying in the plane of the rotor at $\psi = 0^0$, located at $r/R = 0.55$ is chosen. The schematic showing the location of this point on Rotor-II is given in Fig. 4.32. The solidity of the rotor is kept constant and the pressure at the schematic point 'P' for a two-bladed, three-bladed and four-bladed rotor are plotted in Fig. 4.33. It can be observed that the number of pressure pulses within one time period is the same as the number of blades, validating the unsteady, discrete blade rotor model.

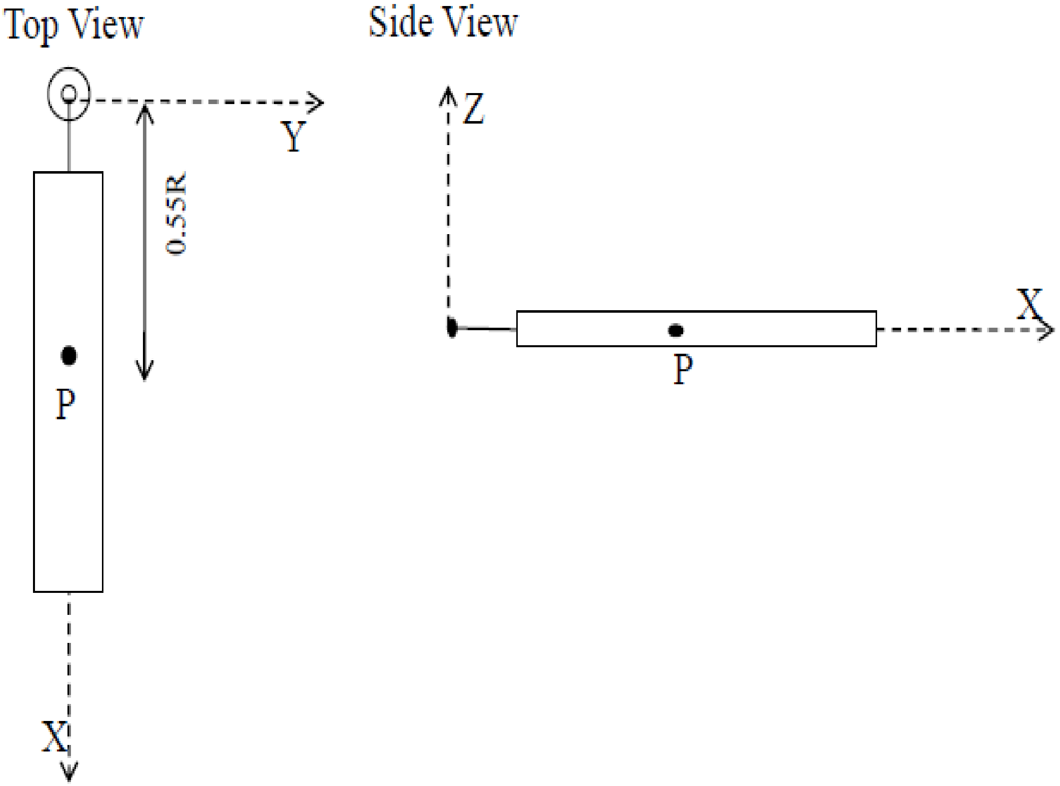

Figure 4.32 Location of test point on the blade for measuring pressure pulses

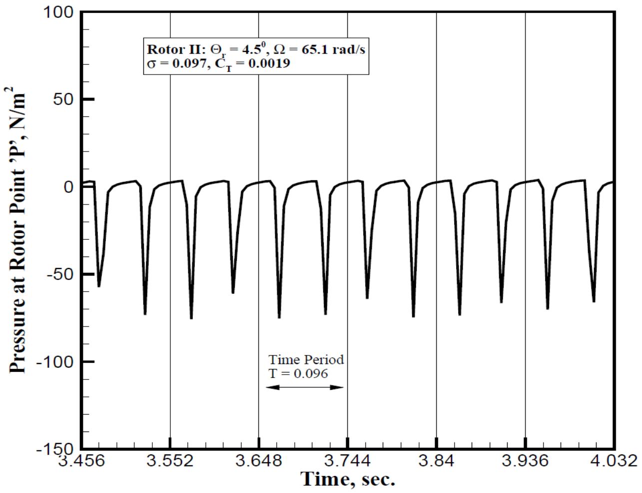

(a) 2-bladed

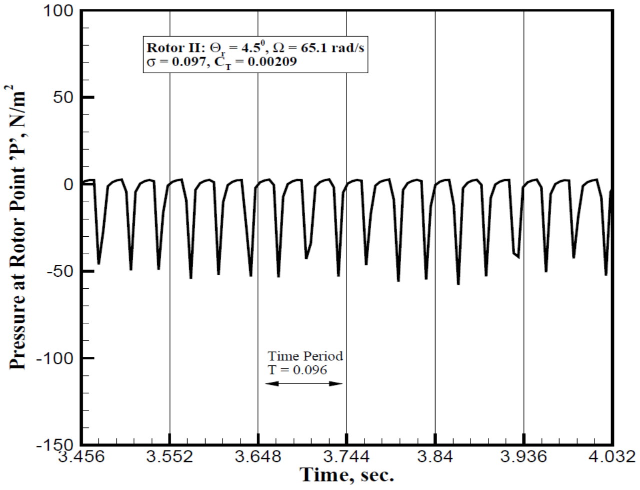

(b) 3-bladed

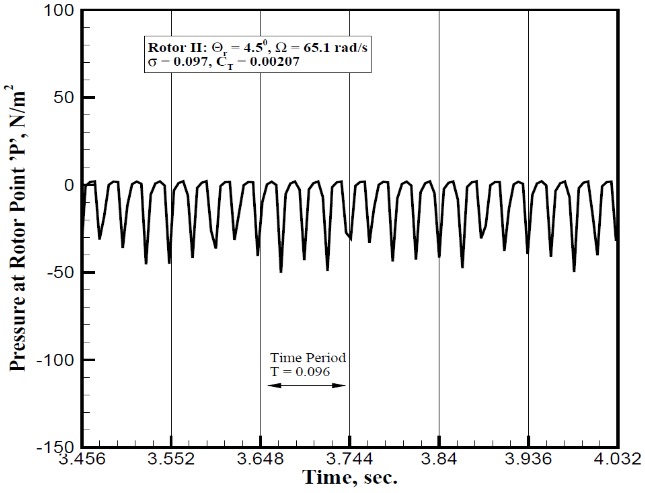

(c) 4-bladed

Figure 4.33 Pressure variation on a blade point with time, Rotor - II

Using the same procedure as described above, the axial induced velocity at the rotor for Rotor-II was also plotted as a function of time in Fig. 4.34. This plot is at $r/R = 0.7$ and an azimuthal position of $\psi = 0^0$. It can be seen in Fig. 4.34 that within each time period, two peaks are observed signifying the passage of two discrete blades. Periodicity with time is clearly captured. This further establishes the capability of the current rotor model in capturing the correct discrete behavior of the rotor flowfield.

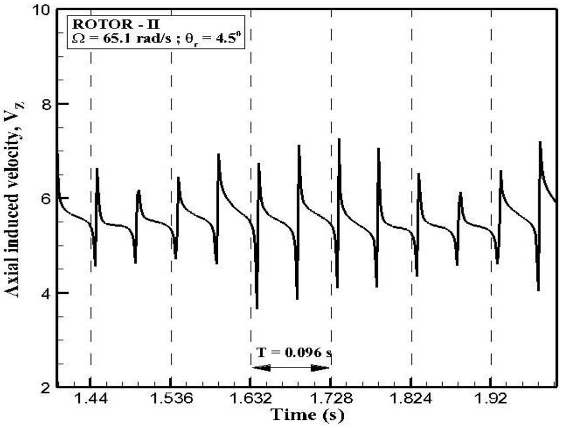

Figure 4.34 Axial induced velocity at $r/R = 0.7, \psi = 0^0$, Rotor - II

Next, various aspects of the flowfield for Rotor-II are visualized. The nondimensional induced velocity profiles for Rotor-II are shown in Fig. 4.35 as a function of the nondimensional radius. In Fig. 4.35(a), the axial velocity is seen to be near zero close to the inner and outer tips and reaches a maximum at 75 percent radius. The steep fall of the profiles near the root and the tip shows the ability of the current model in capturing the influence of the root cutout and the outer tip. Also, the streamtube through the rotor is seen to be converging with the velocities increasing as one goes farther into the wake (negative $z/R$ values represent the rotor wake). Fig. 4.35(b) depicts the nondimensional radial induced velocity $V_r/V_{tip}$ along the radius. The radial induced velocity profile at the rotor i.e. $z/R = 0.0$ is seen to be cutting across the plot, which shows that there is significant cross-flow toward the middle of the rotor from both the inner and outer tips. The higher velocities at the rotor near the outer ends is due to the presence of tips and the associated three-dimensionality of the flow near the tips. In Fig. 4.35(c), the nondimensional tangential velocities $V_\phi/V_{tip}$ at different axial locations along the rotor are plotted. In the wake, the tangential velocity, also known as the swirl velocity, is in the same sense as the rotor rotation. The swirl velocity is nearly zero until the flow reaches the rotor and thereafter, it increases rapidly well into the wake. The profiles at different axial locations are also seen to be converging asymptotically towards a limiting curve, which represents the fact that the streamtube through the rotor has converged to a constant cross section area. This signifies contraction of the wake and that the rotational component of velocity is confined only to the wake. The ability of the rotor model to capture wake contraction correctly is very crucial for its applicability to heavily loaded rotors.

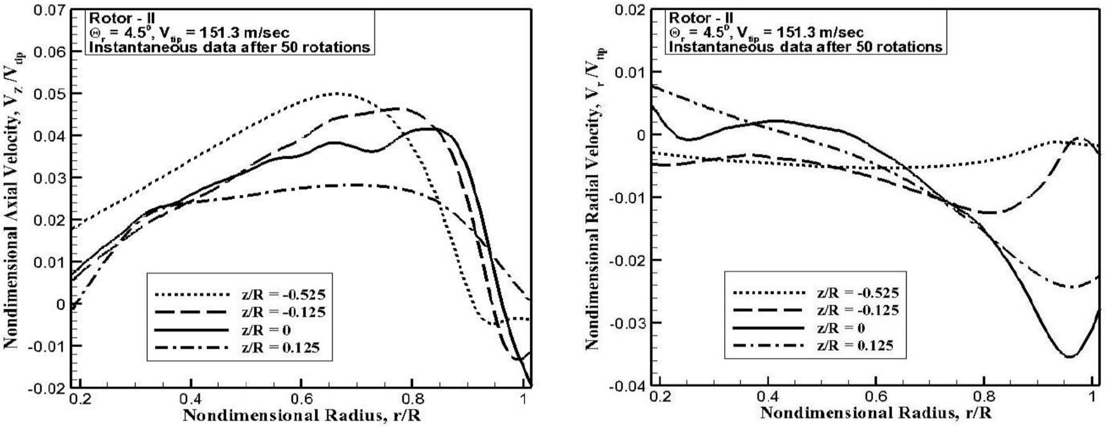

(a) Nondimensional axial velocity

(b) Nondimensional radial velocity

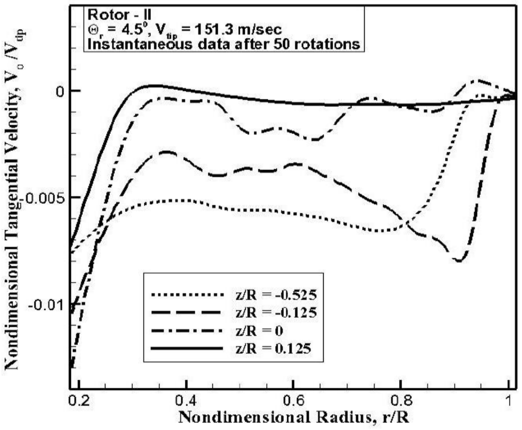

(c) Nondimensional tangential velocity

Figure 4.35 Induced velocity profiles, Rotor - II

In order to visualize discrete vortices for a rotor hovering in OGE, the '$\theta$' component of vorticity in different $(r - z)$ planes is visualized for Rotor-II. The data is obtained by moving the plane of observation in positive '$\theta$' direction in increments of $7^0$ while the rotor blades rotate in negative $\theta$ direction. The value of $7^0$ was chosen because that is how much the blade tip rotates in one time step. The obtained plots are depicted in Fig. 4.36. Tip vortices that contract inwards as they descend down are observed. Upto four discrete tip vortex cores are clearly visible. The present method, therefore, is capable of predicting the discrete and unsteady behavior of individual rotor blades and captures the resulting flowfield properties for a rotor in hover.

In Fig. 4.37, the pressure contours on the rotor disk plane for a collective pitch angle of $4.5^0$ are compared for the unsteady and steady rotors. As can be seen, unsteady rotor model applies a time dependent rotor source to a specific region of the rotor, as against the time-averaged sourcing of the steady rotor model. Fig. 4.38 depicts the vorticity magnitude for the same case. Discrete trailing vortices are observed for the unsteady rotor model simulation, showing the effect of discrete blades. This cannot be captured by the steady rotor model which shows a nearly uniform vorticity distribution along the rotor disk plane. It should be noted that these comparisons are qualitative and are not made to the same scale. Fig. 4.39 shows the wake for Rotor-II, with velocity magnitude as contours, and it is seen to be confined to the region below the rotor.

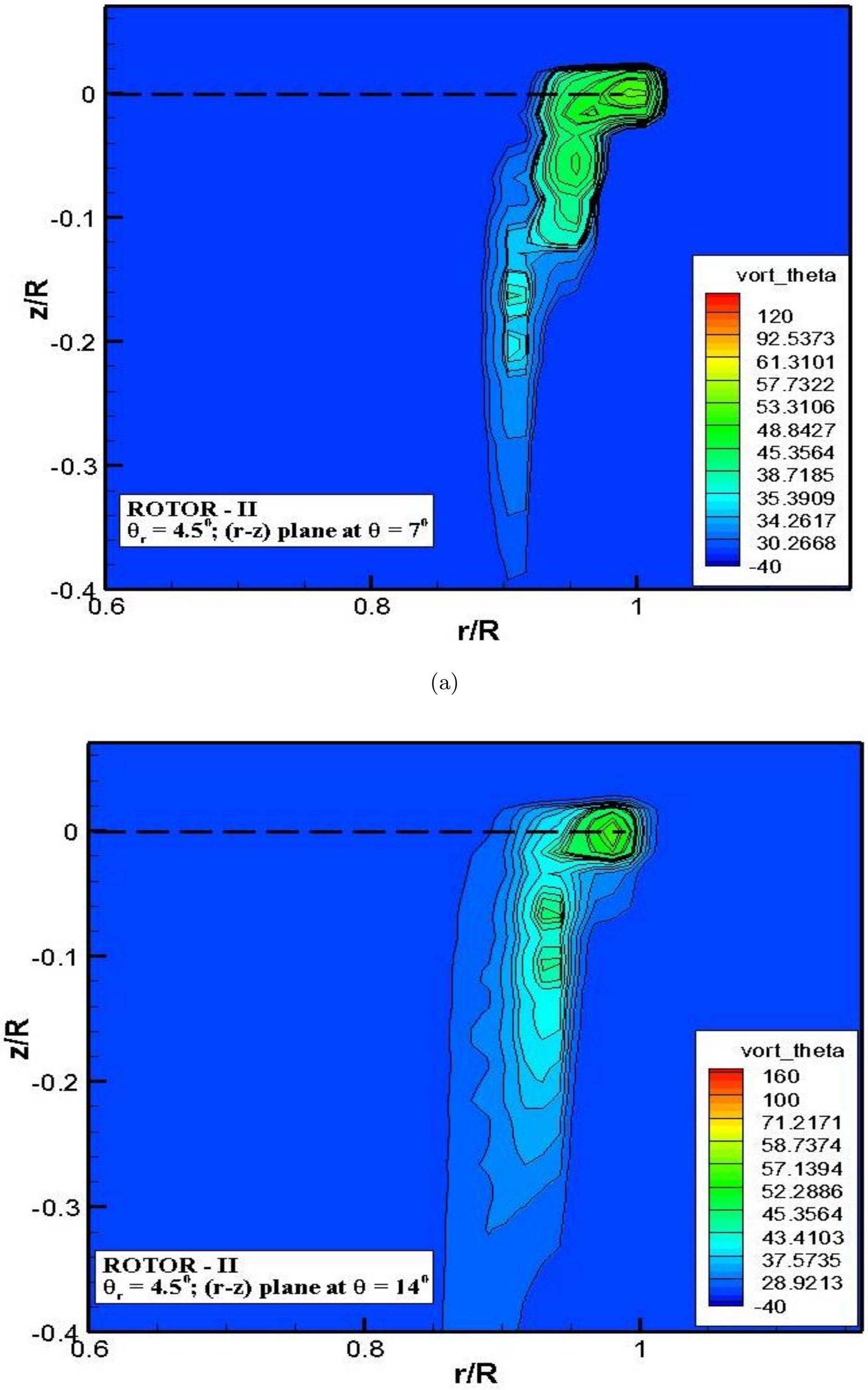

(a)

(b)

Figure 4.36 Vorticity contours in hover, Rotor - II

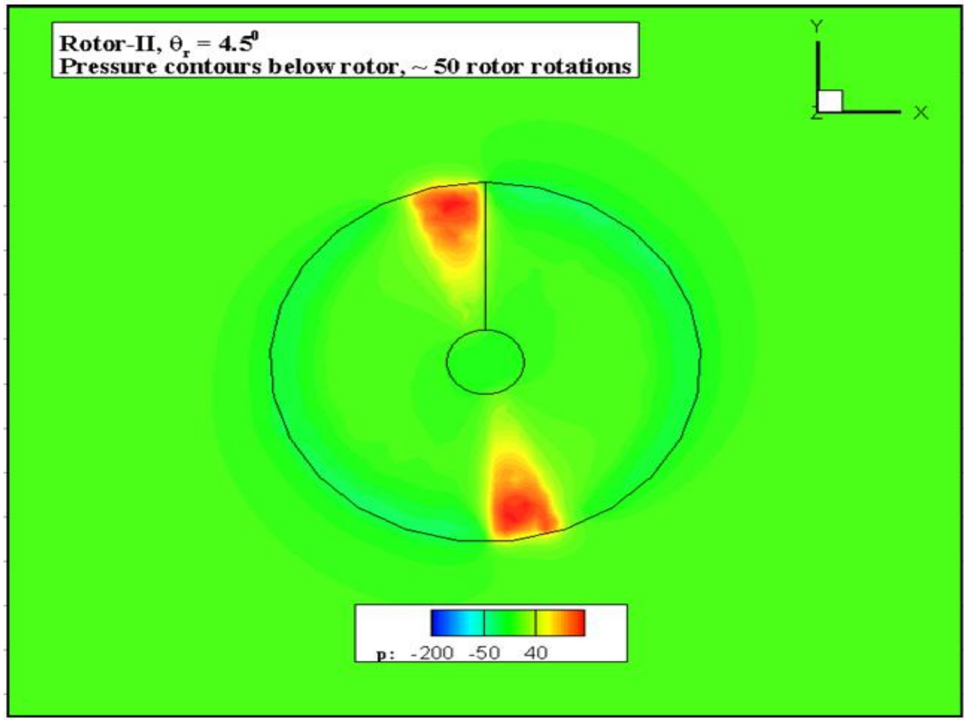

(a) Unsteady rotor model

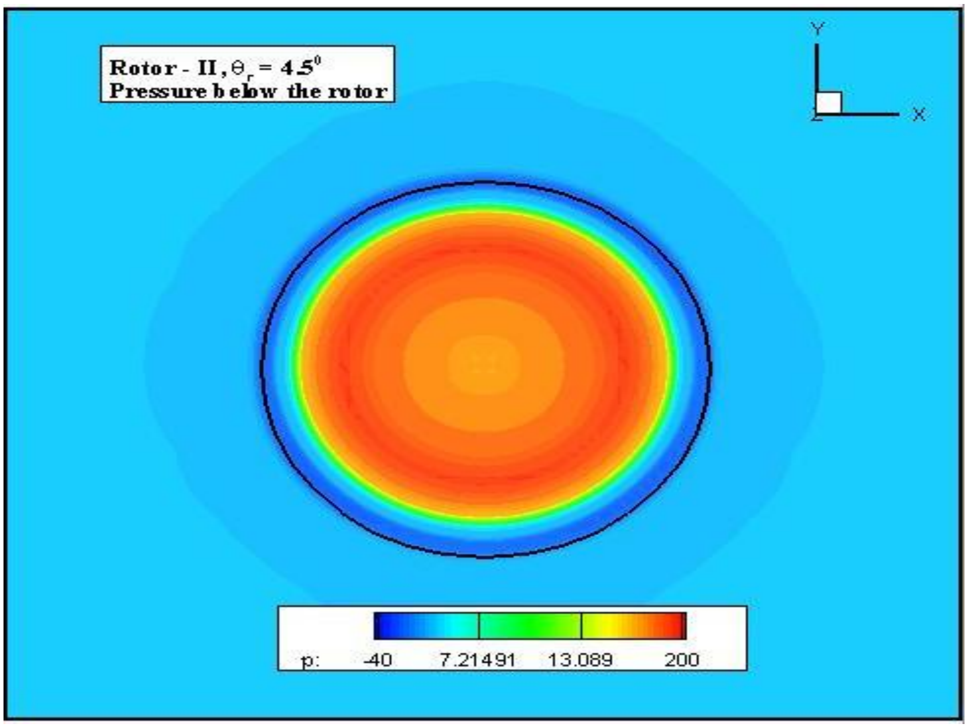

(b) Steady rotor model

Figure 4.37 Pressure contours below the rotor plane, Rotor - II

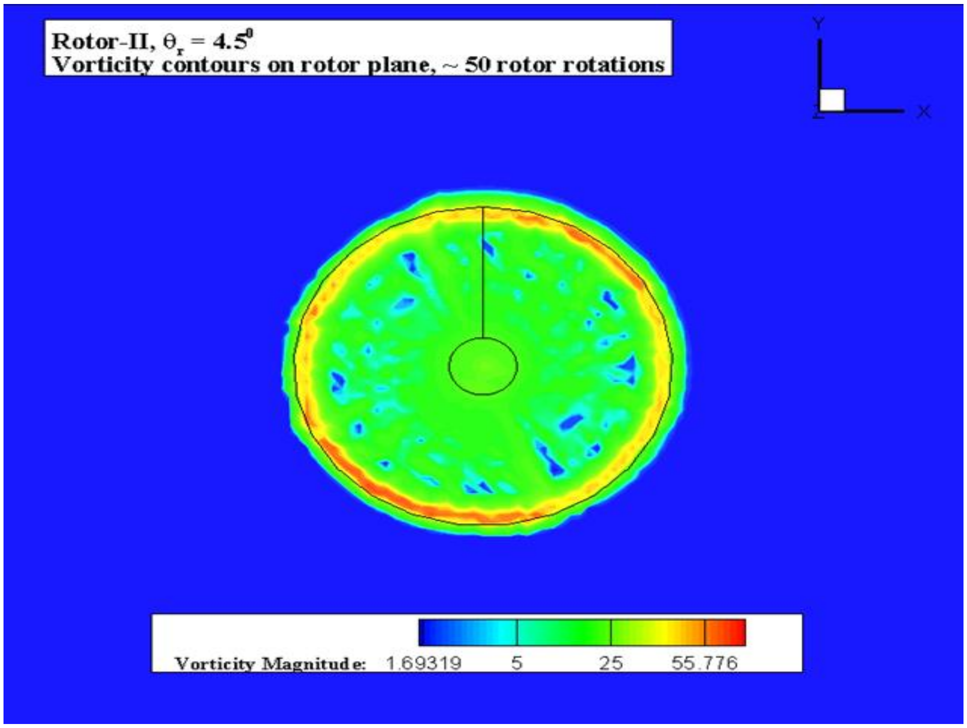

(a) Unsteady rotor model

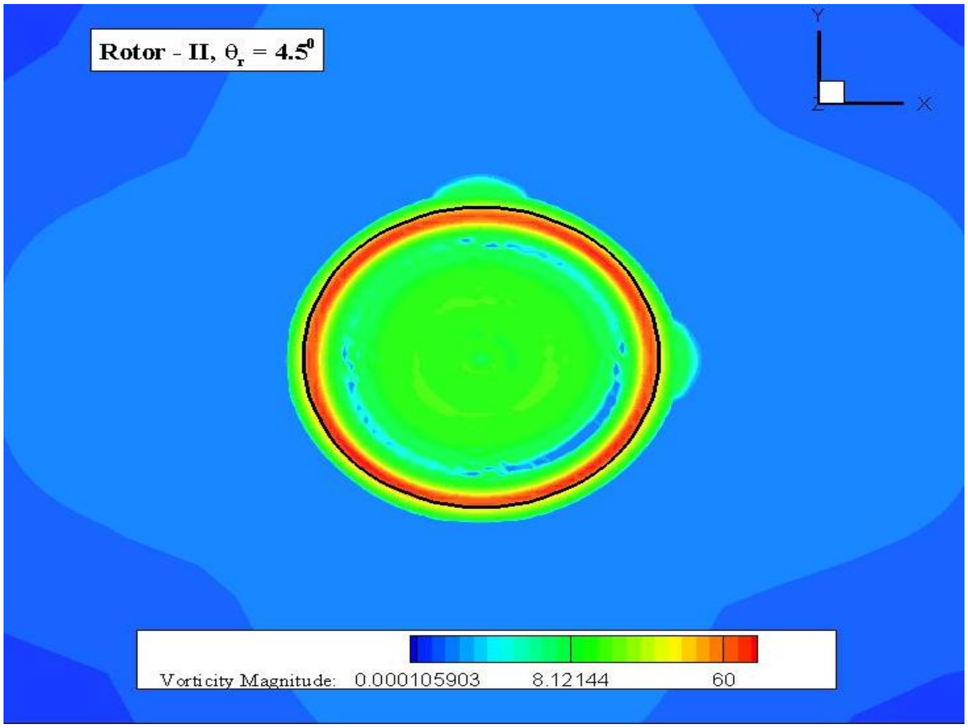

(b) Steady rotor model

Figure 4.38 Vorticity magnitude contours on the rotor plane, Rotor - II

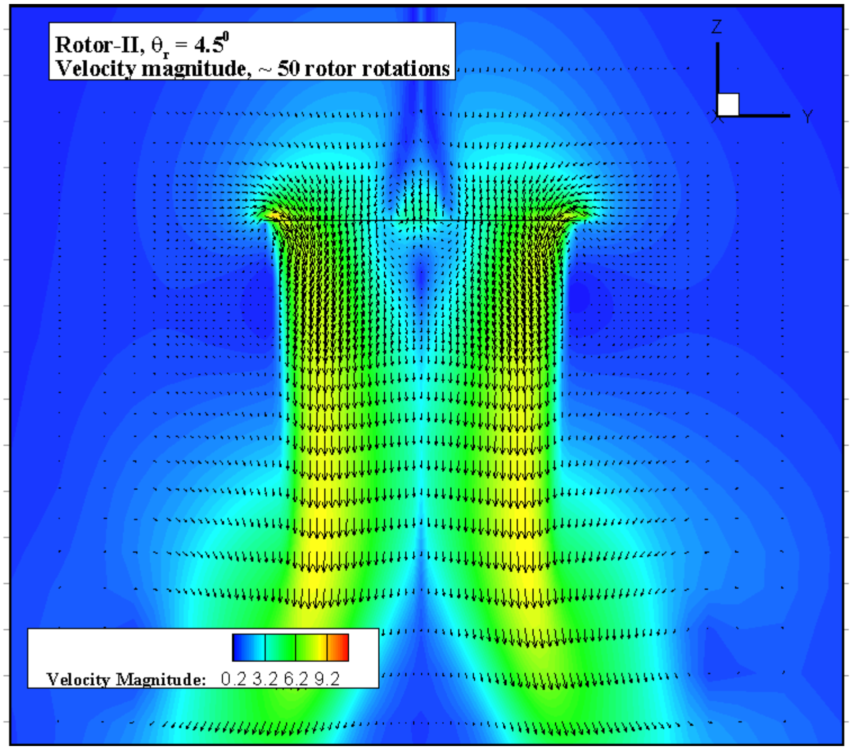

Figure 4.39 Velocity magnitude contours, $x$ plane passing through rotor center, Rotor - II

### 4.2.3 Case 3 : Light Rotor in Ground Effect

Hover performance of a helicopter rotor in ground effect (IGE) is an important design factor, the study of which can help in increasing the lifting capabilities of the helicopter rotor. Also, correctly determining the rotor flowfield characteristics when operating near the ground is crucial in the investigation of the Brownout phenomenon. In the present work, the experimental rotor by Light [52] was simulated in ground effect using the unsteady rotor model and the results are compared with experiments. Various rotor heights above the ground are simulated and the tip vortex geometries are presented. It must be noted here that the plots depicting the tip vortex location are extracted by tracing the '$\theta$' component of vorticity in the $(r - z)$ plane for $6^0$ increments in the rotor azimuth, going from $0^0 - 360^0$. This was done to match the semi-automated data reduction technique used in the experiments, which used shadowgraphs at $6^0$ intervals to trace the tip vortex.

Fig. 4.40 depicts the instantaneous '$\theta$' component of vorticity in the $(r - z)$ plane for given values of $\theta$ at different rotor/ground plane separation distances $(h/R)$. It can be seen that in the presence of the ground plane, the rotor wake contracts for a small distance and thereafter, it expands. This is unlike the out-of-ground effect (OGE) rotor wake which is known to contract well into the wake.

By taking the centers of the vortex cores as the location of the tip vortex at that instant in time, plots depicting the axial and radial tip vortex location for $h/R$ values of 0.84, 0.52 and 0.32 are presented in Figs. 4.41(a)-4.41(f). For a moderate value of $h/R = 0.84$ in Figs. 4.41(a) and 4.41(b), the wake is seen to contract for a small distance and then it gradually expands. The axial descent of the vortex core also decreases due to the presence of the ground plane. The wake expansion rate increases rapidly as the $h/R$ distance decreases in the subsequent plots. Fig. 4.42 shows a variation of the IGE/OGE rotor thrust for different $h/R$ values. All these results are seen to be in good agreement with the experimental data. The ability of the current unsteady rotor model in capturing discrete vortex cores and in correctly predicting the rotor flow field in ground effect makes it a good model to be used for the study of rotorcraft Brownout and also for designing high lift rotors.

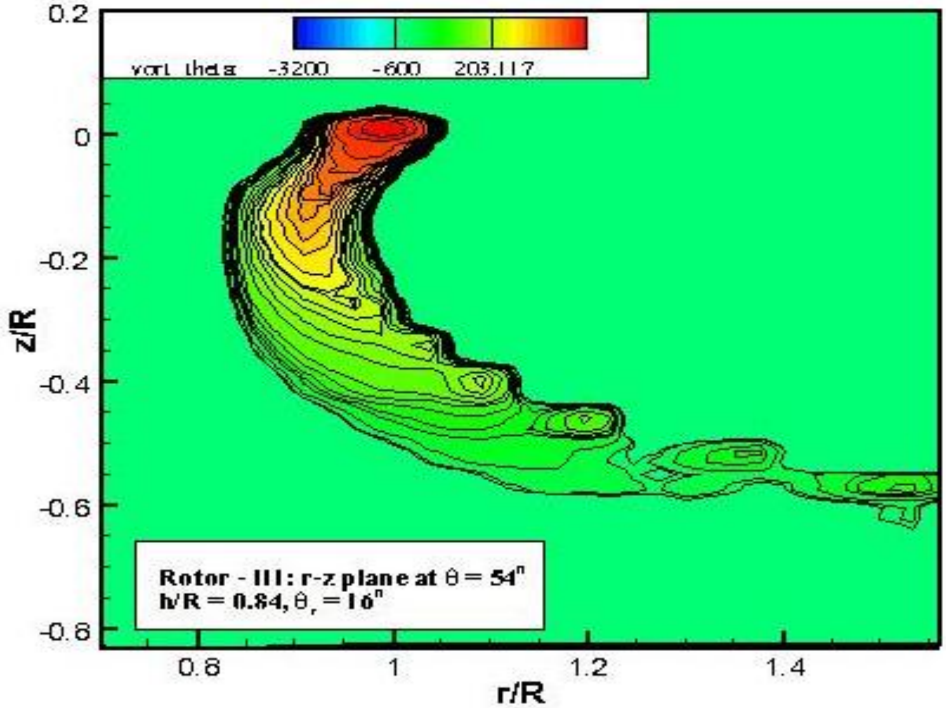

(a) $h/R = 0.84$

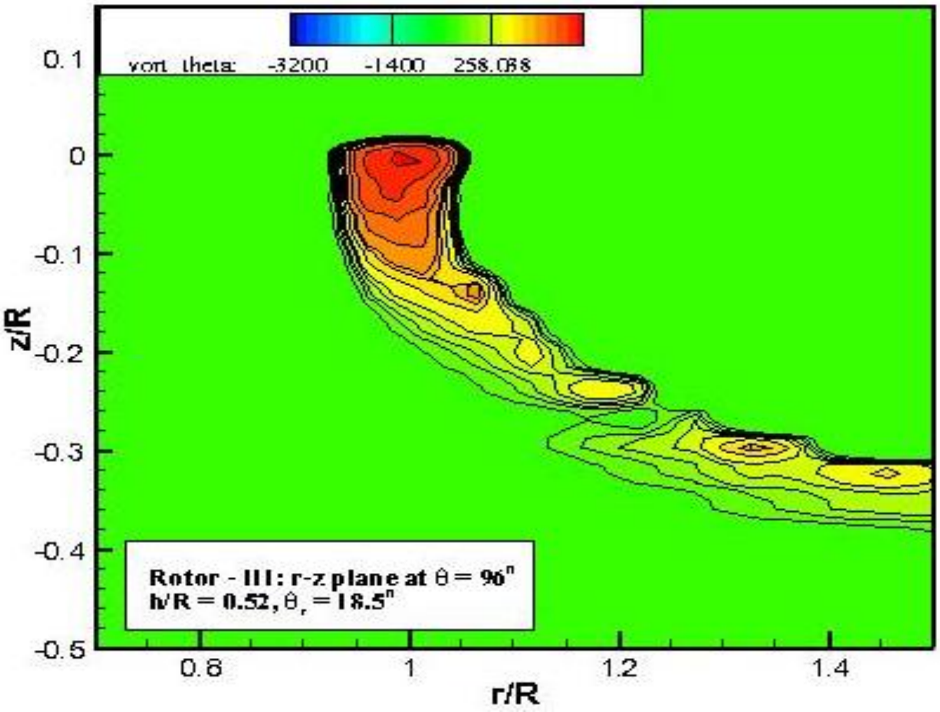

(b) $h/R = 0.52$

Figure 4.40 Vorticity contours in $r - z$ plane, Rotor - III

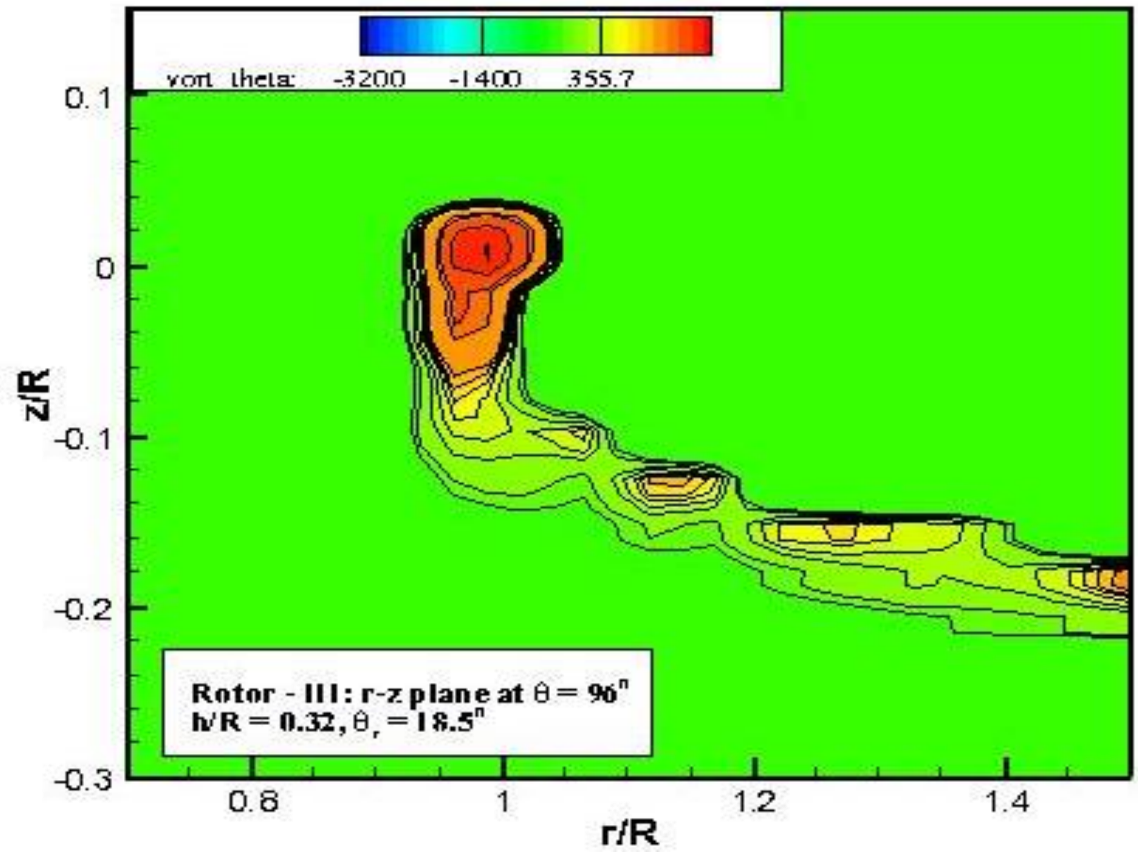

(c) $h/R = 0.32$

Figure 4.40 (continued) Vorticity contours in $r - z$ plane, Rotor - III

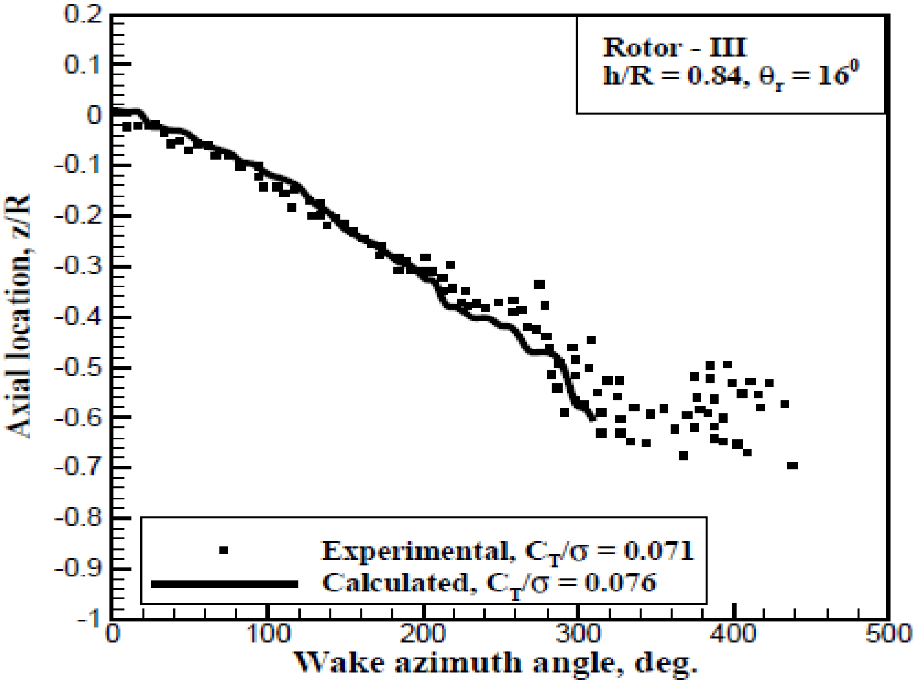

(a) Axial vortex location, $h/R = 0.84$

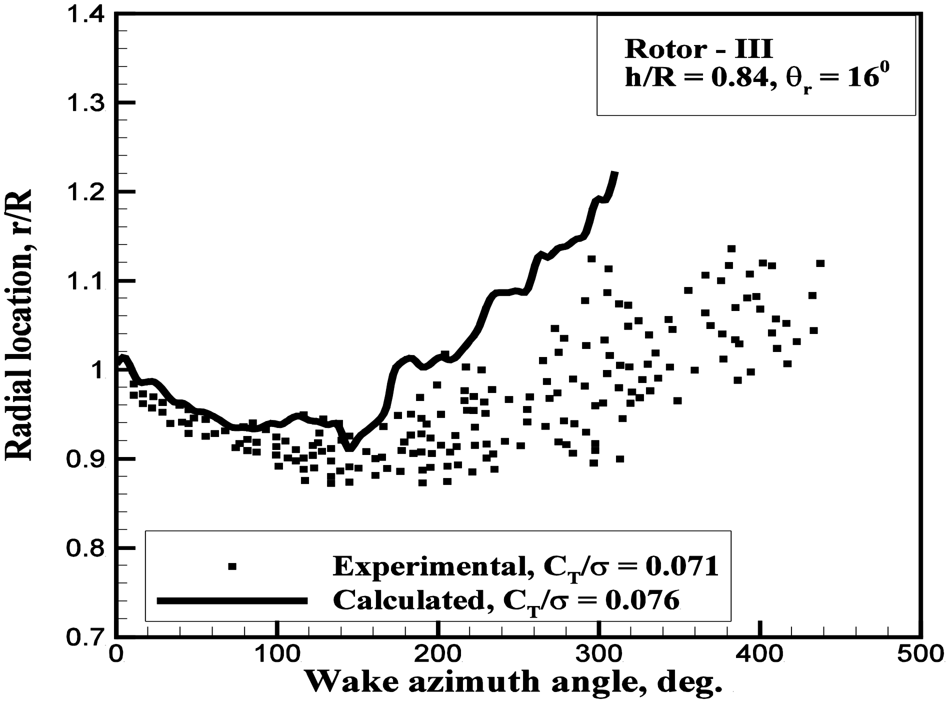

(b) Radial vortex location $h/R = 0.84$

Figure 4.41 Tip vortex locations, Rotor - III

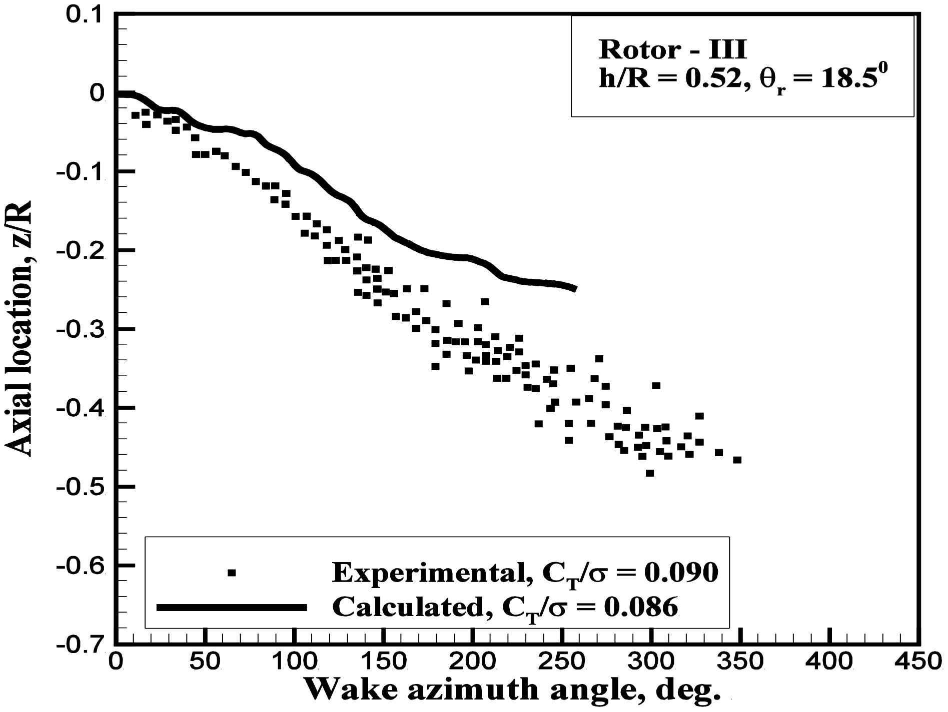

(c) Axial vortex location, $h/R = 0.52$

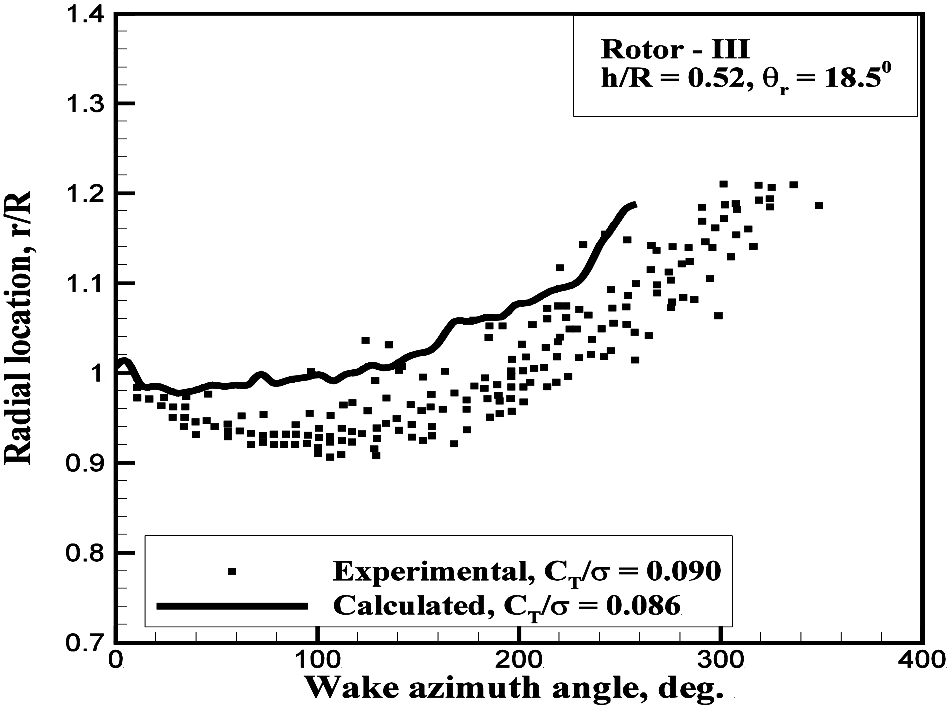

(d) Radial vortex location $h/R = 0.52$

Figure 4.41 (continued) Tip vortex locations, Rotor - III

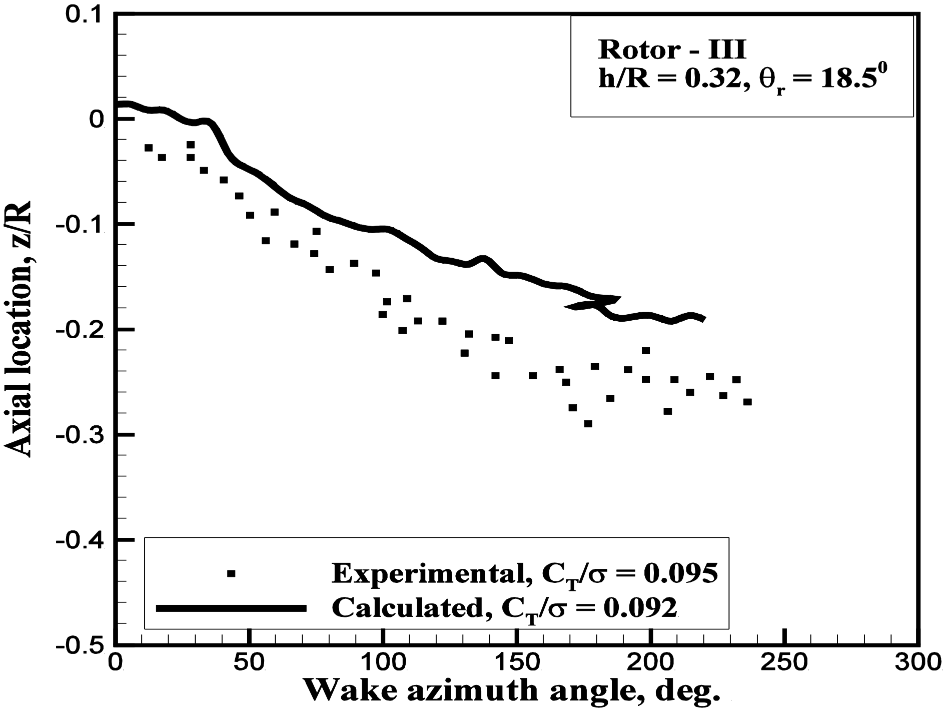

(e) Axial vortex location, $h/R = 0.32$

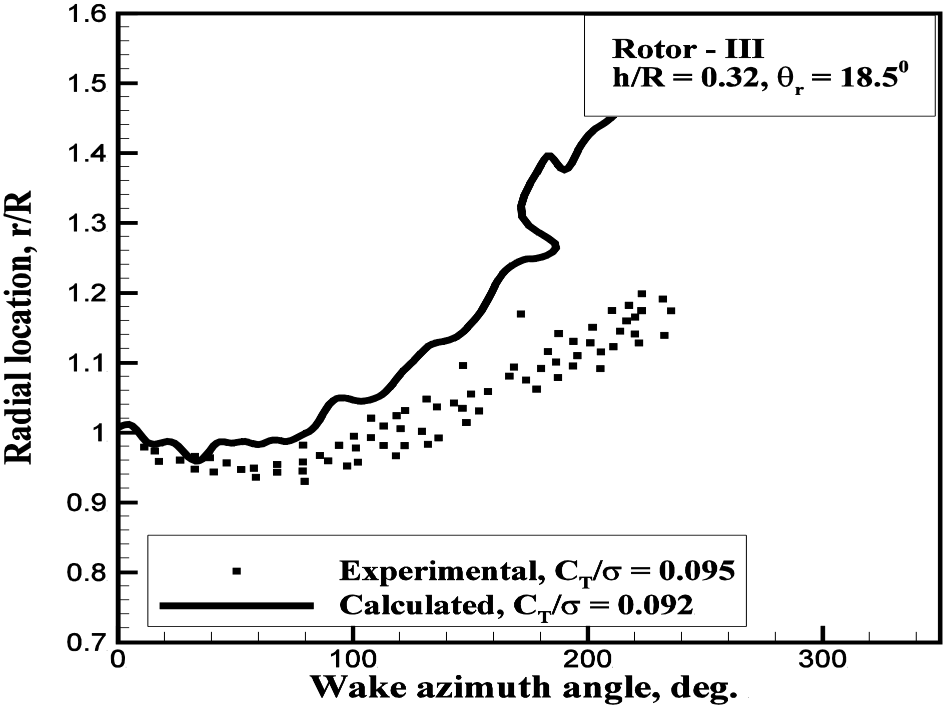

(f) Radial vortex location $h/R = 0.32$

Figure 4.41 (continued) Tip vortex locations, Rotor - III

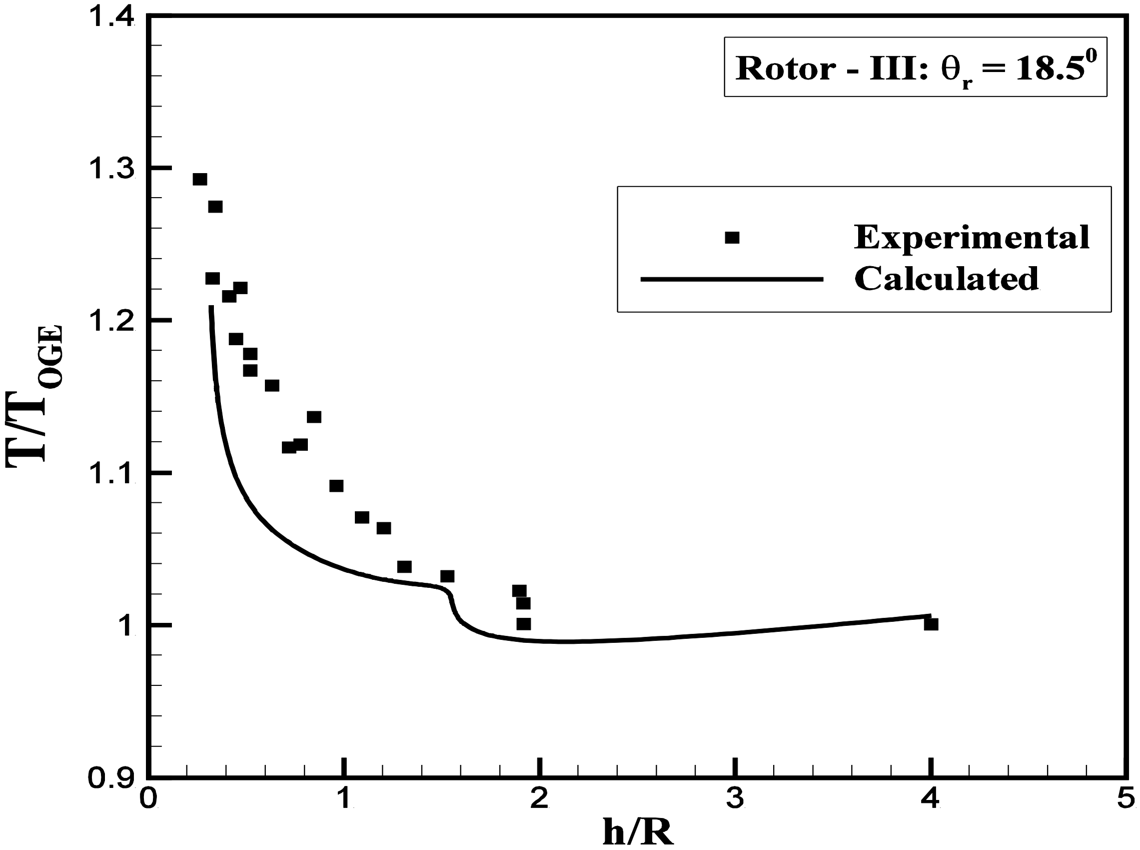

Figure 4.42 Comparison of measured and predicted thrust in ground effect, Rotor - III

## 4.3 Unsteady rotor with Unstructured Solver

The previous two sections presented validation results for the unstructured solver and the unsteady rotor independently. In this section, results for the unsteady rotor model coupled with the unstructured solver are presented. Model helicopter rotors in hover, Rotor I and II as described in the previous section, are chosen for this purpose. Wherever possible, results are compared to experiments and also to the structured unsteady rotor results.

At this point, a brief discussion on the computational requirements for the unstructured solver is in order. The grid generation process used in this research generates tetrahedrons by dividing each structured hexahedron into 6 tetrahedrons. The six faces of a hexahedron are split to generated 16 tetrahedral faces. Since the current solution algorithm uses a face based data structure, where all coefficients are computed and assembled by looping over the faces, the increase in number of faces results in increased computational time and memory requirements. For example, let us start from a structured grid with 27 nodes and tessellate the same physical space to generate tetrahedrons. A comparison of the number of faces and cells is shown in Table 4.3

Table 4.3 Grid Metrics

| | Nodes | Faces | Cells |
|---|---|---|---|
| Structured | 27 | 32 | 8 |
| Unstructured | 27 | 120 | 48 |

Hence, the domain size and the grid resolution used for simulating the unsteady rotor model with the unstructured solver were limited to 10 radii wide in all directions, with 9000-20000 grid points. In the following subsections, results for the Caradonna rotor (Rotor - I) and the Rabbot rotor (Rotor - II) are presented. These results were obtained using a grid with 9261 grid points and the grid is shown in Fig. 4.43.

### 4.3.1 Case 1 : Caradonna Rotor

A collective pitch of $12^0$ was simulated for Rotor - I on a grid having 9261 grid points. The time step was set at 0.0015. The variation of coefficient of thrust with time is shown in

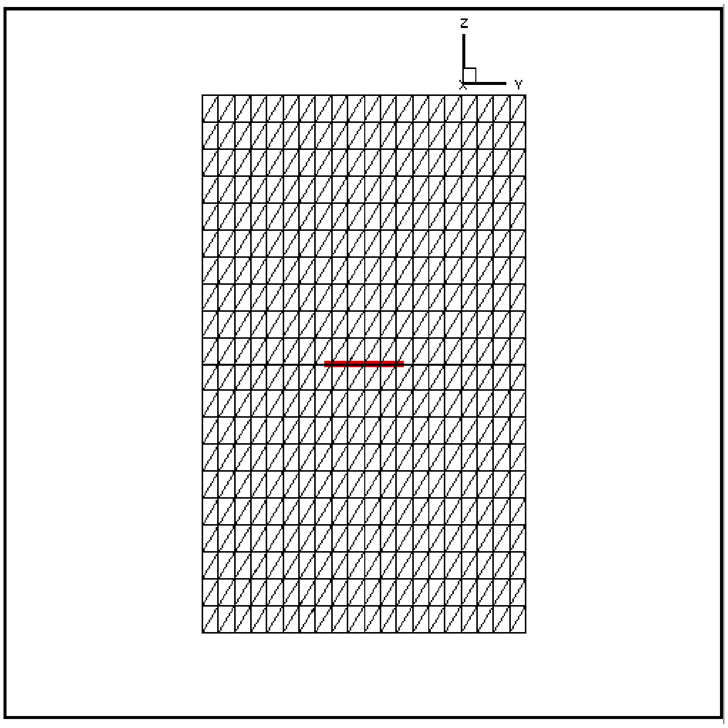

Figure 4.43 Unstructured grid for unsteady rotor calculations

Fig. 4.44. It can be seen that the unstructured solver with the unsteady rotor shows a similar $C_T$ behavior as the structured solver. The unsteadiness of a rotor flow is well manifested in the time dependent oscillations observed in this plot. In order to validate the performance of the unstructured solver with the unsteady rotor model, a similar simulation was run with the structured solver, using the same domain size and grid resolution. Fig. 4.45 compares the time history of $C_T$ for the two solutions. It can be seen that for the given grid resolution, the unstructured code matches the structured results. The oscillations in $C_T$ are also seen to be periodic with time. Table 4.4 compares the predicted values of $C_T$ and $C_Q$ for the unstructured and structured codes with the experiment. The overprediction of the $C_T$ value is attributed to the coarser grid resolution. However, a good agreement between the unstructured code and the well-validated structured code for the given conditions is observed. Fig. 4.46 shows the velocity vectors near the rotor plane.

Table 4.4 Performance Comparison, Rotor - I

| | $C_T$ | $C_Q$ |
|---|---|---|
| Structured | 0.00814 | 0.000818 |
| Unstructured | 0.00823 | 0.000791 |
| Experiment | 0.0079 | - |

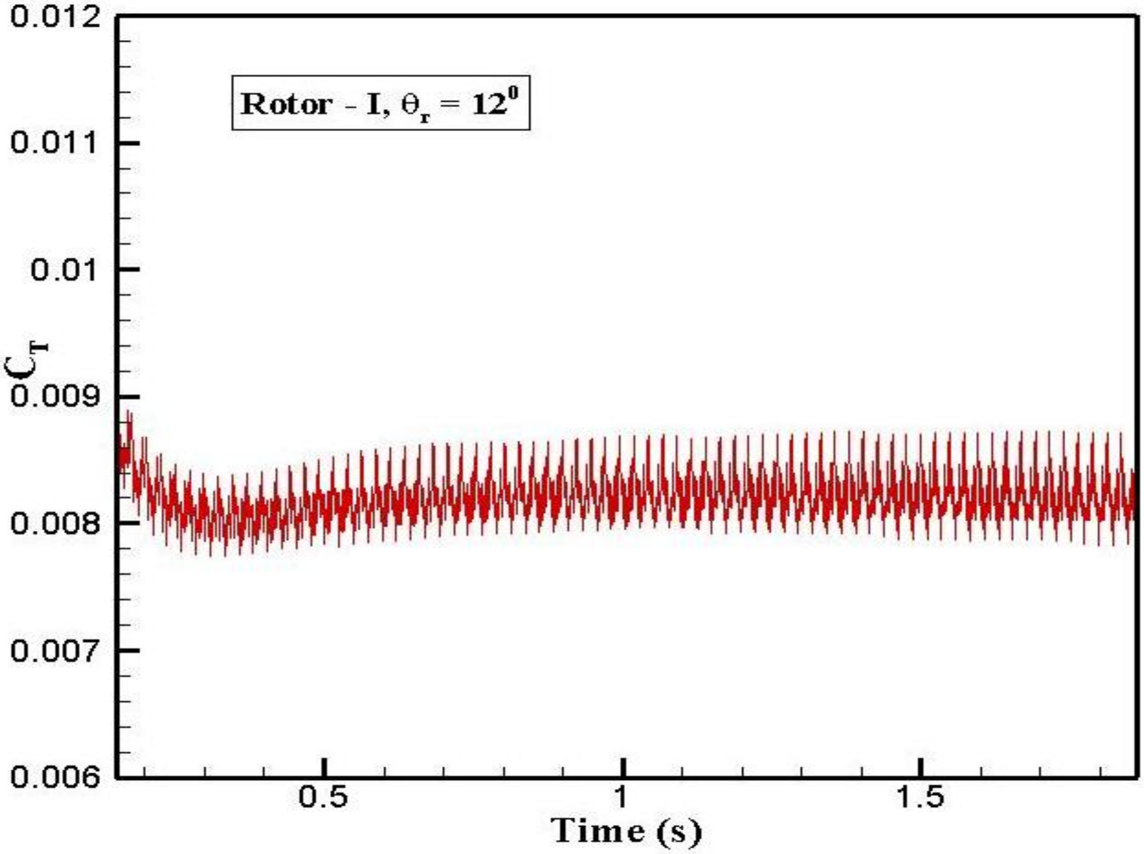

Figure 4.44 Unstructured solver with unsteady rotor, $C_T$ vs. time, Rotor - I

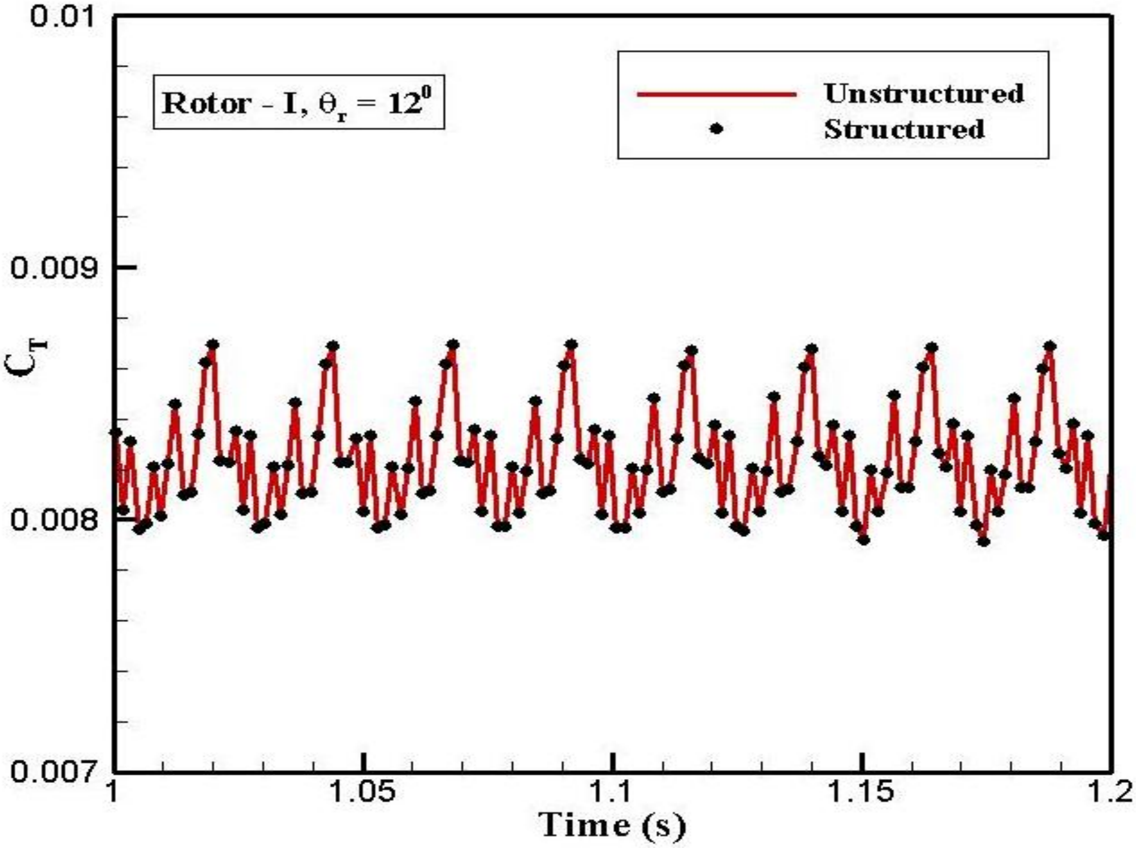

Figure 4.45 Comparison of $C_T$, Rotor - I

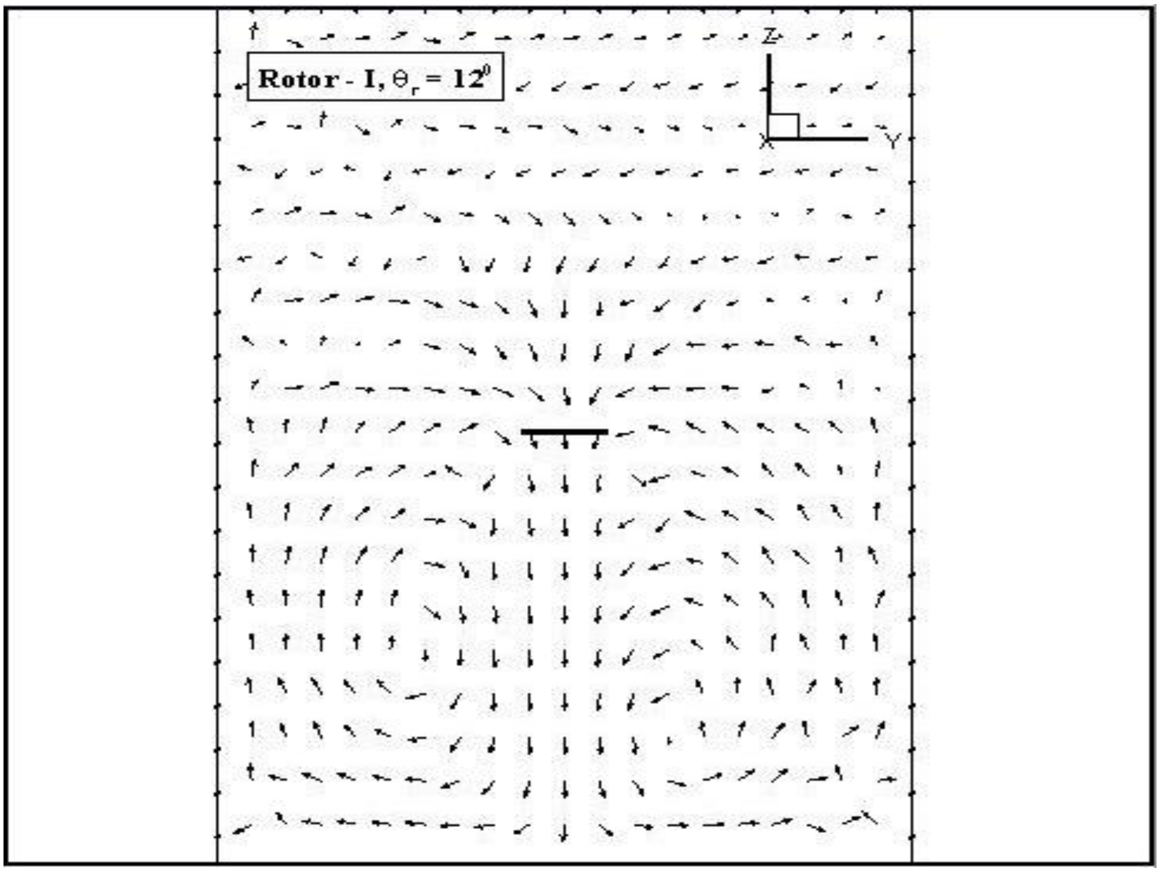

Figure 4.46    Velocity vectors, Rotor - I

### 4.3.2 Case 2 : Rabbot Rotor

For the Rabbot rotor i.e. Rotor - II, a range of collective pitch angles was simulated with the unstructured solver and unsteady rotor model. Fig. 4.47 shows the time variation of $C_T$ for a collective pitch angle of $4.5^0$. As can be seen, the expected unsteady behavior is observed. The calculated average value of $C_T$ (averaged over 50 rotor rotations) is within 2% of the experimental value. The better $C_T$ prediction for the Rabbot case, as compared to the Caradonna rotor, is attributed to the higher grid resolution along the rotor radius, resulting in more continuous rotor source distribution. Fig. 4.48 compares the time variation of $C_T$ as predicted by the structured and unstructured solvers, showing a good agreement between the two. Table 4.5 compares the calculated performance for different collective pitch angles.

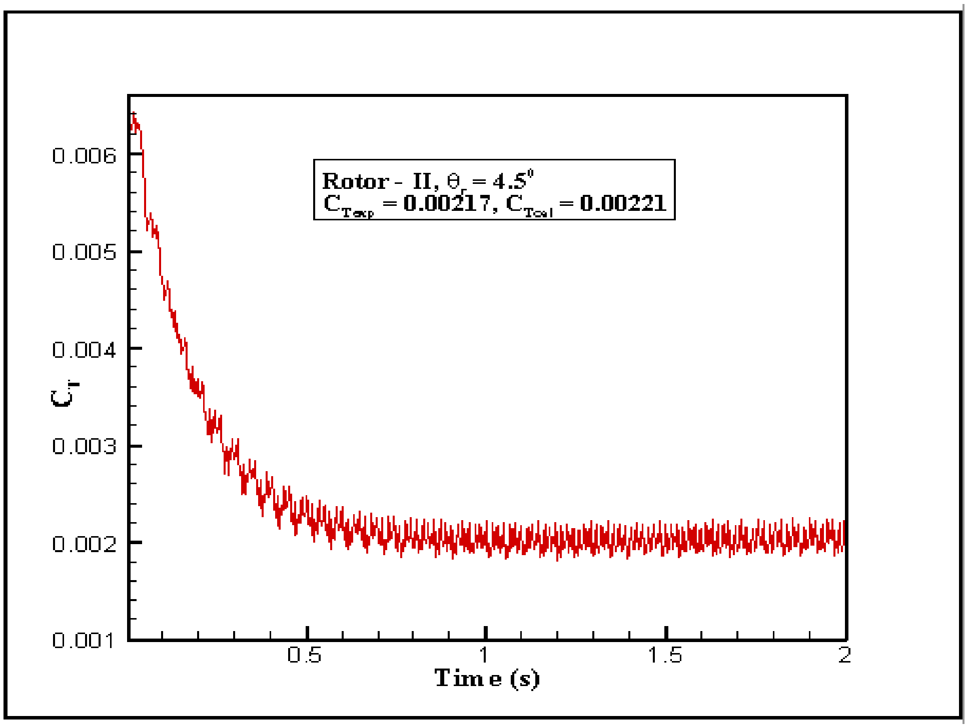

Figure 4.47 Unstructured solver with unsteady rotor, $C_T$ vs. time, Rotor - II

Fig. 4.49 depicts the radial aerodynamic loading for different collective pitch angles. A good agreement with the experiment as well as with the structured code is observed in these plots, except at the outboard region where the loading does not approach zero. This is due to the absence of any tip correction technique in the unstructured unsteady rotor code.

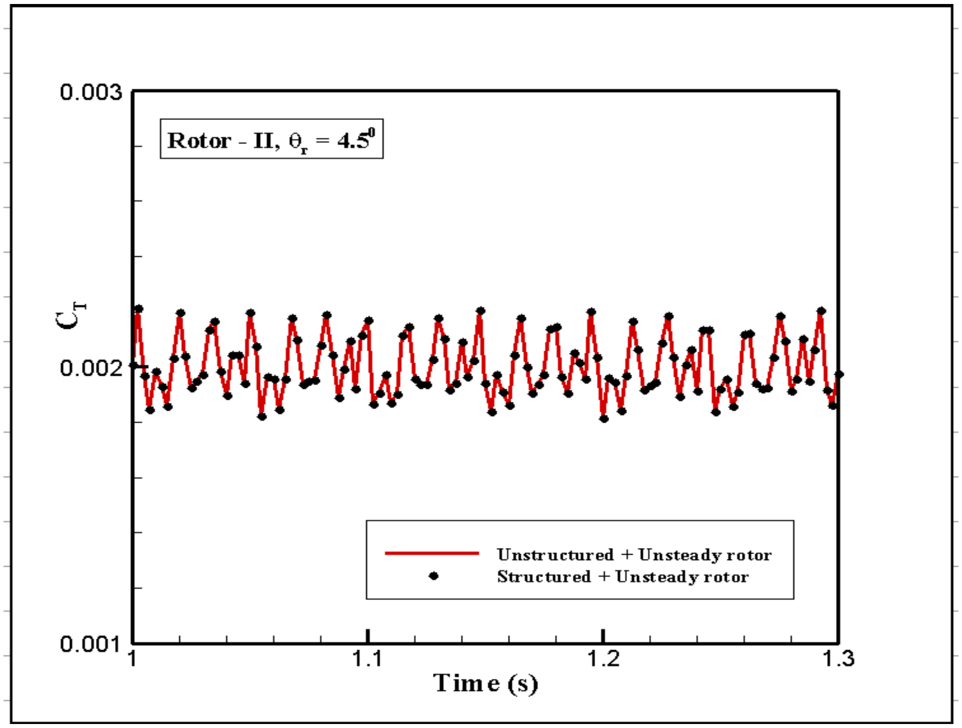

Figure 4.48 Comparison of $C_T$, Rotor - II

Table 4.5 Performance comparison

| Collective pitch | Experimental $C_T$ | Unstructured $C_T$ | Structured $C_T$ |
|---|---|---|---|
| $3^0$ | 0.00148 | 0.001216 | 0.00107 |
| $4.5^0$ | 0.00217 | 0.00221 | 0.00186 |
| $6.7^0$ | 0.00334 | 0.00370 | 0.00310 |
| $9.2^0$ | 0.00518 | 0.00578 | 0.00507 |

As was discussed earlier, Figure of Merit is an important parameter for a hovering rotor and it should follow a nearly linear trend with the thrust coefficient. A similar study, as was done for the structured unsteady rotor solver, was conducted with the unstructured solver and the results are presented in Fig. 4.50. An overall good agreement with experiments is observed in these plots. The unsteady rotor model is therefore, capable of predicting the performance of a rotor flow in an unstructured framework.

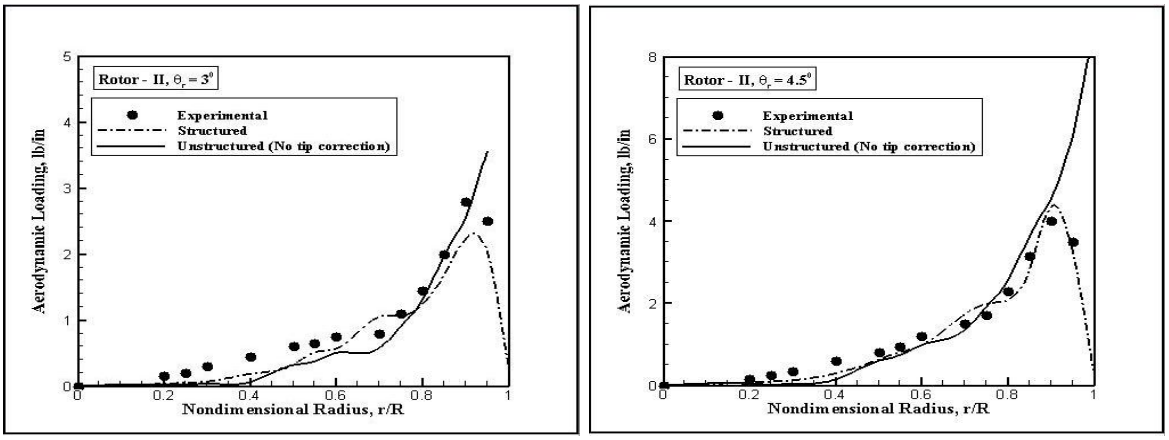

(a) $\theta_c = 3^0$

(b) $\theta_c = 4.5^0$

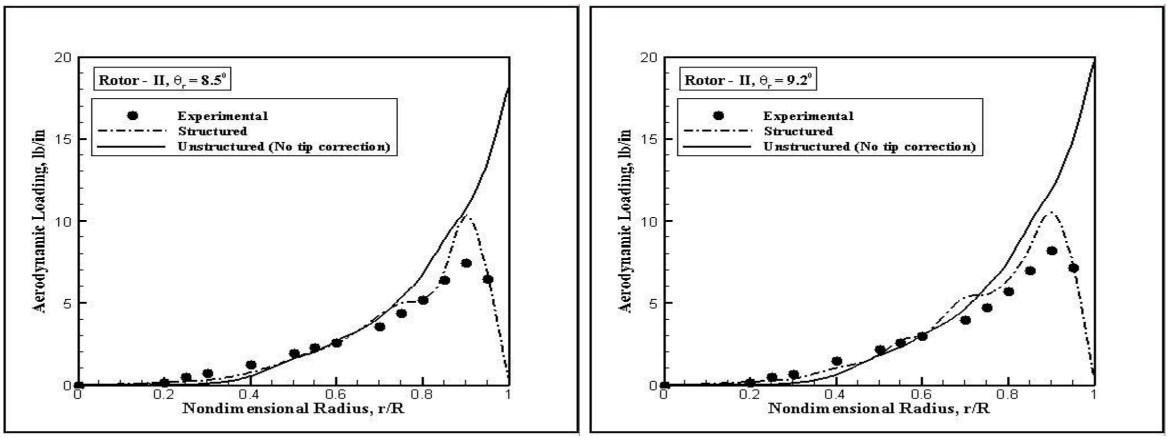

(c) $\theta_c = 8.5^0$

(d) $\theta_c = 9.2^0$

Figure 4.49 Spanwise aerodynamic loading with Unstructured-unsteady rotor model, Rotor - II

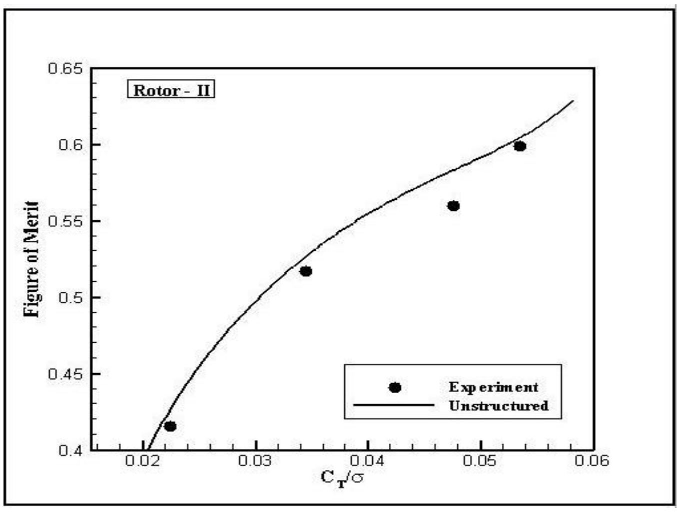

(a) Correlation of FM and thrust coefficient

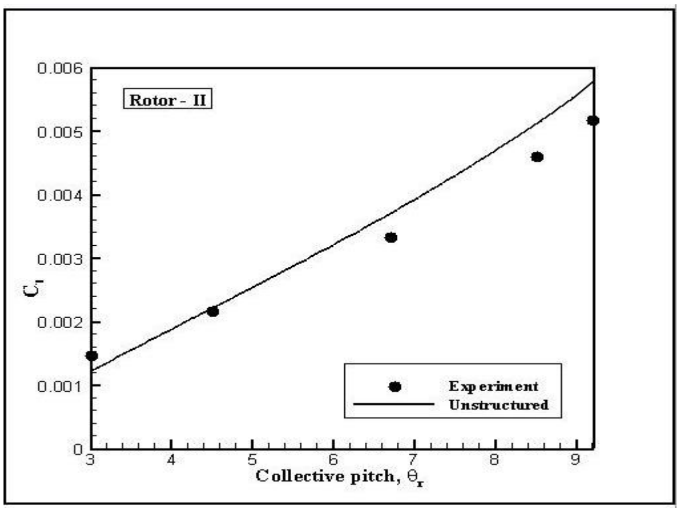

(b) Effect of collective pitch on $C_T$

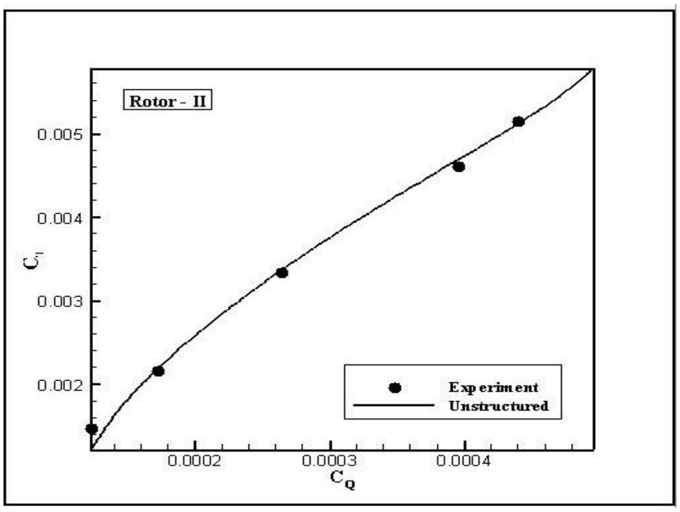

(c) Correlation of rotor thrust and torque

Figure 4.50 Performance characteristics, Rotor - II

Next, the flowfield characteristics as predicted by the unstructured unsteady rotor solver are presented. Fig. 4.51 shows the instantaneous pressure contours above and below the rotor for a collective pitch angle of $4.5^0$. The expected pressure differential across the rotor is observed, thereby maintaining the correct physics of a rotor flow. Also, the localized pressure distribution is an artifact of the unsteady rotor source, as against time-averaged steady rotor source. Fig. 4.52 shows the velocity and vorticity magnitude contours on the rotor plane, while Fig. 4.53 depicts the instantaneous rotor wake. It has already been established in previous sections that the unsteady rotor modeling technique captures discrete tip vortices and the unsteady wake of a rotor flow. For the unstructured unsteady rotor results, the unsteady effect of discrete blades is apparent in the pressure distribution and rotor plane flow plots, but not in the cross-plane view of the rotor wake. This is due to inadequate grid resolution in the wake region of the rotor. Suitable grid adaptation of the unstructured grid is necessary to take full advantage of the unsteady rotor modeling technique.

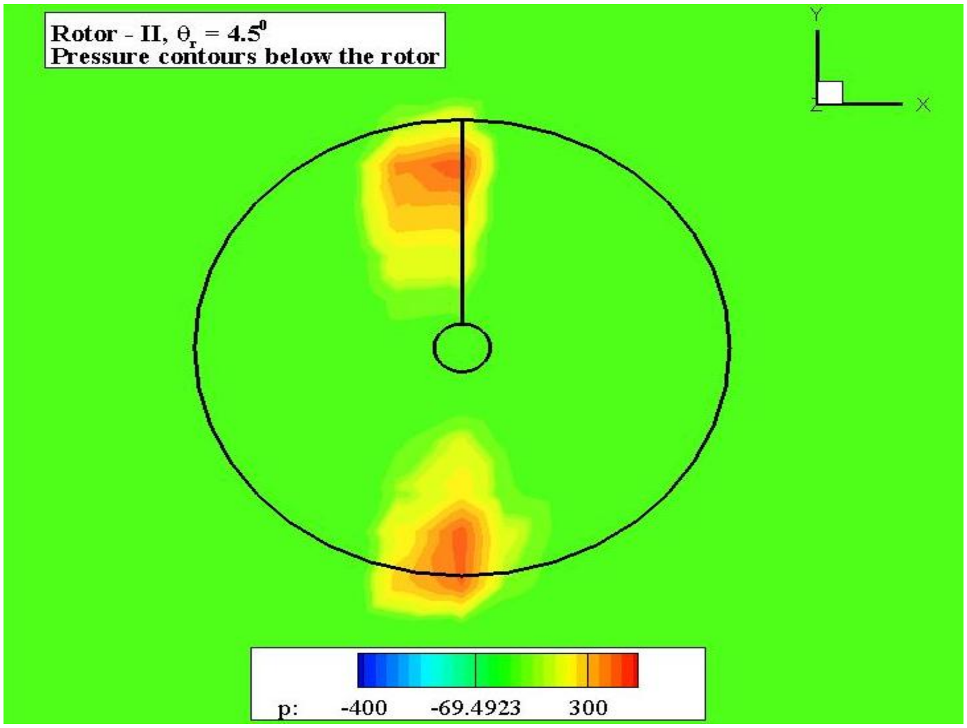

(a) Below the rotor

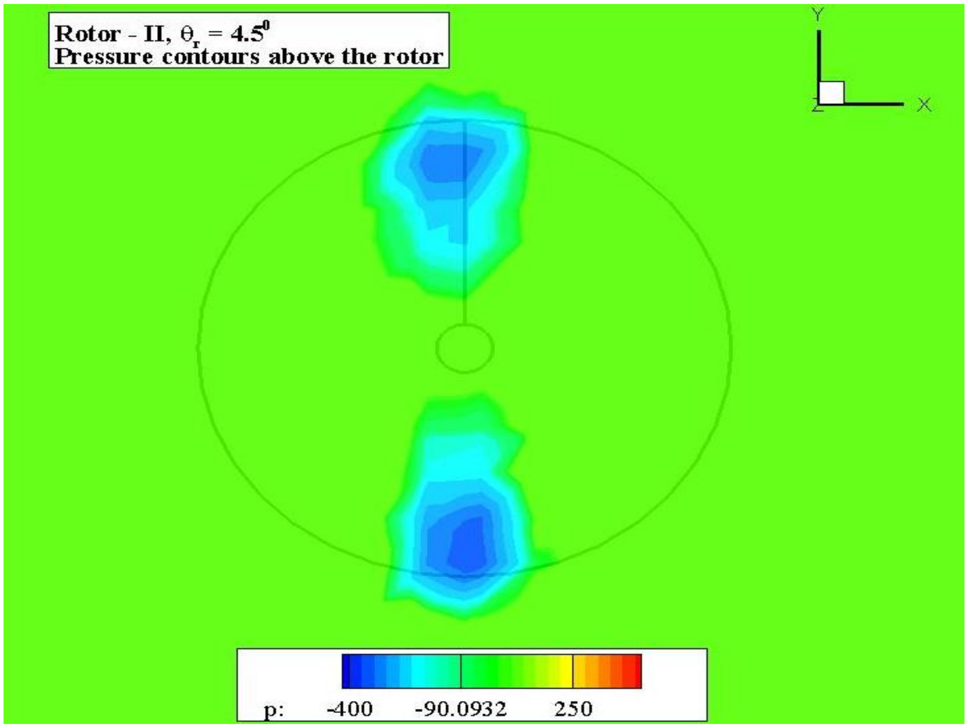

(b) Above the rotor

Figure 4.51 Instantaneous pressure contours, Rotor - II

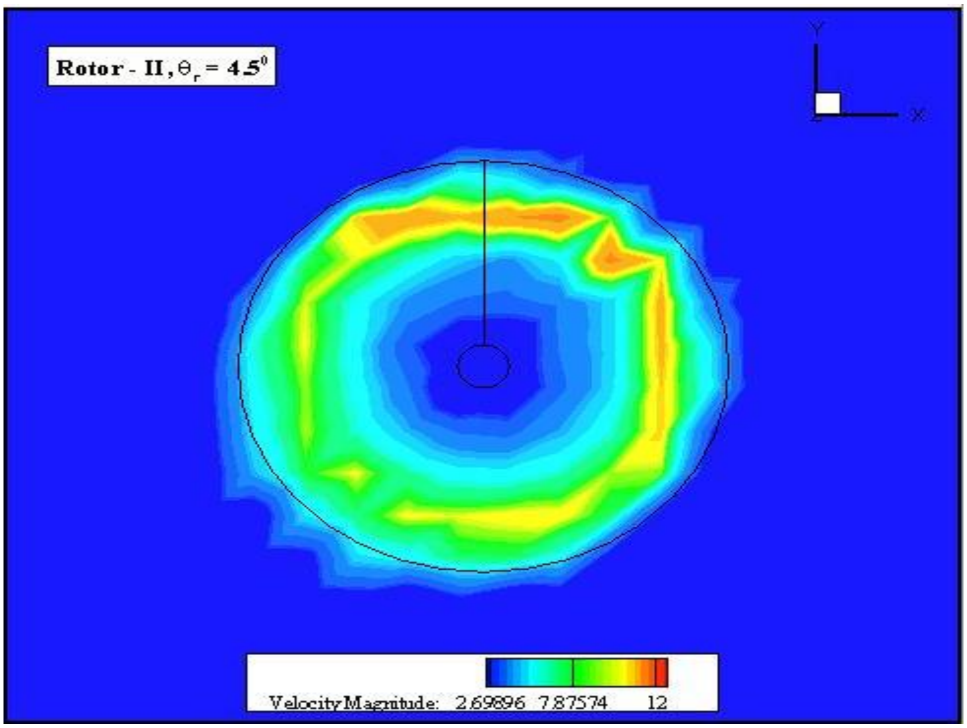

(a) Velocity contours

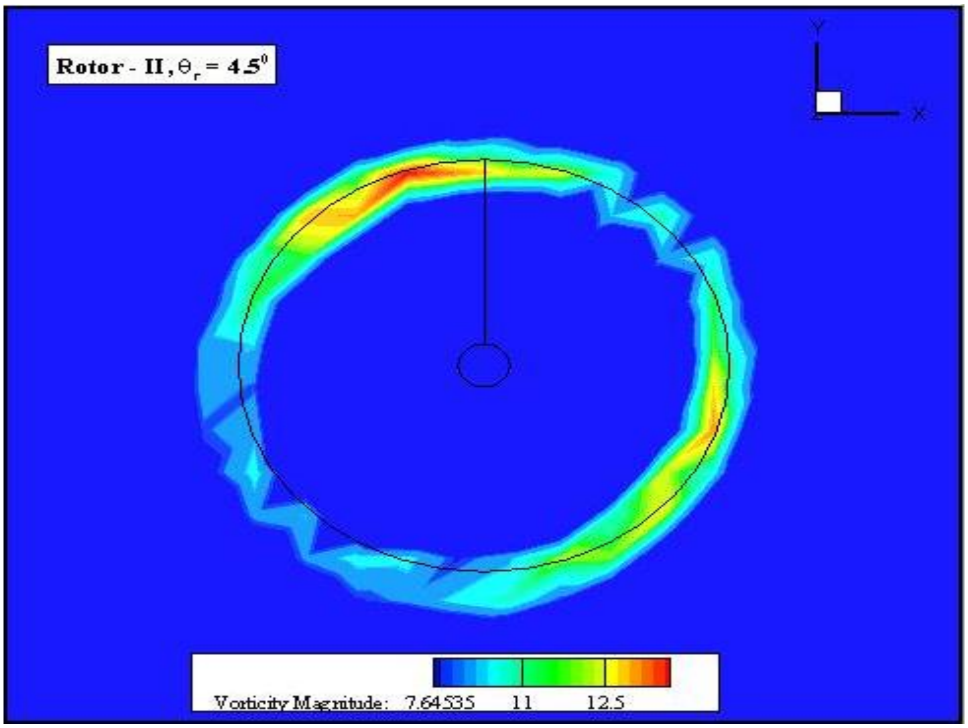

(b) Vorticity contours

Figure 4.52 Rotor - II

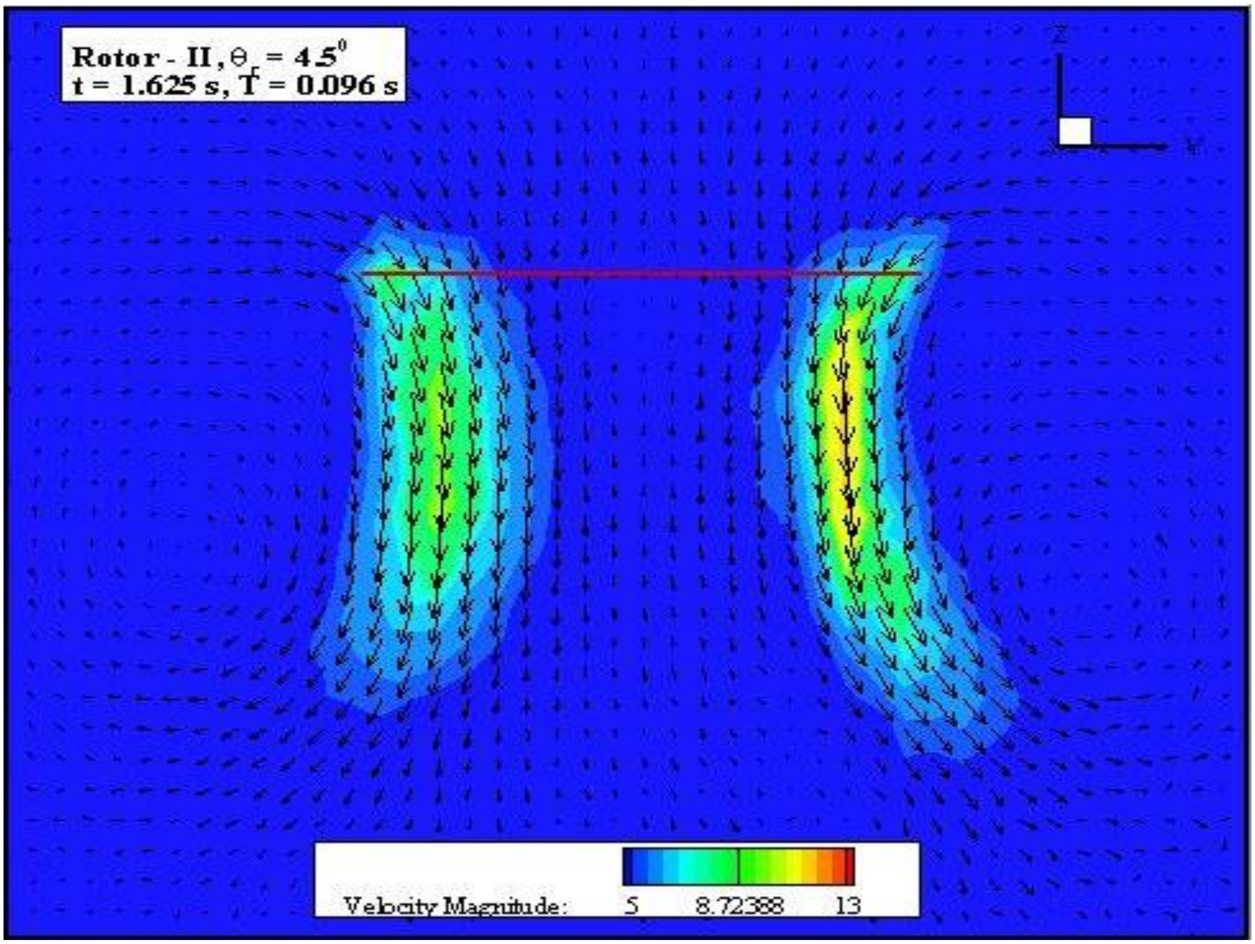

Figure 4.53 Velocity vectors, Rotor - II

# CHAPTER 5. CONCLUDING REMARKS AND RECOMMENDATIONS

In the current research, an unstructured, time-accurate methodology for rotorcraft flows was presented. The incompressible, unsteady, three-dimensional Navier-Stokes equations were solved in the primitive variable formulation, using a median-dual based control volume method. Tetrahedral grids, generated by tessellating structured hexahedral grids, were used for discretizing the physical domain. A vertex-centered finite volume discretization with median-dual control volumes was used in the present research, where pressure velocity coupling was achieved by employing an artificial velocity field to satisfy the continuity constraint. The resulting discretized equations were solved using the SIMPLER algorithm. An implicit time integration scheme was used for advancing in time. The unstructured flow solver was validated using the confined flow in a cavity problem. Both a constant velocity lid and oscillating lid driven cavity problems were tested. A good agreement with existing numerical data was observed. It was found that the flow solver is capable of capturing the unsteady, three-dimensional effects observed in such flows and with adequate grid resolution, also captures the transient vortex development for different Reynolds number.

In addition to the unstructured flow solver, a novel unsteady rotor modeling technique, based on the momentum source approach, was also developed. The unsteady rotor model was first validated by implementing it in an existing three-dimensional, Cartesian structured code for hovering rotors in and out of ground effect. It was found that the unsteady rotor model is capable of capturing the discrete effects of rotor blades like blade tip vortices and results in a time-accurate rotor flowfield. The model also furnishes a good prediction of the performance characteristics of hovering rotors. The unsteady loading on the rotor blades was calculated and an overall good agreement with experiments was observed. The unsteady rotor model was integrated with the unstructured flow solver and simulations for rotors in hover were conducted.

Even with limitations on unstructured grid size, the unstructured-unsteady rotor model was found to furnish a good approximation of the performance characteristics and loading on a hovering rotor. The unsteady, discrete blade effects were observed on the rotor plane, but due to coarser grid resolution (a limitation of the computer memory), they could not be preserved in the rotor wake.

Although the current research is promising, future efforts are required to make the unstructured-unsteady rotor model more robust and general. The unstructured flow solver needs to be tested for more external flows and following that, the unstructured-unsteady rotor model can be applied to problems like rotor-fuselage configurations. There will always be an overhead in going from a structured to an unstructured grid approach, in terms of memory and flow solver complexity. But the ease in generating body-conforming grids for complex geometries, with the potential for localized grid refinement, makes unstructured grid approaches worth the effort. The idea of using the unstructured-unsteady rotor solver near the rotor-body configuration and coupling it with a Cartesian unstructured grid in the farfield, resulting in a hybrid solver, should be explored further.

# APPENDIX A. Interpolation Function for a General Variable $\Phi$

Given the interpolation function as $\Phi = A\xi + BY + CZ + D$, the coefficients $A, B, C$ and $D$ can be computed by satisfying the equation on the four node points of a tetrahedron. The system of equation in the four unknowns, thus generated is:

$$A\xi_1 + BY_1 + CZ_1 + D = \Phi_1$$

$$A\xi_2 + BY_2 + CZ_2 + D = \Phi_2$$

$$A\xi_3 + BY_3 + CZ_3 + D = \Phi_3$$

$$A\xi_4 + BY_4 + CZ_4 + D = \Phi_4 \tag{A.1}$$

This formulation is in terms of the local coordinate system $(\xi, Y, Z)$. Solving the above system of equations by Cramer's rule, the unknowns can be cast as follows:

$$A = L_1\Phi_1 + L_2\Phi_2 + L_3\Phi_3 + L_4\Phi_4 = \sum_{i=1}^{4} L_i\Phi_i$$

$$B = M_1\Phi_1 + M_2\Phi_2 + M_3\Phi_3 + M_4\Phi_4 = \sum_{i=1}^{4} M_i\Phi_i$$

$$C = N_1\Phi_1 + N_2\Phi_2 + N_3\Phi_3 + N_4\Phi_4 = \sum_{i=1}^{4} N_i\Phi_i$$

$$D = O_1\Phi_1 + O_2\Phi_2 + O_3\Phi_3 + O_4\Phi_4 = \sum_{i=1}^{4} O_i\Phi_i \tag{A.2}$$

where,

$$
\begin{aligned}
\triangle =&(Z_3 - Z_4)(\xi_1 Y_2 - \xi_2 Y_1) + (Z_4 - Z_2)(Z_2 - Z_3)(\xi_1 Y_4 - \xi_4 Y_1)\\
&+ \xi_2[Y_3(Z_1 - Z_4) - Y_4(Z_1 - Z_3)]\\
&+ \xi_3[Y_4(Z_1 - Z_2) - Y_2(Z_1 - Z_4)]\\
&+ \xi_4[Y_2(Z_1 - Z_3) - Y_2(Z_1 - Z_2)]
\end{aligned}
$$

$$
\begin{aligned}
L_1 =&\frac{Y_2(Z_3 - Z_4) + Y_3(Z_4 - Z_2) + Y_4(Z_2 - Z_3)}{\triangle}\\
L_2 =&-\frac{Y_1(Z_3 - Z_4) + Y_3(Z_4 - Z_1) + Y_4(Z_1 - Z_3)}{\triangle}\\
L_3 =&\frac{Y_1(Z_2 - Z_4) + Y_2(Z_4 - Z_1) + Y_4(Z_1 - Z_2)}{\triangle}\\
L_4 =&-\frac{Y_1(Z_2 - Z_3) + Y_2(Z_3 - Z_1) + Y_3(Z_1 - Z_2)}{\triangle}
\end{aligned}
$$

$$
\begin{aligned}
M_1 =&-\frac{\xi_2(Z_3 - Z_4) + \xi_3(Z_4 - Z_2) + \xi_4(Z_2 - Z_3)}{\triangle}\\
M_2 =&\frac{\xi_1(Z_3 - Z_4) + \xi_3(Z_4 - Z_1) + \xi_4(Z_1 - Z_3)}{\triangle}\\
M_3 =&-\frac{\xi_1(Z_2 - Z_4) + \xi_2(Z_4 - Z_1) + \xi_4(Z_1 - Z_2)}{\triangle}\\
M_4 =&\frac{\xi_1(Z_2 - Z_3) + \xi_2(Z_3 - Z_1) + \xi_3(Z_1 - Z_2)}{\triangle}
\end{aligned}
$$

$$
\begin{aligned}
N_1 =&\frac{\xi_2(Y_3 - Y_4) + \xi_3(Y_4 - Y_2) + \xi_4(Y_2 - Y_3)}{\triangle}\\
N_2 =&-\frac{\xi_1(Y_3 - Y_4) + \xi_3(Y_4 - Y_1) + \xi_4(Y_1 - Y_3)}{\triangle}\\
N_3 =&\frac{\xi_1(Y_2 - Y_4) + \xi_2(Y_4 - Y_1) + \xi_4(Y_1 - Y_2)}{\triangle}\\
N_4 =&-\frac{\xi_1(Y_2 - Y_3) + \xi_2(Y_3 - Y_1) + \xi_3(Y_1 - Y_2)}{\triangle}
\end{aligned}
$$

$$
\begin{aligned}
O_1 =&-\frac{\xi_2(Y_3 Z_4 - Y_4 Z_3) + \xi_3(Z_2 Y_4 - Z_4 Y_2) + \xi_4(Y_2 Z_3 - Z_2 Y_3)}{\triangle}\\
O_2 =&\frac{\xi_1(Y_3 Z_4 - Y_4 Z_3) + \xi_3(Z_1 Y_4 - Z_4 Y_1) + \xi_4(Y_1 Z_3 - Z_1 Y_3)}{\triangle}\\
O_3 =&-\frac{\xi_1(Y_2 Z_4 - Y_4 Z_2) + \xi_2(Z_1 Y_4 - Z_4 Y_1) + \xi_4(Y_1 Z_2 - Z_1 Y_2)}{\triangle}\\
O_4 =&\frac{\xi_1(Y_2 Z_3 - Y_3 Z_2) + \xi_2(Z_1 Y_3 - Z_3 Y_1) + \xi_3(Y_1 Z_2 - Z_1 Y_2)}{\triangle}
\end{aligned}
$$

# APPENDIX B. Interpolation Function for Pressure

The pressure interpolation is given by $p = -(\alpha x + \beta y + \gamma z + \eta)$. The coefficients are found by satisfying this equation for the four node points of a tetrahedron. The formulation is carried out in the global coordinate system $(x, y, z)$. The system of equations is given below:

$$\alpha x_1 + \beta y_1 + \gamma z_1 + \eta = -p_1$$

$$\alpha x_2 + \beta y_2 + \gamma z_2 + \eta = -p_2$$

$$\alpha x_3 + \beta y_3 + \gamma z_3 + \eta = -p_3$$

$$\alpha x_4 + \beta y_4 + \gamma z_4 + \eta = -p_4 \tag{B.1}$$

Using Cramer's rule, the above equations are solved to yield the coefficients $\alpha, \beta, \gamma, \eta$.

$$-\frac{\partial p}{\partial x} = \alpha = \sum_{i=1}^{4} \bar{L}_i p_i$$

$$-\frac{\partial p}{\partial y} = \beta = \sum_{i=1}^{4} \bar{M}_i p_i$$

$$-\frac{\partial p}{\partial z} = \gamma = \sum_{i=1}^{4} \bar{N}_i p_i \tag{B.2}$$

where, $\bar{L}_i$ etc. are given as follows:

$$\begin{aligned}
\triangle = & x_1[y_2(z_3 - z_4) + z_2(y_4 - y_3) + (y_3 z_4 - y_4 z_3)] \\
& - y_1[x_2(z_3 - z_4) + z_2(x_4 - x_3) + (x_3 z_4 - x_4 z_3)] \\
& + z_1[x_2(y_3 - y_4) + y_2(x_4 - x_3) + (x_3 y_4 - x_4 y_3)] \\
& - [x_2(y_3 z_4 - y_4 z_3) + y_2(x_4 z_3 - x_3 z_4) + z_2(x_3 y_4 - x_4 z_3)]
\end{aligned}$$

$$\bar{L}_1 = -\frac{y_2(z_3 - z_4) + y_3(z_4 - z_2) + y_4(z_2 - z_3)}{\triangle}$$
$$\bar{L}_2 = \frac{y_1(z_3 - z_4) + y_3(z_4 - z_1) + y_4(z_1 - z_3)}{\triangle}$$
$$\bar{L}_3 = -\frac{y_1(z_2 - z_4) + y_2(z_4 - z_1) + y_4(z_1 - z_2)}{\triangle}$$
$$\bar{L}_4 = \frac{y_1(z_2 - z_3) + y_2(z_3 - z_1) + y_3(z_1 - z_2)}{\triangle}$$

$$\bar{M}_1 = \frac{x_2(z_3 - z_4) + x_3(z_4 - z_2) + x_4(z_2 - z_3)}{\triangle}$$
$$\bar{M}_2 = -\frac{x_1(z_3 - z_4) + x_3(z_4 - z_1) + x_4(z_1 - z_3)}{\triangle}$$
$$\bar{M}_3 = \frac{x_1(z_2 - z_4) + x_2(z_4 - z_1) + x_4(z_1 - z_2)}{\triangle}$$
$$\bar{M}_4 = -\frac{x_1(z_2 - z_3) + x_2(z_3 - z_1) + x_3(z_1 - z_2)}{\triangle}$$

$$\bar{N}_1 = -\frac{x_2(y_3 - y_4) + x_3(y_4 - y_2) + x_4(y_2 - y_3)}{\triangle}$$
$$\bar{N}_2 = \frac{x_1(y_3 - y_4) + x_3(y_4 - y_1) + x_4(y_1 - y_3)}{\triangle}$$
$$\bar{N}_3 = -\frac{x_1(y_2 - y_4) + x_2(y_4 - y_1) + x_4(y_1 - y_2)}{\triangle}$$
$$\bar{N}_4 = \frac{x_1(y_2 - y_3) + x_2(y_3 - y_1) + x_3(y_1 - y_2)}{\triangle}$$

$$\bar{O}_1 = \frac{x_2(y_3z_4 - y_4z_3) + x_3(z_2y_4 - y_2z_4) + x_4(y_2z_3 - z_2y_3)}{\triangle} \tag{B.3}$$
$$\bar{O}_2 = -\frac{x_1(y_3z_4 - y_4z_3) + x_3(z_1y_4 - y_1z_4) + x_4(y_1z_3 - z_1y_3)}{\triangle} \tag{B.4}$$
$$\bar{O}_3 = \frac{x_1(y_2z_4 - y_4z_2) + x_2(z_1y_4 - y_1z_4) + x_4(y_1z_2 - z_1y_2)}{\triangle} \tag{B.5}$$
$$\bar{O}_4 = -\frac{x_1(y_2z_3 - y_3z_2) + x_2(z_1y_3 - y_1z_3) + x_3(y_1z_2 - z_1y_2)}{\triangle} \tag{B.6}$$

# APPENDIX C. Derivation of the Pressure Equation

Taking the continuity equation written in terms of the artifical velocity field as the starting point, we substitute the expressions for the artificial velocities and expand to obtain the coefficients for the pressure equation.

$$
\begin{aligned}
&\rho\Bigg[\frac{\hat{u}_r+\hat{u}_s+\hat{u}_t}{3}+\frac{d_r^u+d_s^u+d_t^u}{3}\big(S^u+\bar{L}_1p_1+\bar{L}_2p_2+\bar{L}_3p_3+\bar{L}_4p_4\big)n_x\\
&+\frac{\hat{v}_r+\hat{v}_s+\hat{v}_t}{3}+\frac{d_r^v+d_s^v+d_t^v}{3}\big(S^v+\bar{M}_1p_1+\bar{M}_2p_2+\bar{M}_3p_3+\bar{M}_4p_4\big)n_y\\
&+\frac{\hat{w}_r+\hat{w}_s+\hat{w}_t}{3}+\frac{d_r^w+d_s^w+d_t^w}{3}\big(S^w+\bar{N}_1p_1+\bar{N}_2p_2+\bar{N}_3p_3+\bar{N}_4p_4\big)n_z\Bigg]=0
\end{aligned}
\tag{C.1}
$$

For a given node point, say 1, we assemble the terms containing $p_1's$ , which make up the $a_p'$ for the pressure equation. The rest of the pressure terms contribute to the term $a_{nb}'$ of the pressure equation. The remaining terms contribute to the pressure source $b_p$.

# BIBLIOGRAPHY

[1] Weiss, J. M. and Smith, W. A., “Solution of Unsteady, Low Mach Number Flow using a Preconditioned Multi-Stage Scheme on an Unstructured Mesh”, *AIAA Computational Fluid Dynamics Conference, 11th, Orlando, FL*, July 6-9, 1993.

[2] Weiss, J. M. and Smith, W. A., “Preconditioning Applied to Variable and Density Time-Accurate Flows on Unstructured Meshes”, *AIAA Journal*, 33:2050-2057, 1995

[3] Weiss, J. M., Maruszewski, J. P. and Smith, W. A., “Implicit Solution of Preconditioned Navier-Stokes Equations using Algebraic Multigrid”, *AIAA Journal*, 37:29-36, 1999

[4] Chorin, A. J., “A Numerical Method for Solving Incompressible Viscous Flow Problems”, *Journal of Computational Physics*, 2:12-26, 967

[5] Kwak, D., Chang, J. L. C. and Chakravarthy, S. R., “A Three-Dimensional Incompressible Navier-Stokes Flow Solver using Primitive Variables”, *AIAA Journal*, 24:390-396, 1985

[6] Taylor, C. and Hood, P., “A Numerical Solution of the Navier-Stokes Equations using the Finite Element Technique”, *Computational Fluids*, 1:73-100, 1973

[7] Gartling, D. K., “Finite Element Analysis of Viscous, Incompressible Fluid Flow”, *PhD Thesis, University of Texas*, Austin, Texas, 1975

[8] Chung, T. J., “Finite Element Analysis in Fluid Dynamics”, *McGraw-Hill*, New York, 1978

[9] Braaten, M. E., “Development and Evaluation of Iterative and Direct Methods for the Solution of Equations Governing Recirculating Flows”, *PhD Thesis, University of Minnesota*, Minneapolis, MN, 1985

[10] Kim, J. and Moin, P. “Application of a Fractional-Step Method to Incompressible Navier-Stokes Equations”, *Journal of Computational Physics*, 59:308-323, 1985

[11] Hughes, T. J. R., Liu, W. K. and Brooks, A., “Finite Element Analysis of Incompressible Viscous Flows by the Penalty Function Formulation”, *Journal of Computational Physics*, 30:1-60, 1979

[12] Heinrich, J. C. and Marshall, R. S., “Viscous Incompressible Flow by a Penalty Function Finite Element Method”, *Computational Fluids*, 9:73-83, 1981

[13] Reddy, J. N., “Penalty Finite Elements Methods in Mechanics”, *AMD-vol. 51*, November 1982

[14] Braaten, M. E. and Shyy, W., “Comparison of Iterative and Direct Method for Viscous Flow Calculations in Body-Fitted Co-ordinates”, *International Journal for Numerical Methods in Fluids*, 6:325-349, 1986

[15] Lee, S. L. and Tzong, R. Y., “Artificial Pressure for Pressure-Linked Equation”, *International Journal for Heat Mass Transfer*, 35:2705-2716, 1992

[16] Sato, Y., Hino, T., and Hinatsu, M., “Unsteady Flow Simulation Around a Moving Body by an Unstructured Navier-Stokes Solver”, *Proceedings of the Sixth Numerical Towing Tank Simulation*, Rome, Italy, 2003

[17] Sheng, C. H., Whitfield, D. L. and Anderson, W. K., “A Multiblock Approach for Calculating Incompressible Fluid Flows on Unstructured Grids”, *AIAA Journal*, 37(2):169-176, 1999

[18] Harlow, F. H. and Welch, J. E., “Numerical Calculation of Three-Dimensional Time Dependent Viscous Incompressible Flow of Fluid with Free Surfaces”, *Physics of Fluids*, 1:2182, 1965

[19] Patankar, S. V., “Numerical Heat Transfer and Fluid Flow”, *Hemisphere Publishing Corp.*, New York, 1980

[20] Moukalled, F. and Darwish, M., “A Unified Formulation of the Segregated Class of Algorithm for Fluid Flow at all Speeds”, *Numerical Heat Transfer, Part B*, 37:103-139, 2000

[21] Miller, T. F. and Schmidt, F. W., “Use of Pressure Weighted Interpolation Method for Solution of Incompressible Navier-Stokes Equations on Non-staggered Grids”, *Numerical Heat Transfer*, 14:213-233, 1988

[22] Majumdar,S., “Role of Under-relaxation in Momentum Interpolation for Calculation of Flow on Non-staggered Grids”, *Numerical Heat Transfer*, 13:125-132, 1988

[23] Hall, C., Cavendish, J. and Frey, W., “The Dual-Variable Method for Solving Fluid Flow Difference Equations on Delaunay Triangulations”, *Computational Fluids*, 20:145-164, 1991

[24] Hall, C., Porsching, T. and Hu, P., “Covolume-dual Variable Method for Thermally Expandable Flow on Unstructured Triangular Grids”, *Journal of Computational Fluid Dynamics*, 2:111-139, 1994

[25] Nicolaides, R., Porsching, T. and Hall, C., “Covolume Methods in Computational Fluid Dynamics”, *In M. Hafez, K. Oshima (Eds.), Computational Fluid Dynamics Review*, pages 279-299, Wiley, Chichester, UK, 1995

[26] Nicolaides, R., “The Covolume Approach on Computing Incompressible Flows”, *In M. Gunzburger, R. Nicolaides (Eds.), Incompressible Computational Fluid Dynamics*, pages 295-333, Cambridge University Press, Cambridge, UK, 1993

[27] Perot, B., “Conservation Properties of Unstructured Staggered Mesh Schemes”, *Journal of Computational Physics*, 159:58-89, 2000

[28] Rida, S., McKenty, F. Meng and Reggio, M., “A Staggered Control Volume Scheme for Unstructured Triangular Grids”, *International Journal for Numerical Methods in Fluids*, 25:697-717, 1997

[28] Wenneker, I., Segal, A. and Wesseling, P., “A Mach-Uniform Unstructured Staggered Grid Method”, *International Journal for Numerical Methods in Fluids*, 40:1209-1235, 2002

[29] Wenneker, I., Segal, A. and Wesseling, P., “Conservation Properties for a New Unstructured Staggered Scheme”, *Computational Fluids*, 32:139-147, 2003

[30] Vidovic, D., Segal, A. and Wesseling, P., “A Superlinearly Convergent Finite Volume Method for the Incompressible Navier-Stokes Equations on Staggered Unstructured Grids”, *Journal of Computational Physics*, 198:159-177, 2004

[31] Baliga, B. R. and Patankar, S. V., “A Control Volume Finite-Element Method for Two Dimensional Fluid Flow and Heat Transfer”, *Numerical Heat Transfer*, 6:245-261, 1983

[32] Prakash, C. and Patankar, S. V., “A Control Volume Based Finite Element Method for Solving the Navier-Stokes Equations using Equal-Order Velocity-Pressure Formulation”, *Numerical Heat Transfer*, 8:259-280, 1985

[33] Prakash, C., “An Improved Control Volume Finite-Element Method for Heat and Mass Transfer, and for Fluid Flow using Equal-Order Velocity-Pressure Interpolation”, *Numerical Heat Transfer*, 9:253-276, 1986

[33] Prakash, C., “A Finite Element Method for Predicting Flow through Ducts with Arbitrary Cross Sections”, *PhD thesis*, University of Minnesota, Minneapolis, MN, 1981

[34] Muir, B. L. and Baliga, B. R., “Solution of Three-Dimensional Convection-Diffusion Problems using Tetrahedral Elements and Flow-Oriented Upwind Interpolation Functions”, *Numerical Heat Transfer*, 9:143-162, 1986

[35] Lestari, A., “Development of Unsteady Algorithms for Pressure-based Unstructured Solver for Two-Dimensional Incompressible Flows”, *MS Thesis, Iowa State University,*, Ames, IA, 2009

[36] Rajagopalan, R. G. and Fanucci, J. B., “Finite-Difference Model for Vertical Axis Wind Rotors”, *Journal of Propulsion and Power*, Vol. 1, No. 6, November-December, 1985

[37] Paraschivoiu, I., Mason, C., and Rajagopalan, R. G., "Predictions and Experiments of the VAWT Viscous Flow Field", *AIAA 87-1429, Presented at AIAA 19th Fluid Dynamics, Plasma Dynamics and Lasers Conference*, Honolulu, Hawaii, June 8-10, 1987

[38] Rajagopalan, R. G., and Zhang Zhaoxing, "Performance and Flow Field of a Ducted Propeller", *AIAA/ASME/SAE/ASEE 25th Joint Propulsion Conference*, Monterey, CA., July 10-12, 1989

[39] Rajagopalan, R. G., and Lim, C. K., "Laminar Flow Analysis of a Rotor in Hover", *Journal of the American Helicopter Society*, 36:12-23, 1991

[40] Rajagopalan, R. G., and Mathur, S. R., "Three Dimensional Analysis of a Rotor in Forward Flight", *Journal of the American Helicopter Society*, Vol. 38, No. 3, pp. 14-25, 1993

[41] Zori, L., and Rajagopalan, R. G., "Navier-Stokes Calculations of Rotor-Airframe Interaction in Forward Flight", *Journal of the American Helicopter Society*, Vol. 40, No. 2, pp. 56-67, 1995

[42] Rajagopalan, R. G., Berg, D. E., and Klimas, P. C., "Development of a Three-Dimensional Model for the Darrieus Rotor and Its Wake", *Journal of Propulsion and Power*, Vol. 11, No. 2, pp. 185-195, March-April 1995

[43] Rajagopalan, R. G., and Keys, C., "Detailed Aerodynamic Design of the RAH-66 Fantail Using CFD", *Journal of the American Helicopter Society*, Vol. 42, No. 4, October 1997

[44] Poling, D. R., Rosenstein, H., and Rajagopalan, R. G., "Use of a Navier-Stokes Code in Understanding Tiltrotor Flowfields in Hover", *Journal of the American Helicopter Society*, Vol. 42, No. 2, pp. 103-109, April 1998

[45] Tadghighi, H., Rajagopalan, R. G., and Burley, Casey L., "Simulation of Tiltrotor Fountain Flow Field Effects Using a Finite Volume Technique - An Aero-Acoustic Study", *Journal of the American Helicopter Society*, Vol. 43, No. 2, pp. 150-153, April 1999

[46] Kim, Y. H., and Park, S. O., “Navier-Stokes Simulation of Unsteady Rotor-Airframe Interaction with Momentum Source Method”, *International Journal of Aeronautical and Space Sciences*, Vol. 10, No. 2, November 2009

[47] Yang, J. Y., Yang, S. C., Chen, Y. N. and Hsu, C. A., “Implicit Weighted ENO Schemes for the Three-Dimensional Incompressible Navier-Stokes Equations”, *Journal of Computational Physics*, Vol. 146, pp. 464-487, 1998

[48] Iwatsu, R., Hyun, J. M. and Kuwahara, K., “Numerical Simulations of Three-Dimensional Flow in a Cubic Cavity with an Oscillating Lid”, *International Journal of Fluids Engineering, ASME*, Vol. 115, December 1993

[49] Wirogo, S., “Unsteady Simulations of Two- and Three-Dimensional Flows”, *M.S. Thesis, Iowa State University*, April 1994

[50] Caradonna, F. X., and Tung, C., “Experimental and Analytical Studies of a Model Helicopter in Hover”, *NASA Technical Memorandum 81232*, September 1981

[51] Rabbot Jr, J. P., “Static-Thrust Measurements of the Aerodynamic Loading on a Helicopter Rotor Blade”, *Langley Aeronautical Laboratory*, Langley Field, VA., Technical Note 3688, July 1956

[52] Light, J. S., “Tip Vortex Geometry of a Hovering Helicopter Rotor in Ground Effect”, *45th Annual Forum of the American Helicopter Society*, Boston, Massachusetts, May 22-24, 1989

[53] Maresca, M. J., “A Pressure based Incompressible Unstructured Solver for General Two-Dimensional Flows”, *Master’s Thesis, Iowa State University*, Ames, 1995

[54] Guntupalli, K. and Rajagopalan, R. G.,“Momentum Source Model for Discrete Blades”, *International Powered Lift Conference, American Helicopter Society*, October 5-7, 2010, Philadelphia, PA

[55] “Virtual Blade Model”, Developed by Fluent Inc., 2004

[56] Pavanakumar, M., "Acoustic Prediction of Heavy Lift Rotor Configurations using Momentum Source Method", *Master's Thesis, Department of Aerospace Engineering, Pennsylvania State University*, May 2010